Lawrence Berkeley Laboratory
UNIVERSITY OF CALIFORNIA

Physics, Computer Science & Mathematics Division

DECAYS OF J/ψ (3100) TO BARYON FINAL STATES

Mark William Eaton
(Ph.D. thesis)

May 1982

Prepared for the U.S. Department of Energy under Contract DE-AC03-76SF00098

DISCLAIMER

LBL-14581

DECAYS OF J/ψ (3100) TO BARYON FINAL STATES

Mark William Eaton

Ph.D. Thesis

May 1982

Physics, Computer Science & Mathematics Division
Lawrence Berkeley Laboratory
University of California
Berkeley, CA 94720

This work was supported by the Office of Energy Research, Division of High Energy and Nuclear Physics of the U.S. Department of Energy under Contract No. DE-AC03-76SF00098.

Mark William Eaton

Decays of J/ψ (3100) to Baryon Final States

ABSTRACT

We present results for the decays of ψ(3100) into baryon and hyperon final states. The sample studied here consists of 1.3 million produced ψ decays. The decays into nonstrange baryons agree well with currently established results, but with better statistics. In addition, significant resonance formation in multibody final states is observed. The decay $\psi \to \bar{p}p\gamma$, the first direct photon decay of the ψ involving baryons in the final state, is presented and the theoretical implications of the decays are briefly explored.

Several new decays of the ψ involving strange baryons are explored, including the first observations of three body final states involving hyperons. The I-spin symmetry of the strong decay ψ → baryons has clearly been observed. The reduced matrix elements for $\psi \to B\bar{B}$ are presented for final states of different SU(3) content. The $B_8\bar{B}_8$ results are in excellent agreement with the ψ being an SU(3) singlet as are the results for $\psi \to B_{10}\bar{B}_{10}$. We present the first evidence for the SU(3) violating decays of the type $\psi \to B_8\bar{B}_{10}$ + c.c.. Angular distributions for $\psi \to B_8\bar{B}_8$ are presented and compared with theoretical predictions. Statistics are limited, but the data tends to prefer other than a $1 + \cos^2\theta$ distribution.

ACKNOWLEDGEMENTS

Suffice it to say that this thesis would not be possible except for the incalculable efforts of the many MKII physicists, technicians and staff, without whose help this data would not have existed. Special thanks must go to my advisor Gerson Goldhaber, whose overriding joy of physics never let me lose track of the goals of such an endeavor; my fellow graduate student John Dillon, without whose substantial software contributions much of the new results in this thesis would not be possible; Marty Breidenbach, whose dedication to the physical entity of the MKII detector instilled in me the respect for how important an understanding of the hardware is to doing high energy physics; and Debi Lamm, for keeping me sane during the trying times of composing this thesis.

DEDICATION

I dedicate this thesis to my father, for the degree he never finished, and to my mother, for putting up with me all these years.

CONTENTS

LIST OF TABLES

LIST OF FIGURES

Chapter I

THEORETICAL CONSIDERATIONS

1.1 AN OVERVIEW OF CHARM

1.1.1 History

With the simultaneous discovery[1,2] of the J/ψ(3100) (hereafter called ψ), the high energy physics community was never again to languish smugly in its established beliefs. For these pioneers of the new physics would in just eight years completely revolutionize high energy physics so that the flavor SU(3) theory so dearly held in the 60's is now regarded as a low energy artifact of the "true" theory of strong interactions, color SU(3). Color SU(3) has achieved such a status that it has been dubbed QCD (Quantum Chromo-Dynamics), in direct analogy with the extremely well verified theory of electromagnetic interactions, QED.

If the ψ is actually a charmonium state (i.e. a bound state of a charmed quark and antiquark), then it should be produced in e^+e^- annihilations via an intermediate virtual photon. This need not be the case, for example, if the ψ couples directly to leptons. By carefully measuring[3] the cross section for leptons at center of mass energies in the vicinity of the ψ, one clearly sees the interference between the timelike diagrams for direct production of leptons via an intermediate virtual photon and the ψ decay into lepton

pairs. This is sufficient to not only establish that the ψ does not couple directly to leptons, but establishes the quantum numbers of the ψ as those of the photon, $J^{PC} = 1^{--}$.

The interpretation of the ψ as the lowest radial excitation 1^3S_1 bound state of a charmed quark and antiquark was left to little serious question with the discovery[4] of the D^0 and its isodoublet partner[5] the D^+. Two main points support[6] the interpretation of these states as charmed mesons:

1. Both the D^0 and the D^+ are produced in final states containing both a D meson and an anti-D meson, as one would expect for particles with a quantum number conserved by the electromagnetic interaction.
2. The weak decays of these particles are observed as they must be if they carry a quantum number conserved by the strong or electromagnetic interaction.

Charm was firmly established, opening the door for new spectroscopy of charmed states which abounds in journals today.

1.1.2 The charmonium system

The discovery of the ψ created a flurry of activity, both theoretical and experimental. Theoreticians began with the simplest model one can think of for the charmonium system, the nonrelativistic quark model. The nonrelativistic quark model is certainly nothing new; it is simply the bound state of two heavy fermions by an instantaneous smooth central potential.[7] Examples are common in

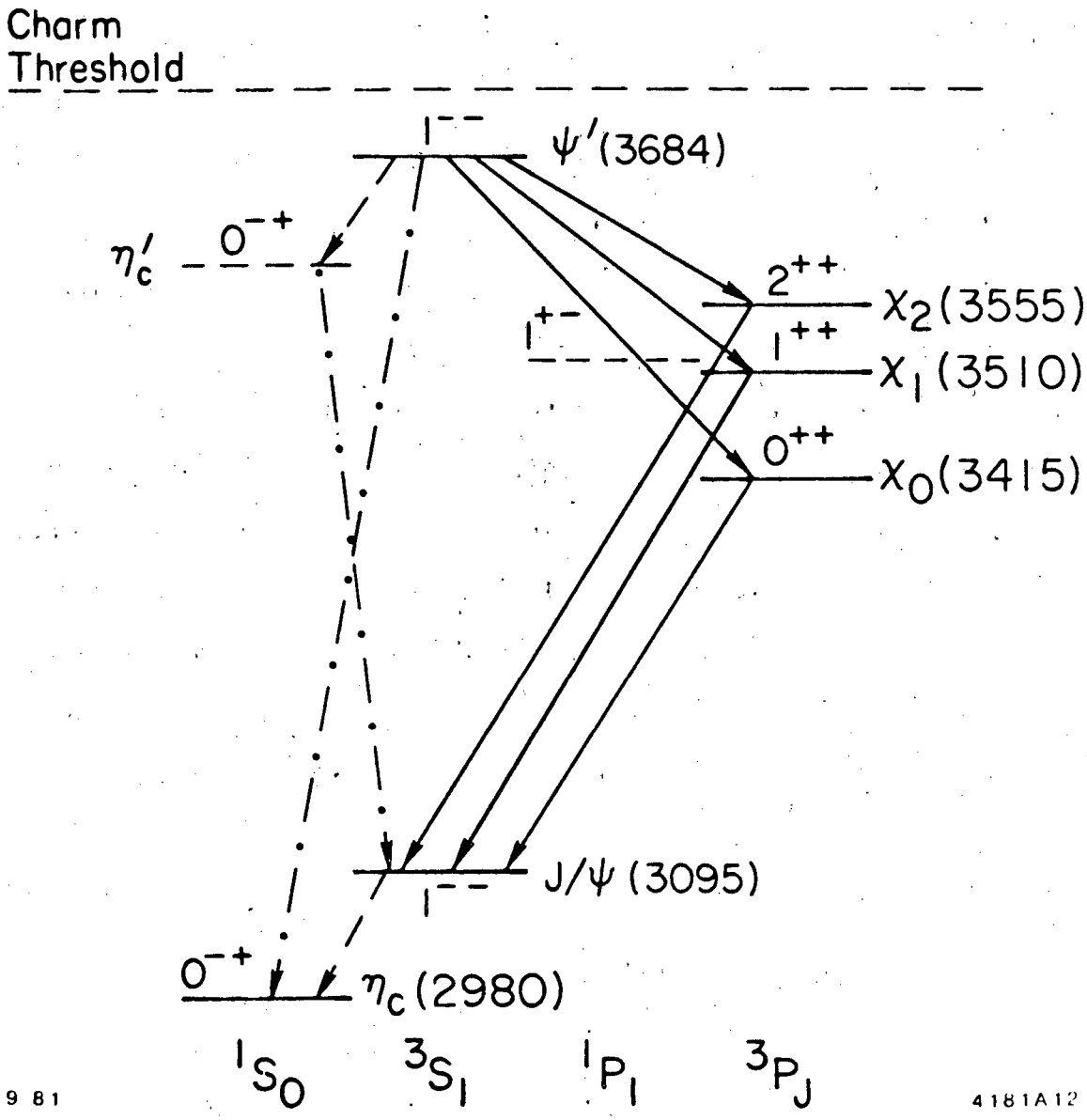

Figure 1: Charmonium level diagram. Established levels are solid lines, predicted are dashed. Solid arrows indicate E1 transitions, dashed arrows indicate allowed M1 transitions, and dot-dashed arrows indicate hindered M1 transitions.

physics; the positronium system being a well known one. The literature abounds[8-14] with models for the QCD potential; the amazing

feature is that they all fit gross features of the charmonium (and for that matter, bottomonium) spectroscopy fairly well.

Once we are convinced a simple potential model recreates the gross features of the charmonium model, the most general analysis includes spin interactions of the charmed constituents of the ψ. This problem is well known[15] and has four terms in the potential corresponding to Thomas, spin-orbit, tensor, and spin-spin forces. Hard predictions aside, the nonrelativistic quark model then immediately predicts the level structure for the charmonium system, shown in figure 1. It is a tribute to the experimentalists hard work that there exists a viable candidate for every charmonium state in figure 1 except the 1^1P_1 state,[16] while it is remarkable how well the simple potential model agrees with the observed spectra, even up to the splitting of the χ states.

1.1.3 Hadronic decays

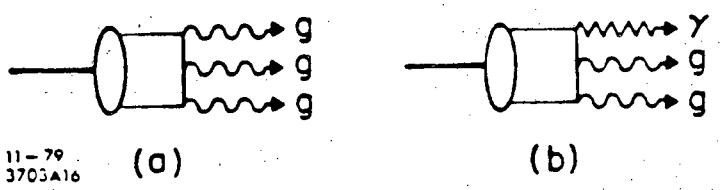

Figure 2: Lowest order diagrams for $\psi \to ggg$ and $\psi \to \gamma gg$.

Whereas the level structure of the charmonium system is aptly described by the simple nonrelativistic quark model, the dynamical

behavior of the ψ is a substantially more difficult problem. One can imagine that the charmonium level structure has probed only a small range of the strong interaction potential corresponding to the Bohr radius of the quarks in the charmonium states, while the hadronic decays pose a more formidable problem due to the inherently nonperturbative hadronization process of the gluons from the ψ decay.

The decay ψ → hadrons must be a strong decay as it conserves the quantum numbers strangeness and I-spin. It is an OZI-violating[17-21] decay, however, since the charm content of the ψ does not show up in the hadronic final state, as the lightest charmed meson has a mass more than half the ψ mass. Presumably, then, the ψ must decay into gluons, the mediators of the strong interaction. This accounts for the narrow (63 KeV) width of the ψ. The decay into one gluon is forbidden[22] by color conservation, while the decay to two gluons is forbidden by angular momentum conservation. It follows immediately that the minimum number of gluons allowed in the decay of a heavy quarkonia state is three.

Figure 2a) shows the lowest order allowed Feynman diagram for the decay ψ → hadrons. One can calculate the hadronic width of the ψ, but it depends on the imperfectly known quark state wave function at the origin. However, the leptonic width of the ψ suffers from the same problem, so the ratio of the two is independent of the wave function. We quote[23] the ratio of the hadronic width to the leptonic width for the ψ.

$$\frac{\Gamma(\psi \to ggg)}{\Gamma(\psi \to \ell^+\ell^-)} = \frac{5(\pi^2-9)\alpha_s^3}{18\pi\alpha^2}, \qquad (1)$$

where α_s is the strong coupling constant evaluated at a Q^2 roughly corresponding to the ψ mass and α is the QED coupling constant ($= 1/137$).

Equation (1) is for <u>all</u> hadronic final states. The much harder dynamical question is the rate to any exclusive final hadronic final state. Unfortunately, figure 2 shows our ignorance about the hadronization process of gluons; perturbative QCD cannot be a good description of the creation of hadrons as the strong coupling constant is near unity for the momentum transfer which is characteristic of the hadronization process. Since the theoretical understanding of nonperturbative processes is poor, so is the understanding of the final state dynamics in this problem.

Ironically, the most informative content on exclusive final states may come from the flavor SU(3) content of the ψ. Very simply, if the ψ is a charmonium state, one would expect negligible mixing of the ψ with other ordinary mesons due to the large mass difference between them. Consequently, the ψ should be an almost pure flavor SU(3) singlet, and its decay rates into baryon-antibaryon final states of the same SU(3) structure should be the equal to each other, except for phase space considerations, regardless of the quark content of the final state. This result is very nontrivial in that it says that the ψ decay matrix element is "blind" to the flavor content of the final state, unlike many perturbative QCD situations.

1.1.4 Direct photon decays

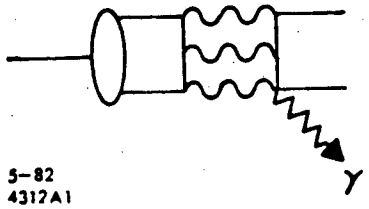

Figure 3: Radiative three gluon decay.

An interesting wrinkle in the hadronic decays of the ψ comes when one replaces one of the gluon lines in figure 2a) with a photon line, shown in figure 2b). This violates neither angular momentum conservation nor the color singlet nature of hadrons. Again, the rate for the ψ into a direct photon plus hadrons is not difficult to evaluate[24,25] but involves the quark state wave function. The ratio of the direct photon width to the hadronic width obviates this problem

$$\frac{\Gamma(\psi \to \gamma gg)}{\Gamma(\psi \to ggg)} = \frac{16\alpha}{5\alpha_s}. \qquad (2)$$

The surprising feature is that for a reasonable value of α_s, say .2, the rate is suppressed by only about an order of magnitude relative to the hadronic width. Direct photon events should be visible as fully reconstructed hadronic events with a single real photon.

The astute reader will have recognized that there is another way to get direct photons opposite a hadronic final state; this is sim-

ply the case where the photon is a bremsstrahlung of a final state quark line and the hadronic final state is due to the three gluon decay of the ψ, shown in figure 3. There are two points which support the interpretation of these events as direct photon events.

The first point is that OZI suppression works at the ψ. In order to get a three gluon final state one pays the price of α_s for the additional gluon vertex over the decay into two gluons. One can get a feeling for what this suppression is relative to the photon plus two gluon decay by simply plugging in α_s evaluated at the ψ ($\simeq .2$), which would indicate that the suppression is about a factor of 25. This would be competitive with the two gluon plus photon decay mode. In fact, this is probably not a very good estimate in that it predicts very little OZI suppression at the $\phi(1.020)$, whereas in fact it is of order[26-28] 10^{-2}.

A better estimate of the suppression may be gotten by looking at the ratio of what the ψ width would be if it were an OZI-allowed decay; this ratio is roughly 10^{-4}. Attributing (very roughly!) equal suppression factors to each of the three gluon lines gives a suppression of roughly 300. This is to be compared with roughly a suppression of 10 from the two gluon plus photon decay. Thus, we have good <u>experimental</u> evidence that diagrams of the type in figure 3 should be negligible in direct photon production. Higher order QCD corrections[29] to the two gluon plus photon diagram, however, may not be.

The second point is that the x spectrum of photons from the bremsstrahlung of a final state quark line should be radically different than that predicted by the first order QCD prediction, i.e. the spectrum should decrease instead of increase with x. Furthermore, the bremsstrahlung spectrum should be much softer than that from direct photon production. A hard photon spectrum from these decays is another way to establish the two gluon plus photon decay over the radiative three gluon decay of the ψ.

Chapter II

HARDWARE

2.1 THE MKII DETECTOR AT SPEAR

2.1.1 Introduction

The MKII detector is shown schematically in figure 4 (looking along beam line), and in figure 5 (isometric view). The MKII is a multi-purpose magnetic detector, designed for good charged and neutral particle reconstruction over a large fraction of the solid angle. Figures 4 and 5 illustrate many features of the MKII which are relevant to event reconstruction. In the following sections, we will outline those features which are important to the measurements in this thesis.

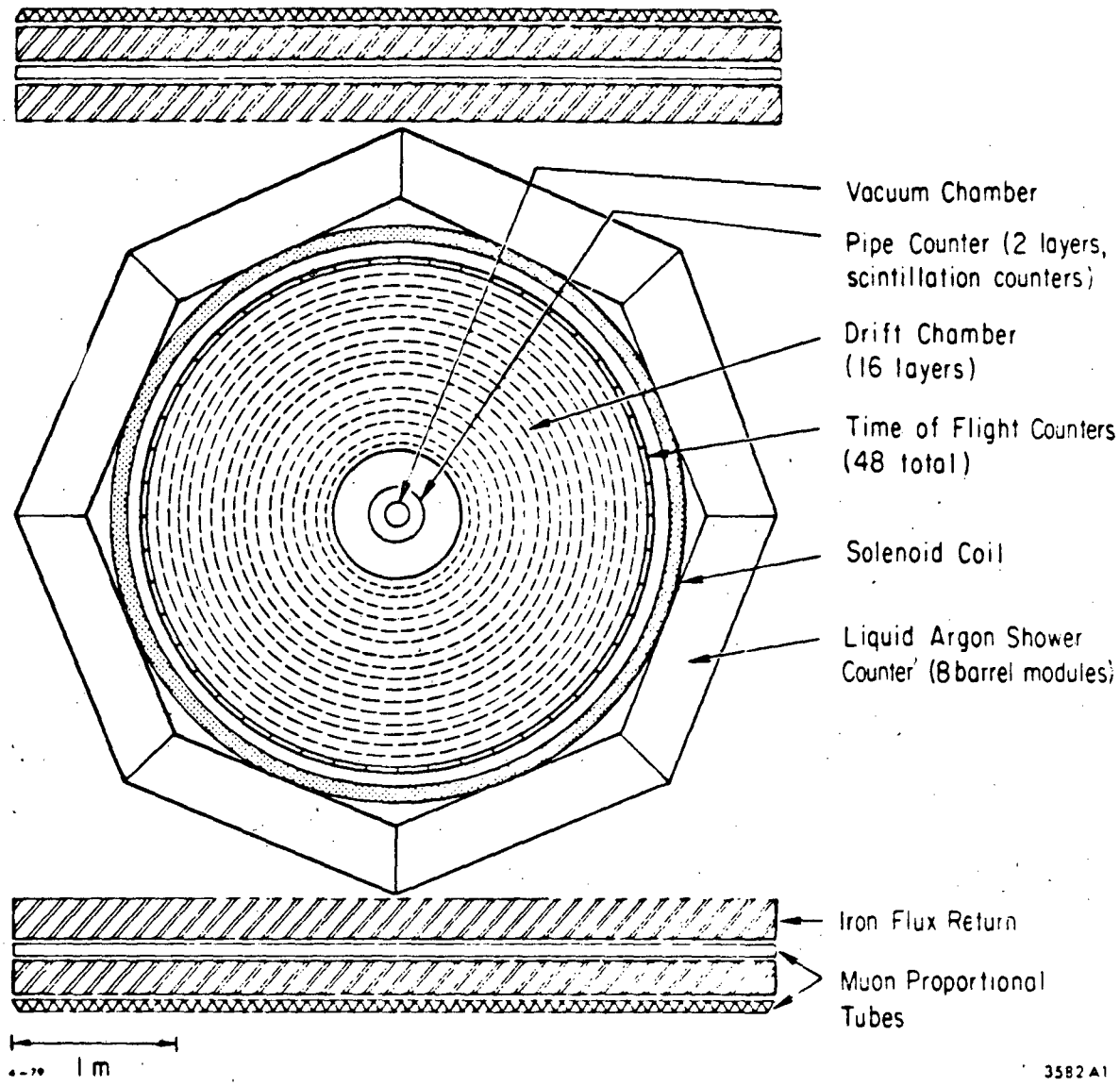

Figure 4: MKII detector (beamline view)
A) Beam pipe
B) Pipe counter
C) Drift chamber
D) Time of flight (TOF) counters
E) Magnet coil
F) Lead-liquid argon (LA) calorimeter modules
G) Bottom: Flux return; Side: Hadron absorber
H) Muon proportional tubes

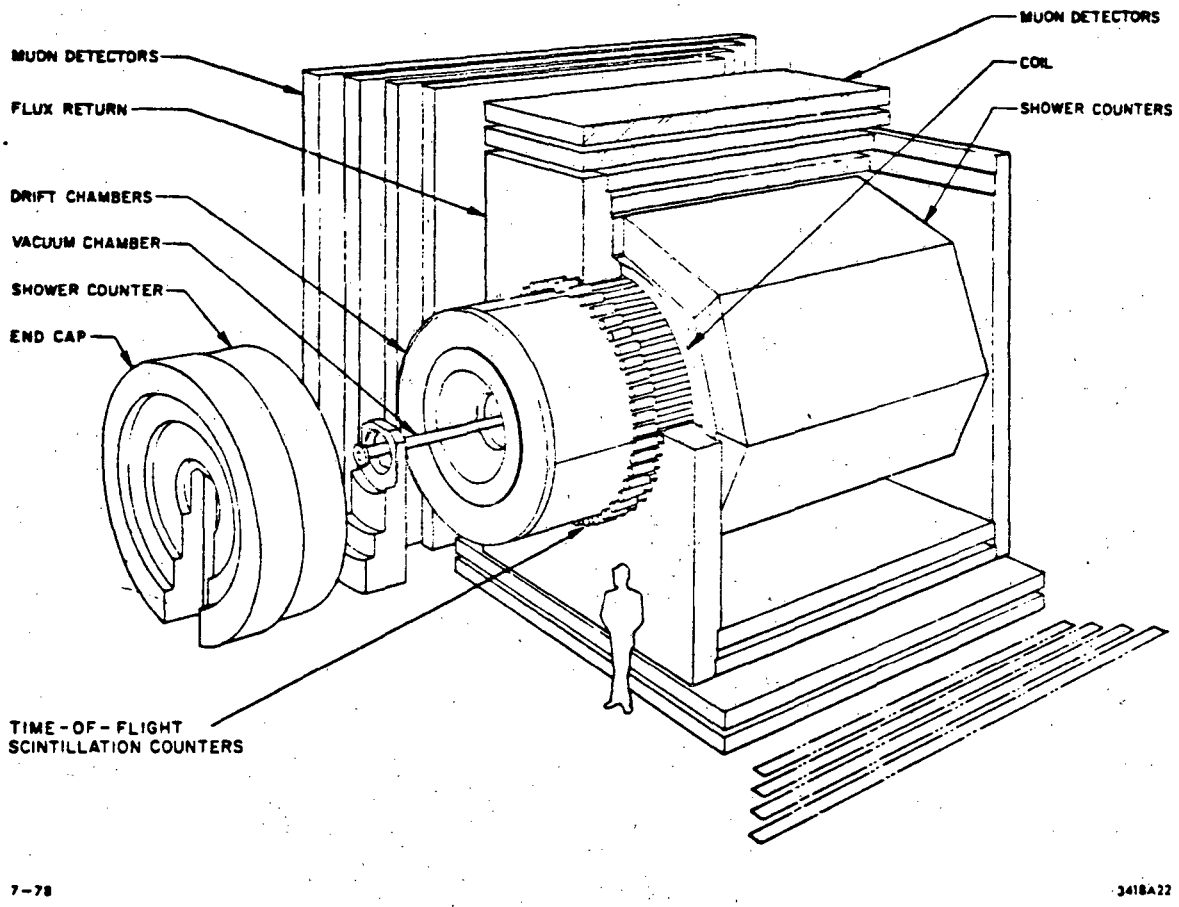

Figure 5: MKII detector (isometric view).

2.1.2 Pipe counter

Surrounding the beam pipe are two concentric cylinders of scintillator, each split into two hemicylinders. The light from each of the four hemicylinders is passed out along the beam pipe via a lucite light pipe until it is out of the magnet and viewed by a

photomultiplier. Each adjacent pair of hemicylinders is placed in coincidence for use in the primary trigger (see section 2.1.7).

2.1.3 Drift chamber

Radially outward from the pipe counter is a 15cm air gap followed by a lexan window. This window is the inner gas seal for the heart of the MKII, the drift chamber.

The drift chamber[30] is a large, single gas-volume cylinder, which provides a spatial resolution within the drift cells of $\simeq$ 220μm, and tracking over $\simeq$ 85% of 4πsr. The transverse momentum resolution of the drift chamber $\delta p/p$ is $\simeq$ 1% at 1 GeV/c at our operating magnetic field. Sense wires are strung in sixteen concentric cylindrical layers, six of which are axial (along the beam and magnetic field axis), and ten are "stereo" layers, oriented at $\pm 3^0$ relative to the beam axis. These stereo layers provide information regarding the dip of the track. Field wires are oriented to define the drift cell boundaries as well as the electric field gradient within the cell.

The sense wires are connected to 50Ω coaxial cable and sent to preamplifiers. The output from the preamplifier is then sent to a TAC[31] (Time to Amplitude Conversion) module, digitized, then read out. In addition, hit wires are provided via shift registers to the secondary trigger logic, and an OR of the shift register is used in the primary trigger logic (see section 2.1.7). The wire to wire alignment of each drift cell is done by simultaneously pulsing

the field wires through the high voltage network, which then couples capacitively to the sense wires, and the wires are read out. This isochronous start allows a system wide resolution of ≃ 1nsec (HWHM).

The advantage of a single gas volume for the drift chamber is that it provides less than .01 radiation length (X_0) for multiple scattering. The MKII drift chamber geometry allows reconstruction of a vertex to ≃ .5mm in the radial direction and ≃ 5mm in the axial direction. Knowledge of the beam-beam interaction point (for example from Bhabha events) decreases $\delta p/p$ to ≃ .5% at 1 Gev/c.

2.1.4 Time of flight (TOF) system

Immediately outside the aluminum outer can of the drift chamber are mounted 48 scintillators composed of the compound PILOT F. Each scintillator is 343cm × 20.3cm × 2.5cm, viewed on each end by an Amperex XP2230 photomultiplier. The scintillator light is passed out to the photomultipliers by lucite light rods.

The photomultiplier output is split 20% into an ADC (Amplitude to Digital Conversion) module, and 80% to a TDC (Time to Digital Conversion) module and latch. The latches are supplied at a fixed time relative to beam crossing, and are employed in the primary and secondary trigger (see section 2.1.7). The ADC is used to compensate for time slewing introduced by variations in the photomultiplier pulse height.

Calibration is done via a nitrogen (N_2) flash lamp which is pulsed to provide an isochronous signal to each scintillator via an optical fiber connected at the center of the each scintillator. This aligns each counter with respect to each other to ≃ 100psec. Further calibration is done offline by taking a sample of Bhabha and μ pair events and minimizing the variation of the predicted and reconstructed times. This results in a systemwide TOF resolution in this data sample of ≃ 300psec. For those occasions when more than one track hits a given counter, one time is usually recovered, with a degraded resolution of ≃ 480psec.

2.1.5 Magnet coil and flux return

Immediately outside of the TOF counters is the solenoidal magnet coil. It is $1.36X_0$ thick, which was operated at SPEAR to provide a 4.16kG uniform axial field. The magnetic flux is returned via the two upper and lower steel slabs shown in figure 4. These slabs were designed primarily for muon identification as opposed to their flux handling capabilities. The magnetic field is found to be constant to within ≃ 1.4% of its mean value. These small variations have been incorporated into the offline tracking programs via a polynomial fit to the actual field map, whose scale is monitored by an nuclear magnetic resonance (NMR) probe within the solenoid volume.

2.1.6 Lead-liquid argon (LA) shower counters

Just beyond the magnet coil are eight lead-liquid argon calorimeter modules. These "barrel" modules share a common vacuum jacket and cover 69% of 4πsr. The barrel modules are a $14X_0$ deep sandwich of 2mm thick lead and 3mm thick liquid argon gaps. The lead strips are 3.7cm wide for those in the θ direction, 5cm wide in the ϕ direction, and 7.4 cm wide in the "U" direction, where the U direction is 45^0 with respect to both the θ and the ϕ directions. The U direction is employed to resolve shower ambiguities.

In order to reduce the number of channels in the LA system to a tractable number ($\simeq$ 360 per module), the 18 layers are grouped internally in depth and width. The charge collected on the strips is then preamplified and integrated via a Sample and Hold Analog Module (SHAM). These analog signals are then digitized and read out. Strip by strip calibration is achieved by depositing a known amount of charge on the detector strips and then reading out the strips. The overall stack energy scale is set by using non-radiative Bhabha events and scaling the stack energy to be the drift chamber measured momentum, plus corrections for leakage out the back of the module , energy loss in the coil, and the entrance angle at the LA module.

2.1.7 Trigger logic

The MKII employs a two stage hardware trigger which offers good suppression of unwanted events while being highly efficient for beam-beam events. It has the disadvantage of having no z information available to it. The first stage, the primary trigger, is the coincidence between the pipe counter hemicylinders (PIPE), the beam crossing signal (BEAMX), and a drift chamber majority (DCM). The pipe counter was discussed in section 2.1.2. BEAMX is a signal from a pickup upstream of the interaction point on the e^- side. This signal is compensated for varying beam currents and is in coincidence with an RF signal in order to eliminate confusion from the e^+ bunch. DCM is an OR of selected drift chamber layers which have been hit. The entire decision making process takes $\simeq$ 600nsec., allowing $\simeq$ 200nsec. to clear the hardware before the next beam crossing.

If the primary trigger is satisfied, all resets and clears are aborted, and the secondary trigger logic begins. The secondary trigger logic then finds track candidates in the drift chamber. There are two major parts:

1. 24 "curvature" modules[32] which search in the xy plane for drift chamber hits within its "road" (mask of curvature).
2. A track counter module which collates the hardware tracks from the curvature modules into subgroups depending on the masks which have been satisfied.

Both the curvature modules and the track counter are programmable, enabling a wide variety of secondary trigger requirements. Typical definitions are an "A" track (four of six hits in a road), and a "B" track (three of five hits in a road, in the inner five layers). We use the mnemonic "$1\frac{1}{2}$ particle trigger" for the secondary trigger logic requirement of one A track and one B track. The trigger efficiency for the $1\frac{1}{2}$ particle trigger is found[33] to be $>$ 99.7%.

Chapter III

EVENT RECONSTRUCTION

3.1 INTRODUCTION

Reconstructing the physics quantities from the detector information is a long and very complex process. In this chapter, we will detail how the production analysis program, called PASS2, takes the detector information and uses this information to produce useful physics quantities. In addition, we will present other algorithms for data analysis which are pertinent to this thesis.

3.2 CHARGED TRACK RECONSTRUCTION

3.2.1 Filtering

Due to the large amount of raw information derived from the drift chamber, we use a two stage charged particle reconstruction algorithm. This has the advantage that the second stage of identification using the program TRAKR can use very sophisticated and time consuming analysis techniques as it is employed on less$^{3}/_{4}$ than 2/3 of the total input data sample. This filtering process removes essentially no useful beam-beam events.

3.2.2 TLTRKR

TLTRKR is the fast track association program. The information from the drift chamber arrives in TLTRKR as a list of hit wires and drift times, ordered by azimuth and layer. In the future we will refer to the drift times of these hit wires as drift chamber azimuths (DAZMs).

Before the input data is used, the DAZM list is searched for groups of > 11 adjacent cells in a given layer. These groups are flagged and eliminated from further analysis. These groups of "bad" DAZMs may arise from hardware problems, showers in the drift chamber, or grazing tracks. DAZMs with drift times outside expected limits are also removed. These techniques are invaluable in reducing the combinations TLTRKR must search for tracks.

TLTRKR first tries to reconstruct the hardware tracks by attaching hit wires in the six axial layers. The drift time is converted to a distance from the cell anode using the approximation of a constant drift velocity. The angle of incidence within the cell is estimated from the curvature and layer radius, hence the distance of closest approach to the sense wire (DCA) is determined. Note that there is a left-right ambiguity remaining in that we cannot measure on which side of the anode in the drift cell the track passed. Simple circle fits to these DCAs are usually sufficient to resolve these left-right ambiguities. The TLTRKR algorithm most notably has problems with closely spaced tracks, low momentum tracks, and steeply dipped tracks.

3.2.3 TRAKR

The program TRAKR is used to fully utilize the efficiency and precision of the drift chamber. TRAKR performs 3 functions:

1. It fits TLTRKR candidates, making a cut on the χ^2 of the fit.
2. From the pool of unused DAZMs, it associates tracks and attempts ambiguity resolution.
3. It fits collections of DAZMs where most of the ambiguities are resolved.

The fit procedure ARCS[35] does a three-dimensional linear least-squares fit to a helical orbit of the charged track parameters ϕ, k (= $1/p\cos\lambda$, λ the dip angle), s (= $\tan\lambda$), x, y, and z. Only the five of these six parameters α_μ are independent due to helical constraint. For each layer, the measured DCA d^m_i is calculated using the measured drift time and a sophisticated knowledge of the drift time-to-distance relationship.[30] ARCS then minimizes the function

$$\chi^2 = \sum_{i=1}^{N} \left\{ \frac{d^m_i - d_i(\alpha_\mu)}{\sigma^m_i} \right\}^2, \qquad (3)$$

with respect to the α_μ. The relationship between the d_i and the α_μ is described in detail in reference 35. On the last iteration, an error matrix Σ is calculated, given by

$$\Sigma^{-1}_{\mu\nu} = \frac{\partial^2 \chi^2}{2\partial\alpha_\mu \partial\alpha_\nu}. \qquad (4)$$

Contributions for multiple scattering are included, but other contributions are left out until the final vertexing is done. This

allows for tracks not originating from the primary vertex which are decay products of weakly decaying neutral particles (VEEs).

The final pass at track finding is also found in TRAKR. Adjacent stereo and axial layers are paired separately to look for peaks in curvature, which are then combined to form track candidates. These procedures tend to be slow because of the large number of combinations from a given pool of unused DAZMs. They can only be successful in the limit of high TLTRKR efficiency and a quiet data sample.

3.2.4 The TOF system

For the momentum range we are interested in, the TOF system will turn out to be an excellent method of particle identification for hadrons, namely π's, K's and p's. We have previously mentioned in section 3.2.3 how we reconstruct the helical path of the particle. If we can associate the track with a hit in the TOF counter, we can then determine the path length of the particle from the DCA to the TOF radius. The TOF counter gives us a measurement of the flight time of the particle for the reconstructed path length. From this we can calculate the m^2 (mass^2) of the particle from the path length, the reconstructed momentum, and the TOF.

Figure 6 shows the m^2 vs. momentum distribution for all particles in the data sample was used in this thesis. One clearly sees vertical bands centered on $m_\pi{}^2$, $m_K{}^2$, and $m_p{}^2$. These bands naturally widen with increasing momentum due to the ever-increasing

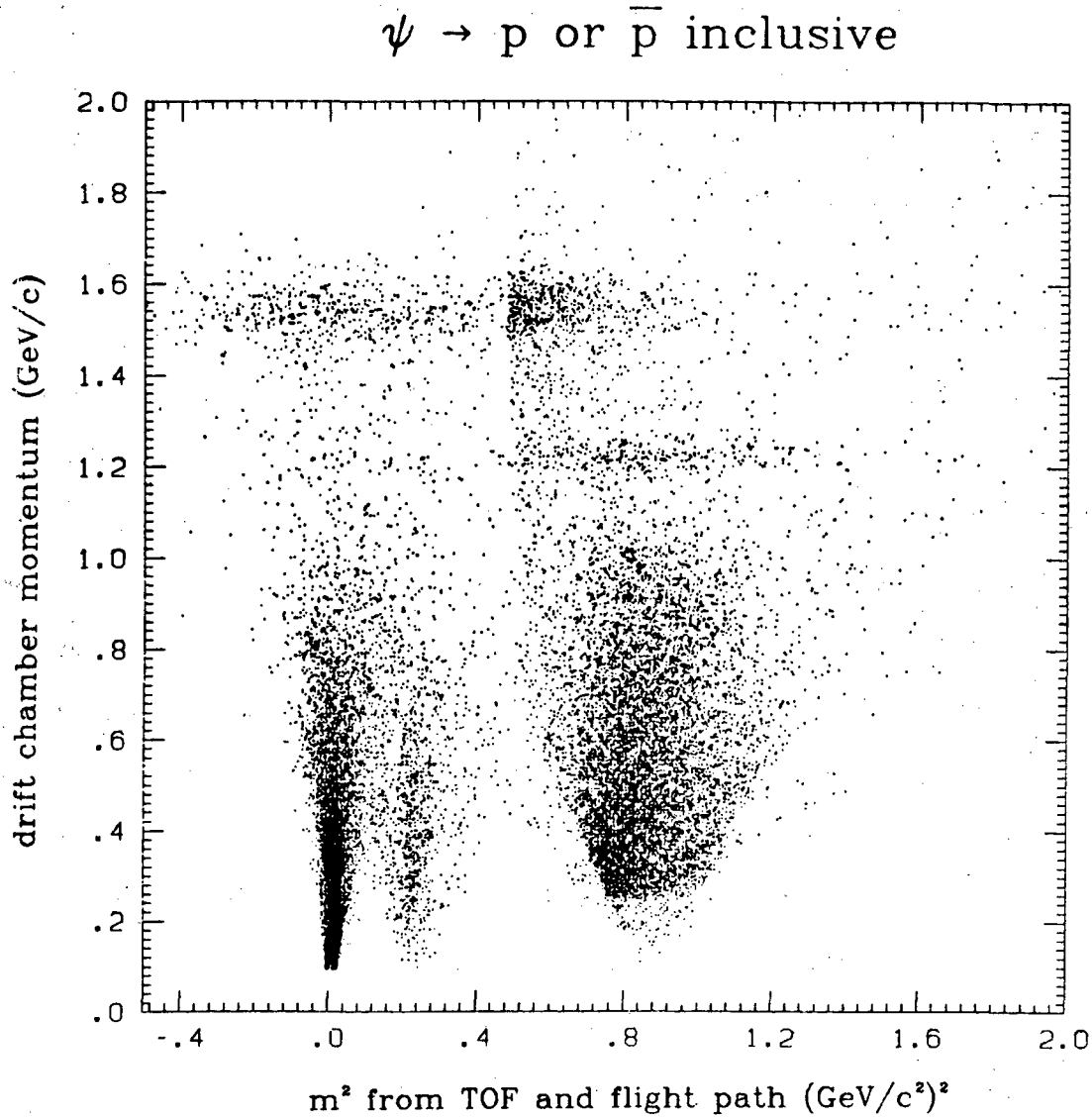

Figure 6: Scatterplot of m^2 vs. momentum. The cutoff near $m^2 = .5\ (GeV/c^2)^2$ is due to a loose proton weight cut on the data sample. This is looser than any other cut on the data samples used in this thesis. The horizontal band structure is discussed in the text.

velocity of the particle and the fixed time resolution of the TOF system. Nevertheless, good separation between protons and kaons is

obtained for momenta < 1.3 GeV/c. Note that all particles from baryon decays of the ψ have momentum in this range. The horizontal band at p = 1.2 GeV/c is from the decay $\psi \rightarrow \bar{p}p$, while the band at p = 1.54 GeV/c is due to the decay $\psi \rightarrow \ell^+\ell^-$, where the leptons are not unambiguously identified by the TOF system.

The problem is to compute the true flight time from the available input data. We have the TDC, the flight time measured at a given discriminator threshold for each photomultiplier, the ADC, the integral of the pulse height over the TDC time scale for each photomultiplier, and the z along the counter from the reconstruction of a drift chamber track. For each tube, we subtract a constant time due to the online alignment of the counters from the raw TDC, correct for pulse height slewing, and correct for the distance z along the counter. The measured TOF t_m is then a weighted average of the two corrected times. The weighting intrinsically prefers the photomultiplier closest to the track entrance in the scintillator as its closer proximity to the source of the scintillation light guarantees better photostatistics, hence better time resolution.

In the analysis of the TOF information, we distinguish between the π-K-p hypotheses in the following way. The flight time resolution is known (see section 2.1.4), therefore we calculate a probability P(M) for a given mass hypothesis M

$$P(M) = \frac{1}{N} \exp\left\{\frac{(t_m - t_p(M))^2}{2\sigma^2}\right\}, \qquad (5)$$

where σ is the TOF resolution, p the particle's momentum, t_m is the measured flight time, L the path length, M is the mass hypothesis,

$$t_p = L\frac{\sqrt{p^2+M^2}}{pc}, \tag{6}$$

and

$$N = \sum_i P(M_i) \quad i = \pi, K, p. \tag{7}$$

$P(M_i)$ is the normalized TOF weight.

For the purposes of this analysis, we will use the following conventions: p and K will be selected by having the highest normalized weight of the three hypotheses. In the case of bad or no TOF information, the assignment defaults to π. This is eminently reasonable due to the large fraction of π's in the data sample. Given our TOF resolution, particle identification for this thesis is relatively unambiguous.

3.2.5 Energy loss corrections

All charged particles are corrected for energy loss in the various materials between the interaction point and drift chamber layer 6. This correction is done for a 2.29 gm/cm^2 (carbon equivalent) absorber:

$$\frac{dp}{dx} = \frac{.044}{Cos\lambda} \quad \text{for } \beta > .93, \tag{8}$$

and

$$\frac{dp}{dx} = \frac{.044}{Cos\lambda}\left\{\frac{\beta_0}{\beta}\right\}^{2.65} \quad \text{for } \beta < .93. \tag{9}$$

This correction is good to within 1% for e and μ above 175 MeV/c, K above 350 MeV/c and p above 650 MeV/c.

Below these momenta, the fit does not work well and we use a more correct algorithm which explicitly integrates the range-momentum tables[36] as the particle traversed the media.

3.2.6 Charged particle fiducial cuts

Even with the great care taken in the track reconstruction program, tracks are still found which are not suitable for the analysis. These may simply be accidentals due to beam-gas events in the beam pipe and cosmic rays, or may be tracks which simply are not well reconstructed from the DAZMs. In general, one must take some care in selecting tracks involved in the analysis.

This analysis is notably free from such problems for two reasons:

1. The enormous cross section of the ψ means that a large fraction of the raw data sample is actual beam-beam events. This is untrue at any other energy range except the narrow charmonium resonances.
2. We require some sort of geometric constraint on the origin of virtually all tracks used in this analysis. In the case of the non-strange decays, this requirement is that all charged tracks eminate from a common origin, the beam-beam interaction point (see section 3.4.3). For the strange decays, this is clearly inappropriate, so we require that

the two particles eminate from a common point in space, consistent with a VEE decay (see section 3.4.2).

3. In general, we allow events to have tracks not constrained to a vertex due to accidentals and $\bar{p}$ annihilations in the LA or TOF systems which then reenter the drift chamber volume.

In the non-strange case, we in addition make requirements on the DCA of each track to the measured beam-beam interaction point:

$$r_{xy} < 1.5\text{cm}, \tag{10}$$

and

$$|z| < 8\text{cm}. \tag{11}$$

For the strange decays, cuts (10) and (11) are far too tight, and we make the very loose[37] cuts of

$$r_{xy} < 15\text{cm}, \tag{12}$$

and

$$|z| < 15\text{cm}, \tag{13}$$

with essentially all the geometrical cuts coming in the vertexing.

The measured beam-beam interaction point is determined by a previous pass over the data sample, called PASS1. The reader becomes cognizant of the mnemonics at this point. In this PASS1, Bhabha pairs are identified and tracked to a common point. This point is assumed to be the beam-beam interaction point. This position is kept track of on a run-by-run basis as, indeed, it wanders by several millimeters in the course of this data sample. The error in this beam position is convoluted with the known size of the beam from the beam position monitors, and is used when making fiducial

cuts. It is also of use in the beam constrained fit to make full use of the precision of the drift chamber and vertexing (see section 3.4.3).

3.3 PHOTON RECONSTRUCTION

3.3.1 Introduction

Between the drift chamber and the lead-liquid argon shower counters lies 1.36 radiation lengths of preradiator in the form of the coil. As a result, to maximize the low energy efficiency for photons, showers with deposited energies comparable to the detector noise must be detected. This immediately creates the problem of spurious or "fake" photons found by the service program LADRV3[38] due to detector noise. The optimal solution is thus a compromise between high efficiency and an acceptable fake rate.

3.3.2 LADRV3

Initially, a loose cut of 2σ, where σ is the RMS detector noise, is applied to each strip read out. Then, for any spatial coincidence of strips in a layer, a more stringent cut on the deposited energy (typically $\simeq$ 10 MeV) is made. Most uncorrelated noise fluctuations will fail this cut. At this level, four different algorithms are employed to determine spatial coincidences using the redundancy afforded by seven readout layers. The use of four separate algorithms maximizes the detection efficiency independent of the lateral shower development within the module. Use of all four

algorithms finds ≃ 67% more photons below 200 MeV than the single most successful algorithm.

3.3.3 Fiducial cuts

From section 3.3.2, it is clear that photon "tracks" must be thoroughly "massaged" in order to be useful in the data analysis. We mentioned in section 3.3.2 how uncorrelated detector noise could be used by the service program to form spurious photons. The problem becomes much more acute in the case of correlated detector noise. Such noise could arise from RF pickup on the detector elements or high voltage (HV) breakdown of the detector elements. Such events are easily recognized in software as having a large number n_γ of reconstructed photons in a single shower module. Consequently, we require

$$n_\gamma \text{ per module} < 5. \qquad (14)$$

In order to guarantee that photons are well contained by the shower counter, we require that the centroid of the reconstructed photon be more than two detector strips (roughly 10cm) from the edge of the module.

There is another mechanism which can create fake photons. When a charged particle, even minimum ionizing, enters the liquid argon, it deposits a certain amount of energy. LADRV3 can then combine some of this real energy with detector noise to form a fake photon. Consequently, we require

$$r_\gamma > 30\text{cm}, \qquad (15)$$

where r_γ is the distance between the photon and any charged particle at the entrance to the liquid argon system. Antiprotons often annihilate in the coil or liquid argon and deposit a large splash of energy. Therefore, we require

$$r_\gamma > 45\text{cm for antiprotons.} \qquad (16)$$

Determining the incident energy of a photon from its deposited energy is a very complex process. For the purposes of this thesis, we use only the well defined reconstructed centroid of the photon in the liquid argon and not its reconstructed energy, except as input for a kinematic fit (with large errors which essentially allow the photon energy to be free).

3.4 VERTEXING

3.4.1 Introduction

As mentioned in section 3.2.6, the use of a vertex constraint is important to the analyses in this thesis. The use of a vertex constraint increases the transverse momentum resolution of charged tracks by roughly a factor of two and significantly reduces the contribution accidentals and beam-gas events in the data sample. We will discuss two types of vertex constraints which are used in this analysis.

3.4.2 Secondary vertex constraint

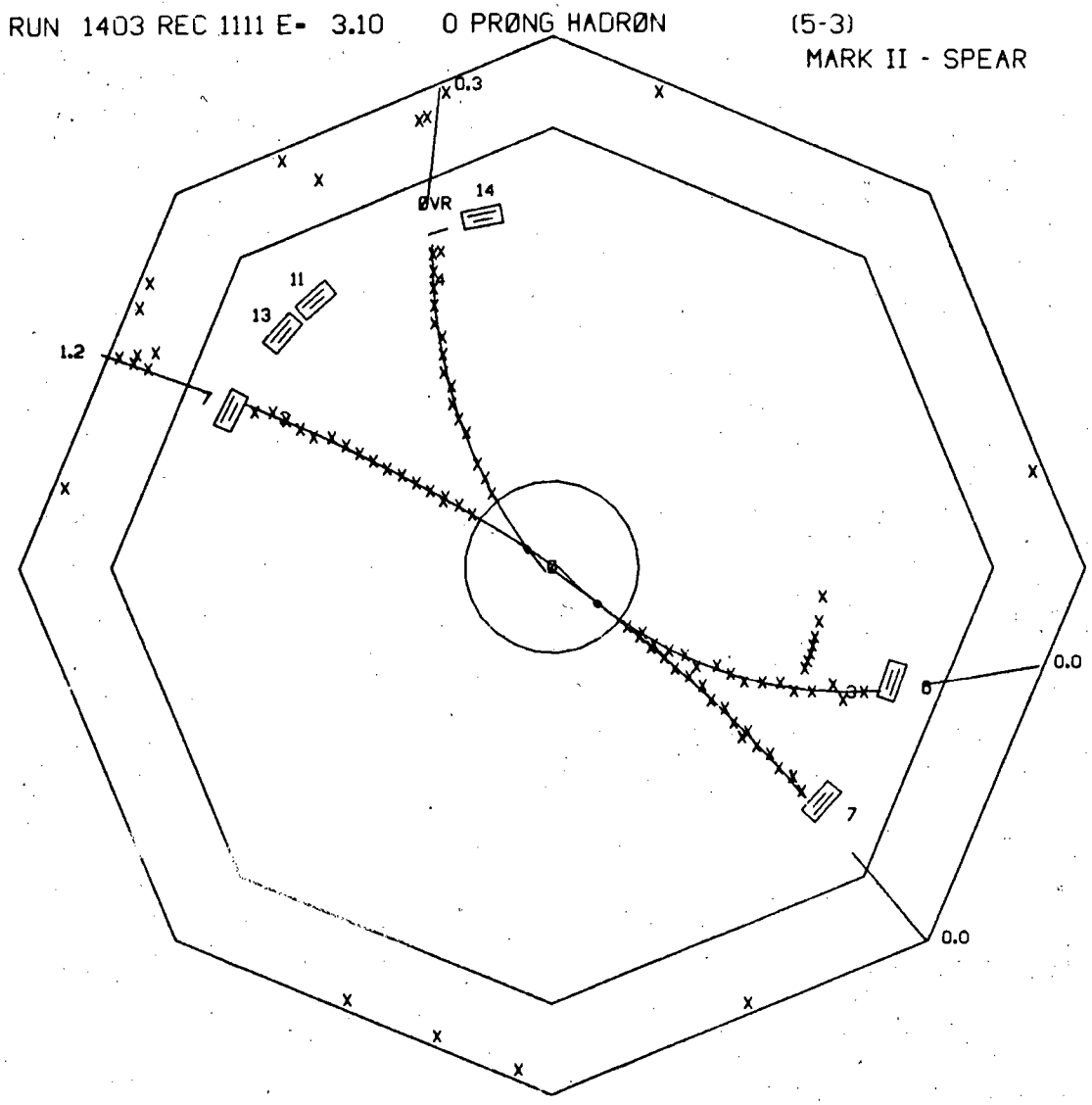

Figure 7: A $\psi \to \Lambda\bar{\Lambda}$ event. Both Λ's travel several cm in the detector before decaying. Track 1 is the proton, track 2 is the antiproton, track 3 is the π^-, and track 4 is the π^-.

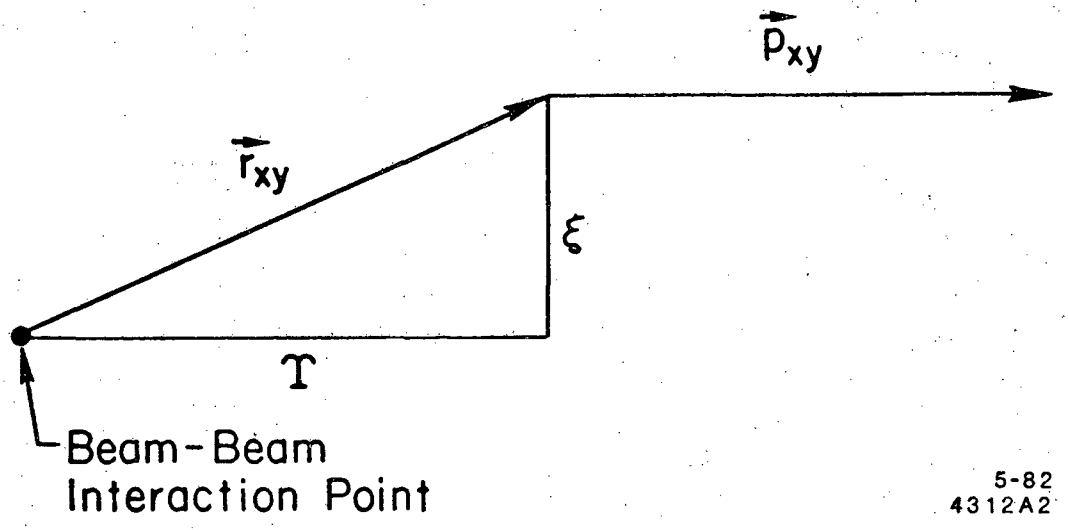

Figure 8: Diagram illustrating the ξ and τ variables.

All of the strange decays of the ψ involve weakly decaying particles. These particles consequently have relatively long lifetimes and may travel several centimeters in the detector before decaying, as shown in figure 7. Constraining these charged secondaries to the primary vertex is clearly inappropriate. Therefore, we wish to constrain these tracks to a secondary vertex spatially displaced from the primary vertex.

The service program VFINDP[39] is employed to do this. VFINDP does the secondary vertexing in the following way. At the first level, information from the one-track fits is used for pairs of tracks. These helices are circles in the xy plane. The intersec-

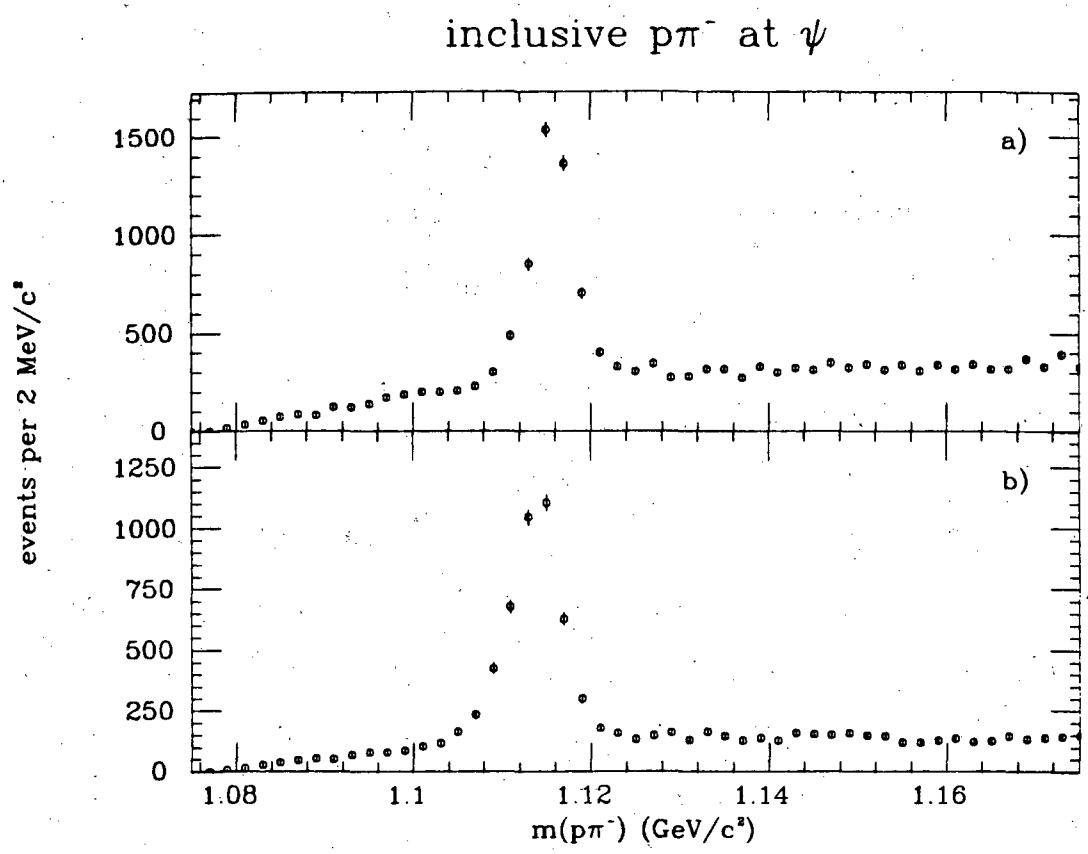

Figure 9: m(pπ⁻) before and after secondary vertex cuts.
a) without VFINDP
b) with VFINDP
The reduction in background under the Λ peak is obvious.

tions of these two circles are then examined for the geometrical crossing points of the two tracks. The cuts are as follows:

1. For maximum generality, we do not require the secondary vertex (VEE) to be significantly displaced from the primary vertex, as many VEEs do not travel significantly far from the primary vertex before decaying.

2. We make a cut on the z difference of the two tracks at the crossing point

$$|\Delta z| < 8\text{cm}. \tag{17}$$

3. Define a variable (see figure 8) ξ such that

$$\xi \equiv \frac{|\vec{p}_{xy} \times \vec{r}_{xy}|}{|\vec{p}_{xy}|}, \tag{18}$$

and require that

$$\xi < 1.5\text{cm}. \tag{19}$$

The physical significance of this is the following: A real VEE will have its momentum and decay length vectors collinear. We thus require that the component of the VEE's decay length perpendicular to its momentum be small.

4. Define a variable (see figure 8) Υ such that

$$\Upsilon \equiv \frac{\vec{p}_{xy} \cdot \vec{r}_{xy}}{|\vec{p}_{xy}|}, \tag{20}$$

and require that

$$\Upsilon > -5\text{cm}. \tag{21}$$

Note that Υ is a signed quantity unlike ξ. Physically, Υ is the component of the decay length parallel to the momentum of the VEE. This requirement is simply that the VEE decayed along its momentum vector, within errors. The effect of these cuts is to define a rectangular region about the beam-beam interaction point with the VEEs momentum vector, wherein the crossing point of the VEE secondaries must lie.

Figure 9b) shows the resultant mass distribution for Q = 0 pairs of $p\pi$ tracks which satisfy the secondary vertex cuts at this point. For comparison, figure 9a) shows the uncut distribution. These cuts provide very clean Λ identification with minimal signal loss.

At this point, the second stage of secondary vertexing begins. A loose mass cut

$$1.10 < m_{\Lambda} < 1.13 \text{ GeV}/c^2, \tag{22}$$

is made. The VEE secondaries are then swum to a common vertex using a true three dimensional swim, and constrained at the vertex. This procedure is very similar to that for the primary vertex (see section 3.4.3). A cut is made on the vertex χ^2

$$\chi^2(\text{secondary vertex}) < 16, \tag{23}$$

and a tight mass cut

$$1.110 < m_{\Lambda} < 1.122 \text{ GeV}/c^2, \tag{24}$$

are applied. For future analysis, the VEE mass is set to the known Λ mass (1.1156 GeV/c^2) and the VEE energy is recalculated. This is very similar to performing a 1C (one constraint) fit to the Λ mass.

3.4.3 Primary vertex constraint

In order to use the beam position information determined by the PASS1 analysis method mentioned in section 3.2.6, an attempt is made to constrain all charged tracks with r < 15cm to a common origin near the beam-beam interaction point, minimizing the transverse and longitudinal differences from this point. For low momentum tracks, multiple scattering becomes an effect which can signifi-

cantly deviate the reconstructed track from its actual origin. Consequently, a weight is applied to low momentum tracks in the fit. Tracks are successively removed from the fit if they contribute more than 100 to the χ^2 of the fit, then the fit is repeated. For all of the nonstrange decay analysis, we will require all charged particles to originate from this vertex.

Chapter IV

SYSTEMATICS

4.1 CHARGED PARTICLE RECONSTRUCTION

4.1.1 Drift chamber performance

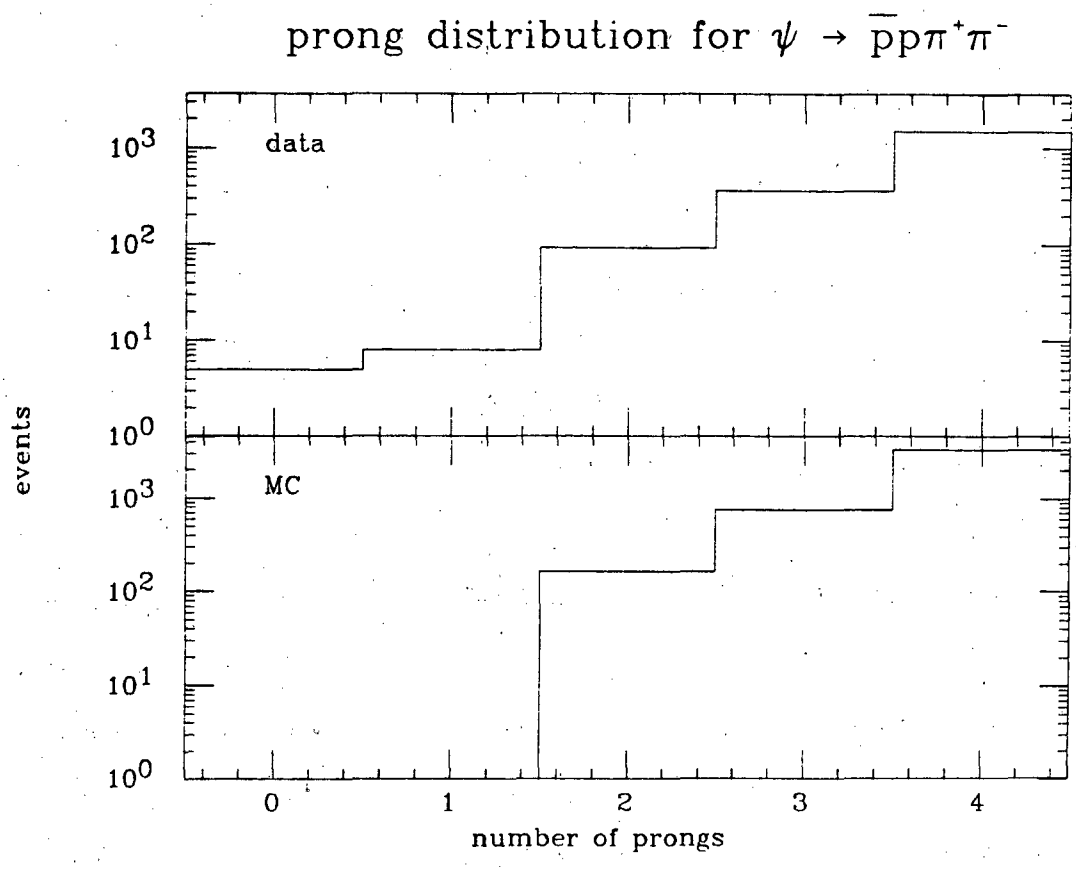

Figure 10: Prong distribution for $\psi \rightarrow \bar{p}p\pi^+\pi^-$ events.

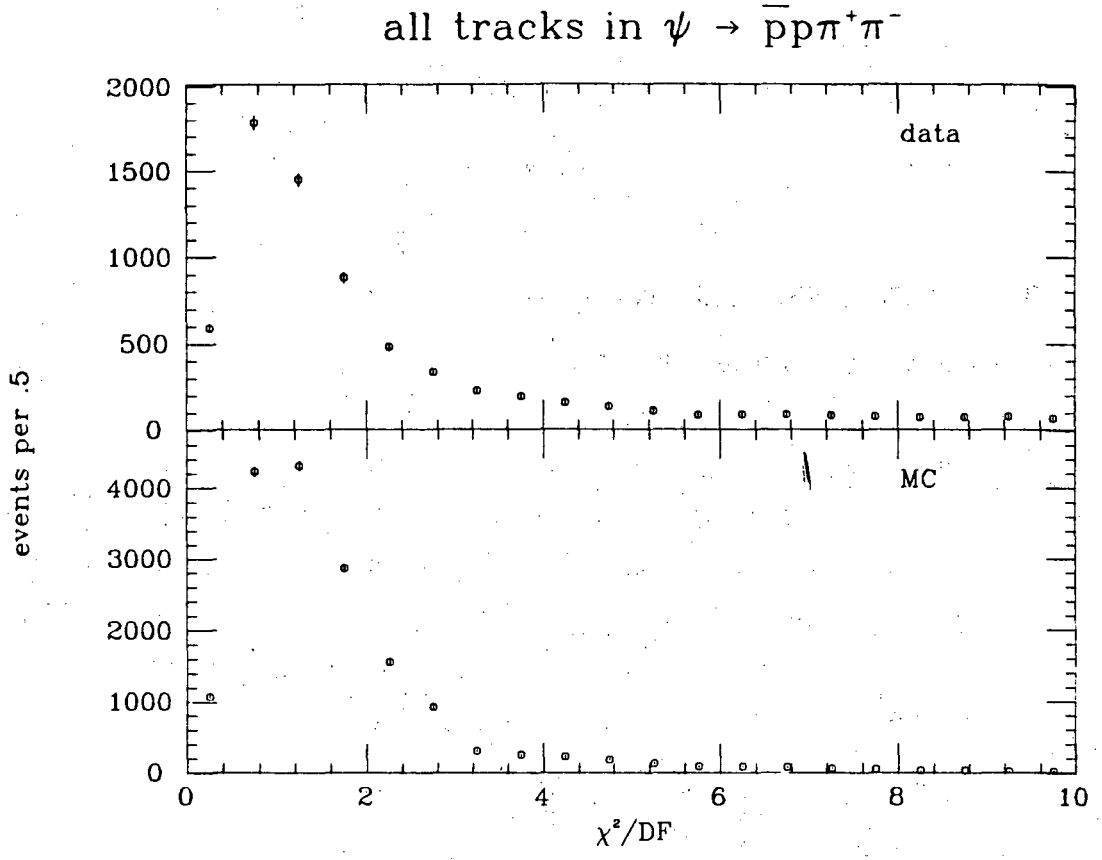

Figure 11: χ^2/DF for each track in $\psi \rightarrow \bar{p}p\pi^+\pi^-$ events.

A good measure of how well the Monte Carlo simulation program "fakes" the actual raw data is to take a clean, well understood data sample and compare it in detail with the predictions from the Monte Carlo. For these purposes, we take the decay $\psi \rightarrow \bar{p}p\pi^+\pi^-$. As discussed in section 5.8.2, this decay has the advantage of having a large branching ratio with a reasonable efficiency for a four charged particle decay. It has the disadvantage of having the decay $\psi \rightarrow \Lambda\bar{\Lambda}$ as a contaminant. These events are explicitly removed as mentioned in section 5.8.1. We are left with a data sample

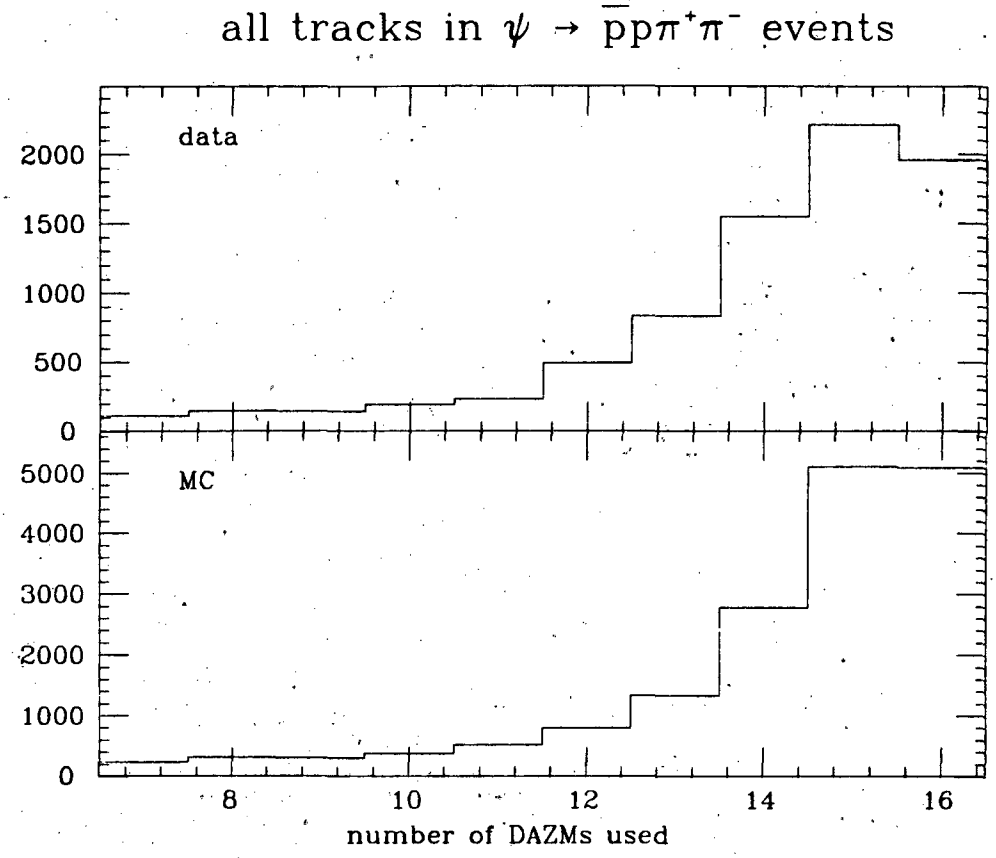

Figure 12: Number of DAZMs used for each track in $\psi \rightarrow \bar{p}p\pi^+\pi^-$ events.

wherein almost all the events are unambiguously identified as originating from ψ decays.

For this analysis, we then reanalyze the sample with no other cuts on the data other than the TOF cuts and the kinematic constraint on that the four charged tracks reconstruct to the ψ mass. This loosening of the event selection does not introduce much background as the requirement of both a proton and antiproton identified by the TOF system is a very powerful tool for eliminating

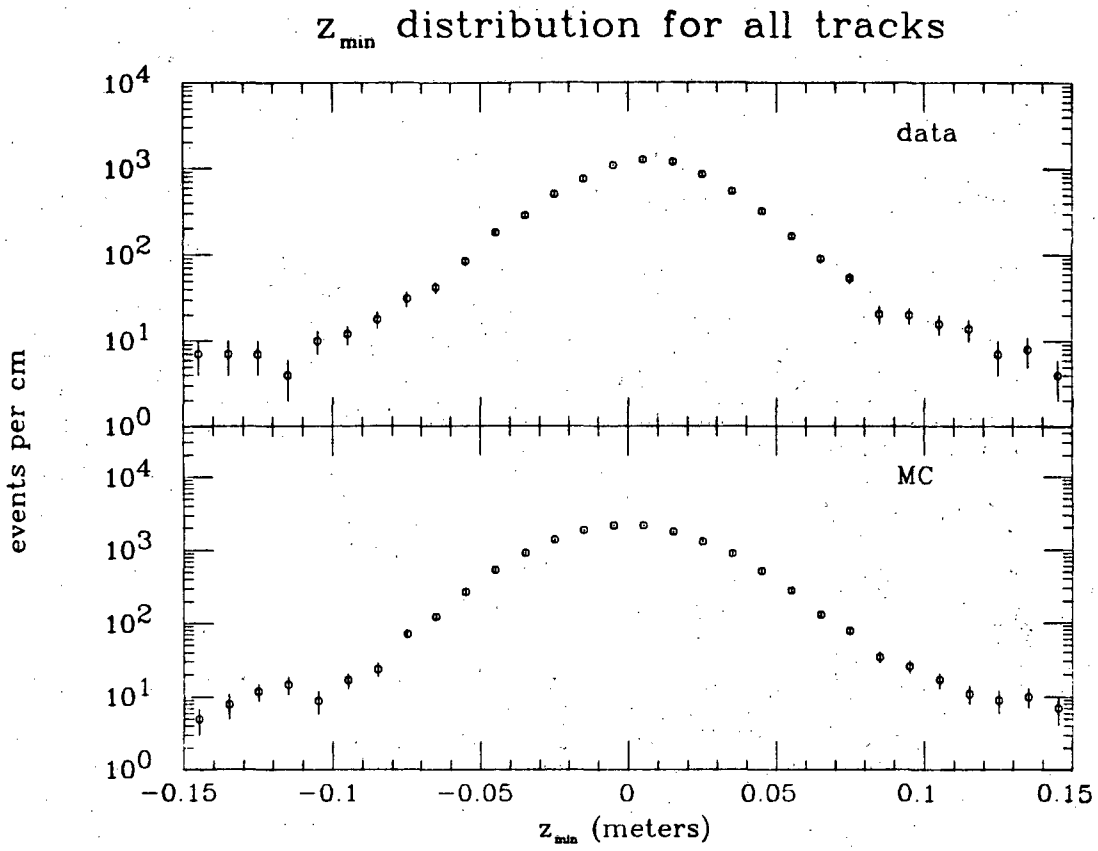

Figure 13: DCA in z direction for each track in $\psi \rightarrow \bar{p}p\pi^+\pi^-$ events.

beam-pipe and beam-gas events. We are left with a sample which allows us to check the systematics of the Monte Carlo simulation for charged tracks. In figures 10-14, we plot respectively the number of charged tracks found in the primary vertex (prongs), the χ^2/degree of freedom (DF) from the one track fits for each track in the event, the number of DAZMs used for each track during tracking, the DCA for each track in z direction, and the DCA for each track in the xy direction.

Several comments are in order:

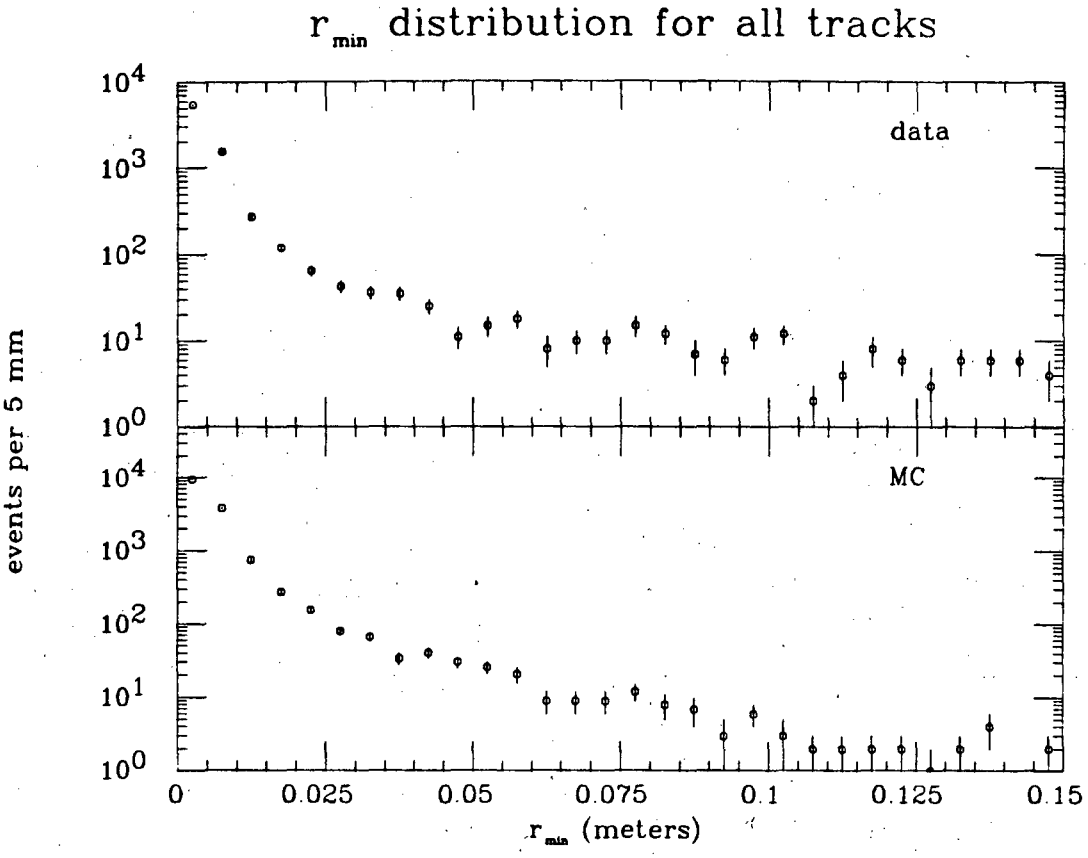

Figure 14: DCA in xy direction for each track in $\psi \rightarrow \bar{p}p\pi^+\pi^-$ events.

1. In figure 10, the data shows a smattering of 0 and 1 prong events, where a prong is defined here to be a track which reconstructs to the beam-beam interaction point, while the Monte Carlo has none. This may be due to a small residual contamination of $\Lambda\bar{\Lambda}$ events, or a small contamination of non-ψ events. Otherwise, the prong distribution agrees quite well. The large fraction of 3 prong events in both samples is doubtlessly due to low momentum tracks which mul-

tiple scatter and are not constrained to the primary vertex (see section 3.4.3). We attribute a 3.1 ± 1.3% systematic error to the four prong requirement. Two prong events are free of this problem in that almost all two prongs with r_{min} < 1.5cm will be tracked to a common vertex (the primary vertex).

2. In figure 11, the χ^2/DF plot falls off more rapidly for the Monte Carlo than for the data, probably due to nuances of drift chamber performance such as δ rays, drift cell inefficiencies, Landau fluctuations in ionization, etc., not being completely accounted for in the Monte Carlo. The surprising feature is that the distribution peaks at a higher value for the Monte Carlo sample than for the data. This is of unknown origin. Qualitatively, the agreement is still good between the two curves.
3. In figure 12, the distributions for the number of DAZMs used by the tracking program in reconstruction is in excellent agreement, except that the data shows an inefficiency for 16 DAZM tracks relative to the Monte Carlo. This may be related to the subtle problems mentioned in the previous point, or due to a lack of a detailed understanding of the drift cell inefficiency.
4. In figure 13, the z_{min} distributions agree qualitatively quite well, with slightly different shapes. The data also shows the significant offset of the beam-beam interaction

point from the physical origin of the MKII detector. As mentioned in section 3.2.6, this is corrected for in calculating the DCA of the track. Our cut of $|z_{min}| < 8cm$ is well in the tails of the distribution. We attribute a .1 ± .6% systematic error to this cut.

5. In figure 14, the two distributions again agree qualitatively quite well, with the Monte Carlo distribution falling somewhat more rapidly. There is no evidence in either distribution for an excess of tracks near r_{min} of 8cm, which corresponds to the mean radius of the vacuum chamber (see section 2.1.2). This adds confidence that we are truly seeing tracks originating from the beam-beam interaction point. Our cut of $r_{min} < 1.5cm$ looks deceptively tight on the log scale, but is well reproduced by the Monte Carlo distribution. We attribute a 2.3 ± .6% systematic error to this cut.

In conclusion, the Monte Carlo agrees qualitatively and in most cases quantitatively with the actual data distributions.

4.2 ACCURACY OF TOF SIMULATION IN THE MONTE CARLO

4.2.1 Single hit counters

We have checked the accuracy of the TOF Monte Carlo in events of the topology $\psi \rightarrow \bar{p}p$. Candidate events were selected using the following criteria:

1. We require two collinear prongs in the primary vertex.

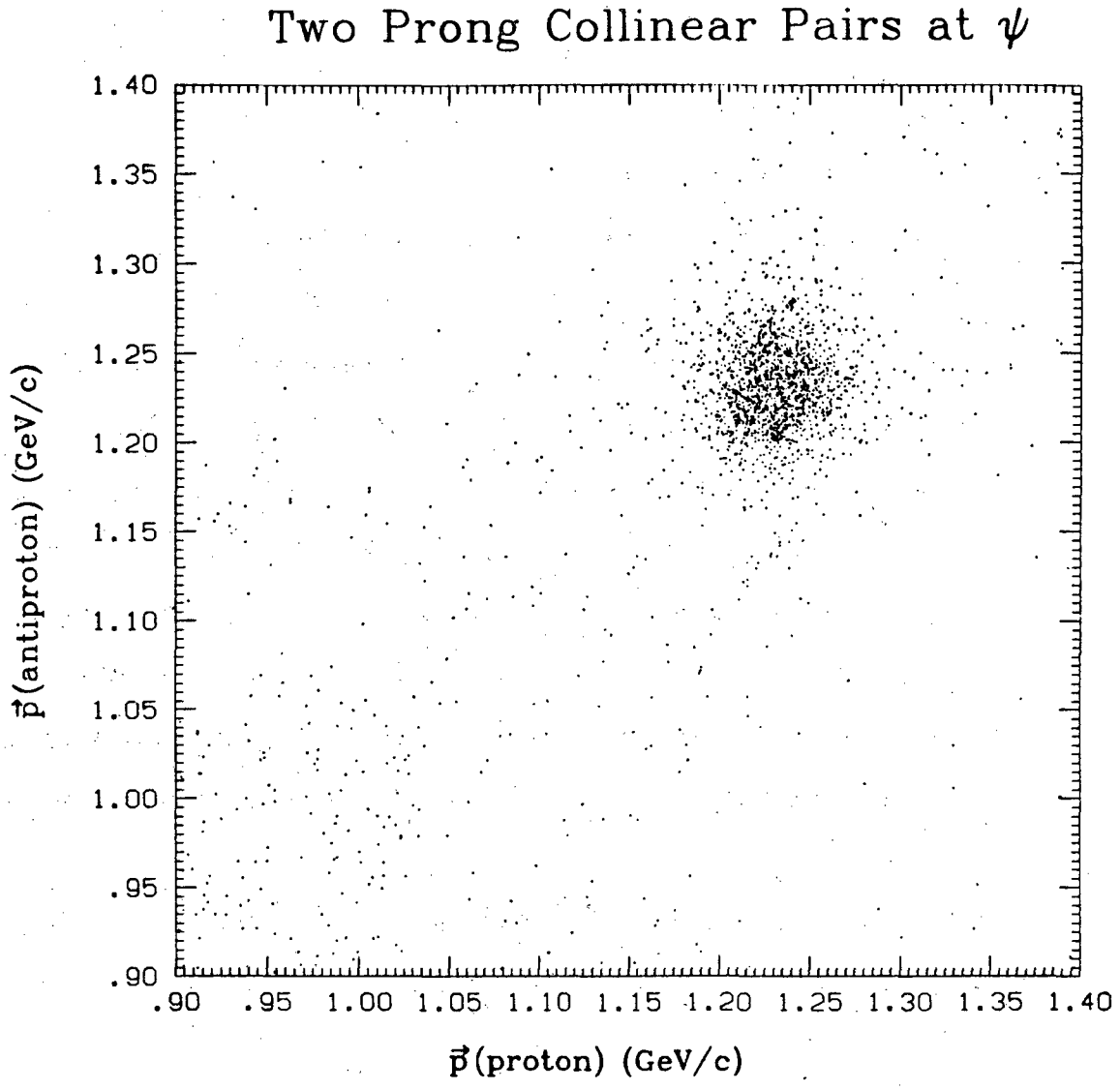

Figure 15: $\vec{p}(p)$ vs. $\vec{p}(\bar{p})$ for 2 prong collinear events. One proton is required to be identified by TOF.

2. Each track must have $|\cos\theta|$ for each track < .7.

3. <u>One</u> track must be identified as a proton.

4. In Figure 15, the momentum of one track is plotted versus the momentum of the other track. $\psi \to \bar{p}p$ events are seen to cluster in a circle about the nominal momentum of 1.23 GeV/c. We further require events to lie within a circle of radius .025 GeV/c about this nominal momentum.

Figure 15 shows this yields a very clean sample of events.

We then look at the other prong to see whether or not it was identified as a proton by the TOF system. For 111 events, only one prong was identified, while 694 had both identified. In order to estimate the (small) background contamination in the sample, we looked along the line $|\vec{p}_1| = |\vec{p}_2|$ well beyond the nominal beam momentum in an unphysical[40] region. The residual events in this region are presumably collinear cosmics with one good TOF which corresponds to a proton time. These events will filter into the sample used for the TOF efficiency. Our nonphysical region yielded 13 events. Based on the ratio of areas, we expect 4.0 ± 1.1 background events in the signal region. On the assumption these are cosmics, none of these events can have both times as protons, so we must subtract these from the sum of events which had only one proton identified. Defining N_2 as the number of events with both identified, and N_1 as the number of events with one identified, the efficiency for the TOF is defined as

$$\epsilon \equiv \frac{2N_2}{2N_2 + N_1}. \tag{25}$$

For the data, we get

$$\epsilon(\text{data}) = .926 \pm .044. \tag{26}$$

The Monte Carlo simulation had 620 events had one identified proton, and 4343 events had both identified as protons. This results in an efficiency

$$\epsilon(\text{Monte Carlo}) = .933 \pm .019. \qquad (27)$$

Comparing (26) and (27), we attribute a systematic error of .7 ± 2.6% for this data sample due to TOF system performance.

4.3 SECONDARY VERTEX SYSTEMATICS

4.3.1 Event selection

In order for us to determine the systematics due to secondary vertex constraints, we select $\psi \to \Lambda\bar{\Lambda}$ events in the same manner as in section 6.10.1, without using secondary vertex constraints. Figure 66 shows a clear $\psi \to \Lambda\bar{\Lambda}$ signal. We then compare the Monte Carlo distribution with the data distributions, as in section 4.1.1, for various VEE quantities.

4.3.2 VEE systematics

Figure 16 shows the radial decay distance r_{xy} of the VEE away from the beam-beam interaction point. Statistics are poor for the data in all of the comparisons in this section, but there is good qualitative agreement between the two distributions. We attribute a 3.7 ± 4.2% systematic error to the cut $r_{xy} > 8$mm, used only in the $\psi \to \Lambda\bar{\Lambda}$ analysis.

Figure 17 shows the mismatch in z between the two tracks due to tracking resolution. There is good quantitative agreement between

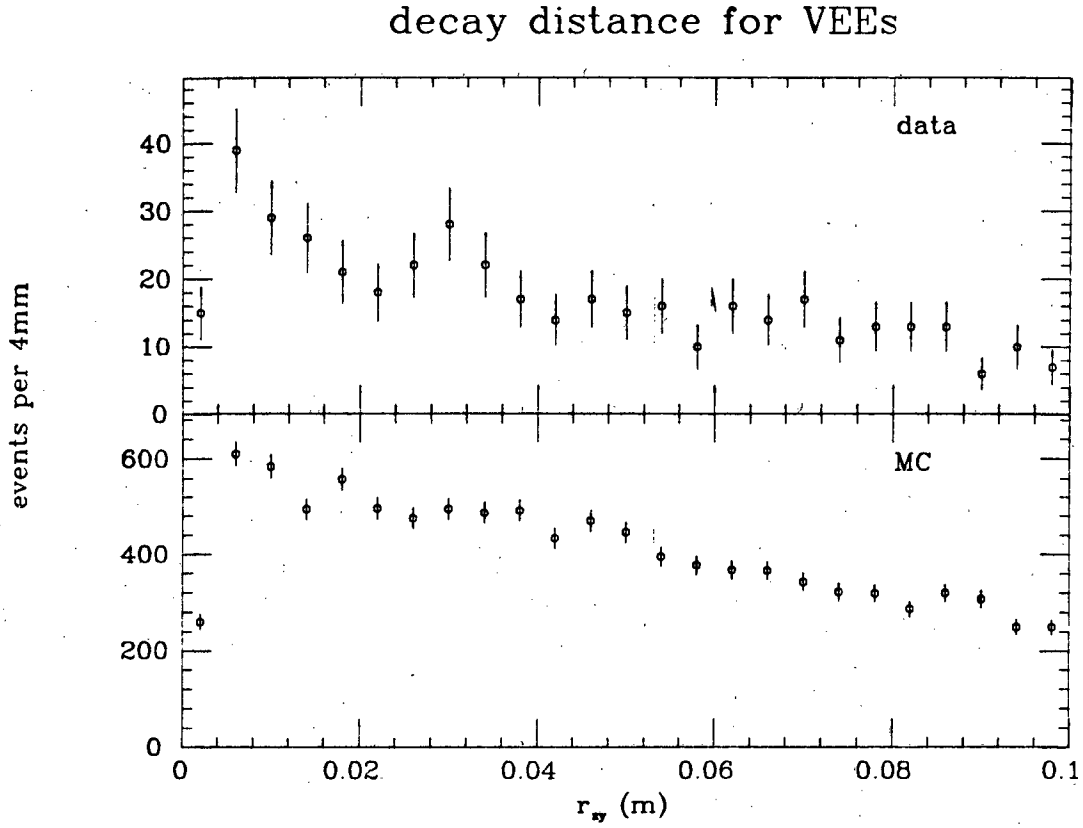

Figure 16: r_{xy} for VEEs in $\psi \rightarrow \Lambda\bar{\Lambda}$ events.

the two distributions. We attribute a 1.8 ± 4.0% systematic error to the cut $|\Delta z| < 8$cm.

Figure 18 shows the signed ξ variable (see section 3.4.2) distribution. The Monte Carlo distribution is much wider than the data distribution and also has a peculiar double hump to it. This is of unknown origin. It is also peculiar that the data distribution appears Gaussian as one might have expected. Fortunately, our cut of $\xi < 1.5$cm is quite loose and unaffected by the systematic problems in this variable. We attribute a .6 ± 4.2% systematic error in this variable.

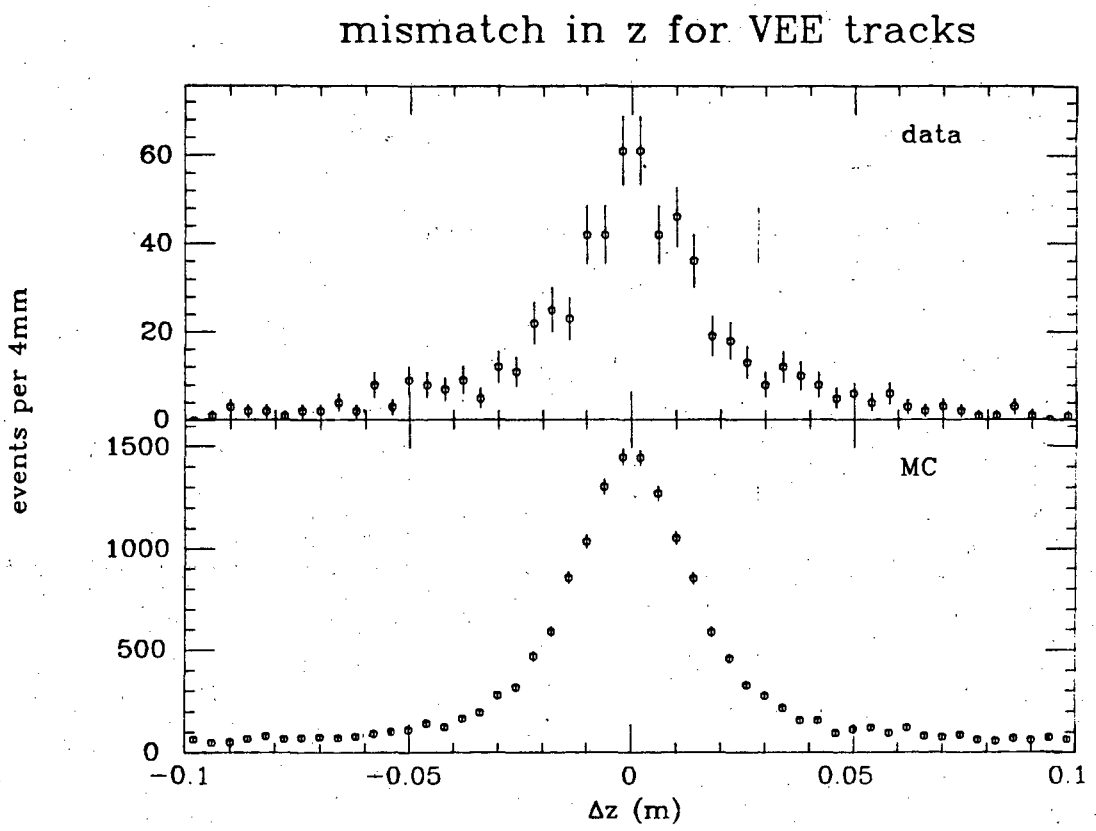

Figure 17: Δz for VEE tracks in $\psi \rightarrow \Lambda\bar{\Lambda}$ events.

Figure 19 shows the T variable (see section 3.4.2) distribution. The data distribution is in excellent agreement with the Monte Carlo. We attribute a .6 ± 4.2% systematic error to the cut T > 5cm.

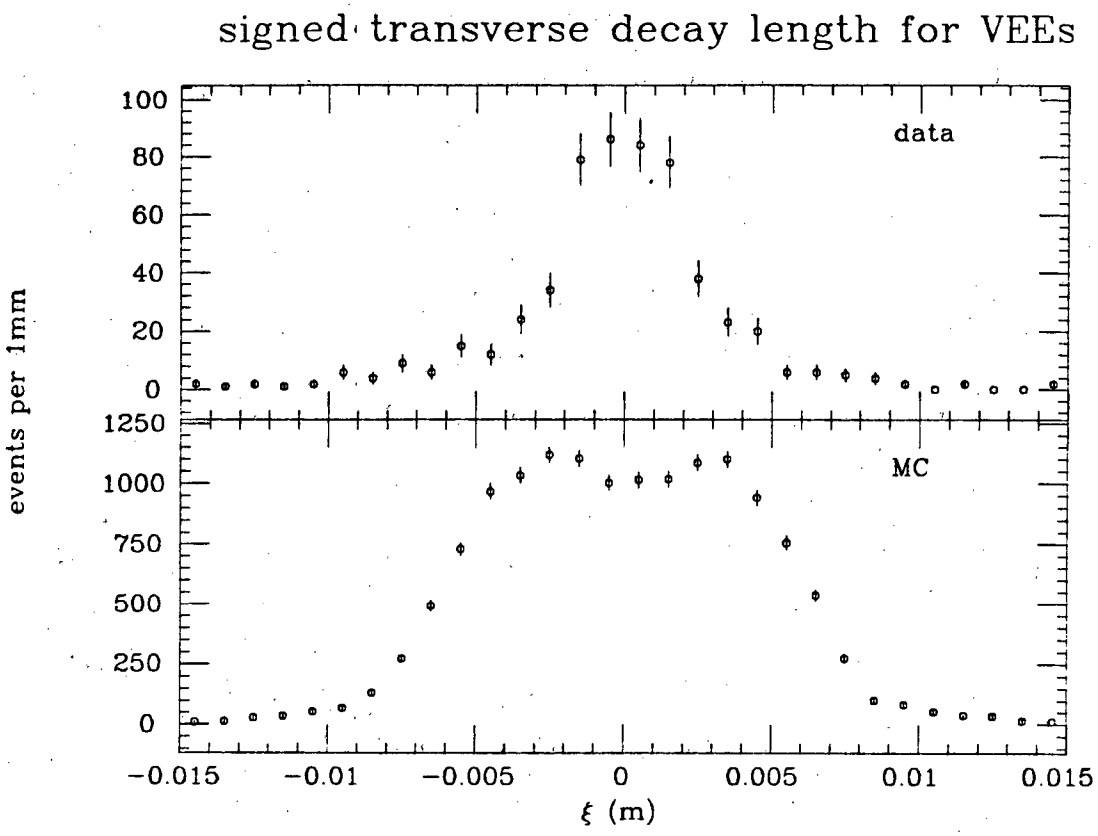

Figure 18: ξ for all VEEs in $\psi \to \Lambda\bar{\Lambda}$ events.

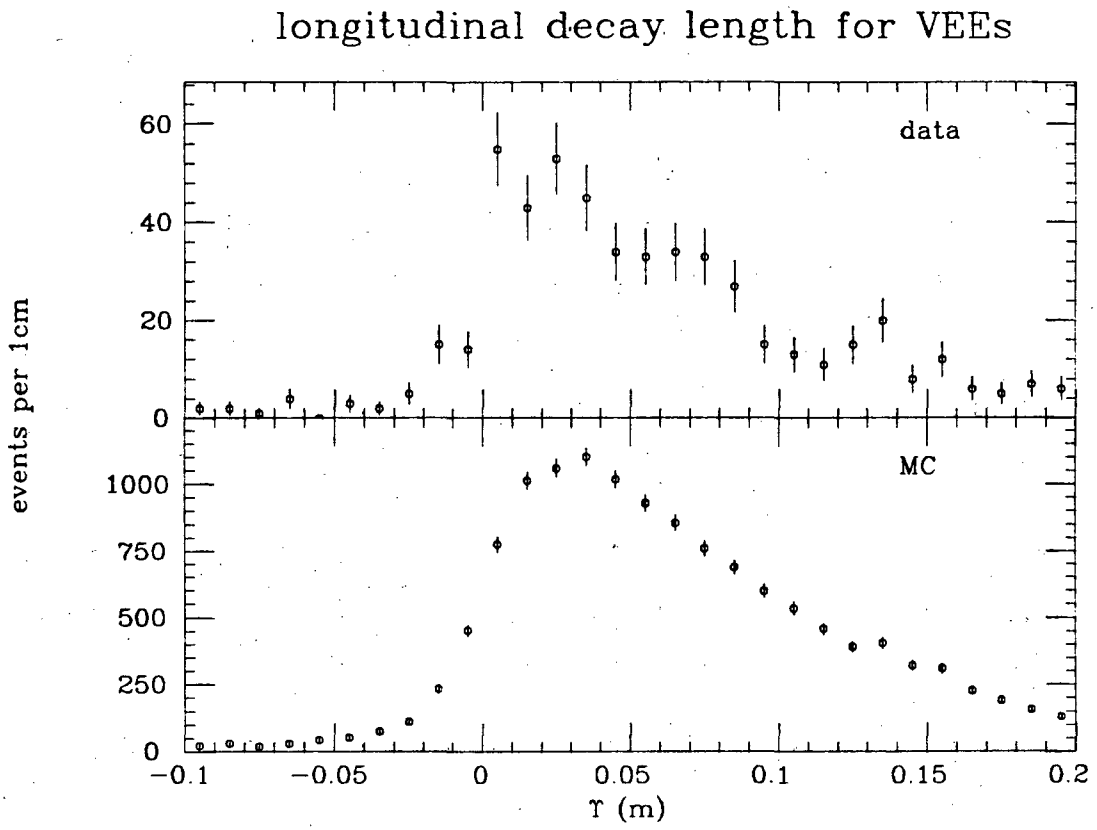

Figure 19: Υ for all VEEs in $\psi \to \Lambda\bar{\Lambda}$ events.

4.4 LUMINOSITY

4.4.1 Introduction

It is essential to this thesis to know how many ψ were produced in our data sample. This is the normalization we use to derive any branching fraction. This is typically done using a luminosity monitor, usually a small angle device which measures the Bhabha cross section where it is large. Systematics are a large problem, typically 10% without undue effort to understand the system. However, charmonium is kind to us in that it not only provides us with the

ψ, but its first radial excitation, the 2^3P_1 $\psi(3684)$ (hereafter called ψ'). In addition, the decay

$$\psi' \rightarrow \pi\pi\psi, \tag{28}$$

is roughly 30% of the total width of the ψ' and will prove to be useful for a luminosity measurement.

4.4.2 Luminosity calculation

The technique is simple; it relies on the fact that the ψ from decays of the topology (28) is essentially at rest:

1. Tag events of the topology (28) by finding the two pions from the ψ' decay which satisfy the trigger requirement.
2. Eliminate these two pions in software from the event.
3. Reanalyze the events and group them into event codes as was done for the data sample at the ψ.
4. Calculate an "efficiency" for each event code, which is the trigger efficiency for ψ decays into that event code.
5. We can now return to the ψ data sample and from the number of events in each event code, find the number of produced ψ from the number of events in each event code.

The analysis is done for different groups of event codes as a cross check on the method. It turns out there is about a 5% systematic variation for different event codes, which is added into quadrature for all branching fractions. This may be due to the tacit assumption that the ψ motion in the lab rest system is negligible, or from other considerations.

Table 1 summarizes the number of produced Ψ by run cycle for this thesis. These numbers are somewhat ad hoc since we have no preference for the results of any one set of event codes over the other.

TABLE 1

Summary of produced Ψ by run cycle

Run cycles 1 and 2	6.57×10^5
Run cycle 3 (no LA system)	6.64×10^5
ALL	1.32×10^6

4.5 SUMMARY OF SYSTEMATIC ERRORS

4.5.1 Event summary

Below we summarize the various systematic errors which we attribute to the measurements in this thesis. These errors reflect the systematic studies done in this chapter to determine systematic differences between the Monte Carlo simulation and the actual data. Note that the deviations of the Monte Carlo from the data are in almost all cases small with respect to the statistics available for the systematic study, hence we do not explicitly correct the estimated Monte Carlo efficiencies for the systematic deviations between the simulation and the actual data sample. Rather, we simply quote the error on these studies as a measure of the systematic

uncertainty between the simulation and the actual data sample. They do not reflect model dependent parameters (e.g. non-uniform phase space populations or resonances) which are estimated on a case by case basis for each decay channel.

TABLE 2

Systematic errors for various event topologies

Event topology	Systematic error
2 prong non-strange and 3 body strange decays	3.7%
4 prong non-strange decays	4.5%
2 prong strange decays ($\Lambda\bar{\Lambda}$ only)	8.4%
Other strange decays	7.4%

Chapter V

BARYON DECAYS OF $\psi(3.095)$

5.1 THE DECAY $\psi \rightarrow \bar{p}p$

5.1.1 Data reduction

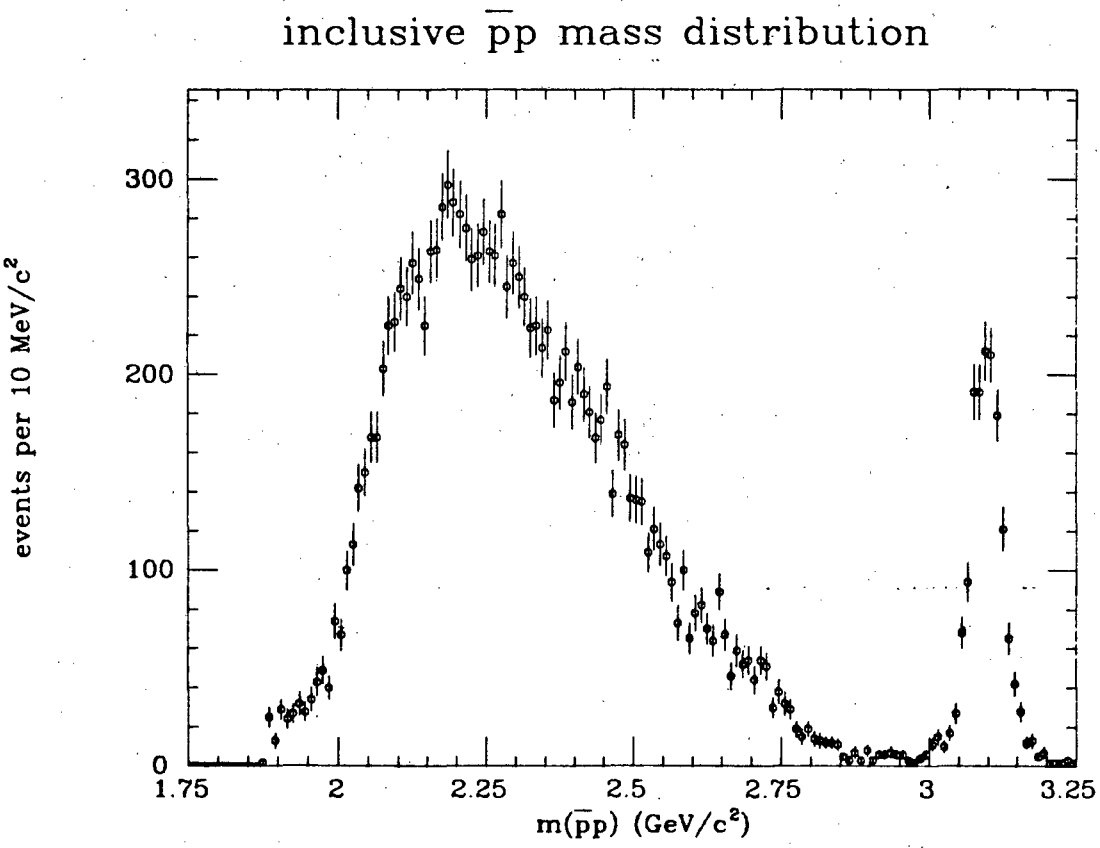

Figure 20: $\bar{p}p$ mass for all pairs.

Candidate events are required to have exactly two oppositely charged protons in the primary vertex. The invariant mass distribution of the $\bar{p}p$ system for these events is shown in figure 20. There is a clear signal of events centered near 3.1 GeV/c^2, which we attribute to the decay

$$\psi \rightarrow \bar{p}p. \tag{29}$$

Both tracks must have $|\cos\theta| < .7$ so that events are well contained in the central detector. We define the signal region as $3.02 < m(\bar{p}p) < 3.17$ GeV/c^2, therefore eliminating events far in the tails of the mass distribution.

5.1.2 Angular distribution of $\bar{p}p$ pairs

There are

$$1420 \pm 37 \text{ events,} \tag{30}$$

which satisfy these criteria. For these events, we plot $dN/d(\cos\theta)$ of the pair in Figure 21, where $\cos\theta$ is now the angle between the proton direction and the positron beam direction. From the phase space Monte Carlo an efficiency is estimated for the pairs as a function of the polar angle $\cos\theta$. This efficiency is found not to vary in the region $|\cos\theta| < .7$, therefore we may determine the angular distribution of $\bar{p}p$ pairs directly from the detected distribution.

A fit is done using the program MINUIT[41] to the detected distribution of the form

$$\frac{dN}{d(\cos\theta)} = N_0(1 + \alpha\cos^2\theta) \tag{31}$$

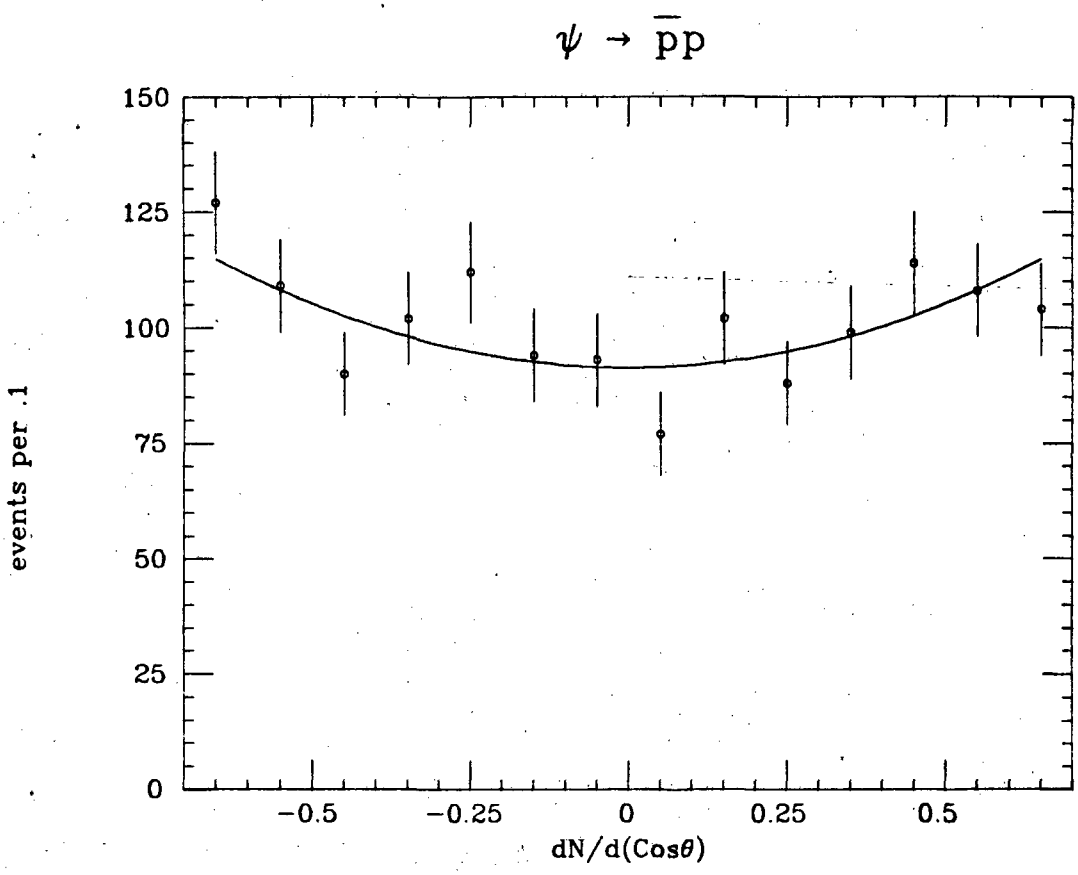

Figure 21: Angular distribution of $\bar{p}p$ pairs from the ψ.

where N_0 is an overall normalization and α is a measure of the deviation of the production distribution from flat. The results of such a fit give

$$\alpha = .61 + .23 - .22 \qquad (32)$$

where the χ^2 of the fit is 12.6 for 12 degrees of freedom (DF).

5.1.3 Efficiency calculation and branching fraction

In our simulation, we assumed that the distribution of $\bar{p}p$ pairs was flat in the polar angle. As we have just shown, such is not the case. In order to determine the branching fraction for $\psi \rightarrow \bar{p}p$, we must correct our efficiency estimate for the observed angular distribution of pairs.

In the case of a flat angular distribution, we estimate an efficiency of

$$\epsilon(\text{flat angular distribution}) = .544. \tag{33}$$

We now must fold in the non-flat angular distribution of pairs. Since the acceptance is flat over $|\text{Cos}\theta| < .7$, the Monte Carlo has overestimated the acceptance by

$$\frac{\int_0^1 d(\text{Cos}\theta) \times \int_0^{.7} (1 + \alpha_m \text{Cos}^2\theta) d(\text{Cos}\theta)}{\int_0^1 (1 + \alpha_m \text{Cos}^2\theta) d(\text{Cos}\theta) \times \int_0^{.7} d(\text{Cos}\theta)} = .914. \tag{34}$$

where α_m is the measured angular distribution. This gives for the geometrically corrected acceptance

$$\epsilon = .497. \tag{35}$$

Our result is then

$$BR(\psi \rightarrow \bar{p}p) = (2.16 \pm .07 \pm .15) \times 10^{-3}, \tag{36}$$

where in this and all following cases the first error is statistical and the second systematic. We have included a systematic error of $.07 \times 10^{-3}$ due to the measured angular distribution (32) of $\bar{p}p$ pairs.

5.2 THE DECAY $\psi \to \bar{p}p\gamma$

5.2.1 Introduction

Direct photon decays of heavy onia states have been the subject of much discussion recently.[24,25,42-53] Not all of the total direct photon contribution has been accounted for by exclusive decays of the ψ, such as $\gamma\pi^0$, $\gamma\eta$, $\gamma\eta'$, $\gamma f(1270)$, and the recently discovered[54] $\gamma\iota(1420)$ and[55] $\gamma\theta(1640)$. We present evidence for the first observation of an exclusive final state involving baryons opposite the direct photon.

5.2.2 Data reduction

Candidate events are selected using the following criteria:

1. We require exactly two oppositely charged tracks coming from the primary vertex, both of which must be identified protons.
2. We cut on the final state kinematics of the proton antiproton pair to eliminate multi-pion final states. We use the variable $U \equiv E_{miss} - p_{miss}c$, and require that

$$-.07 < U < .06 \text{ GeV}. \qquad (37)$$

Note that U is related to mm^2 by the simple relationship

$$mm^2 = E^2_{miss} - p^2_{miss}c^2$$
$$= (E_{miss} + p_{miss}c)U. \qquad (38)$$

The effect of this cut is illustrated in figure 22. There is a distinct band roughly centered about $U = 0$, which corresponds to the missing $\gamma(\pi^0)$ hypothesis. The advantage of

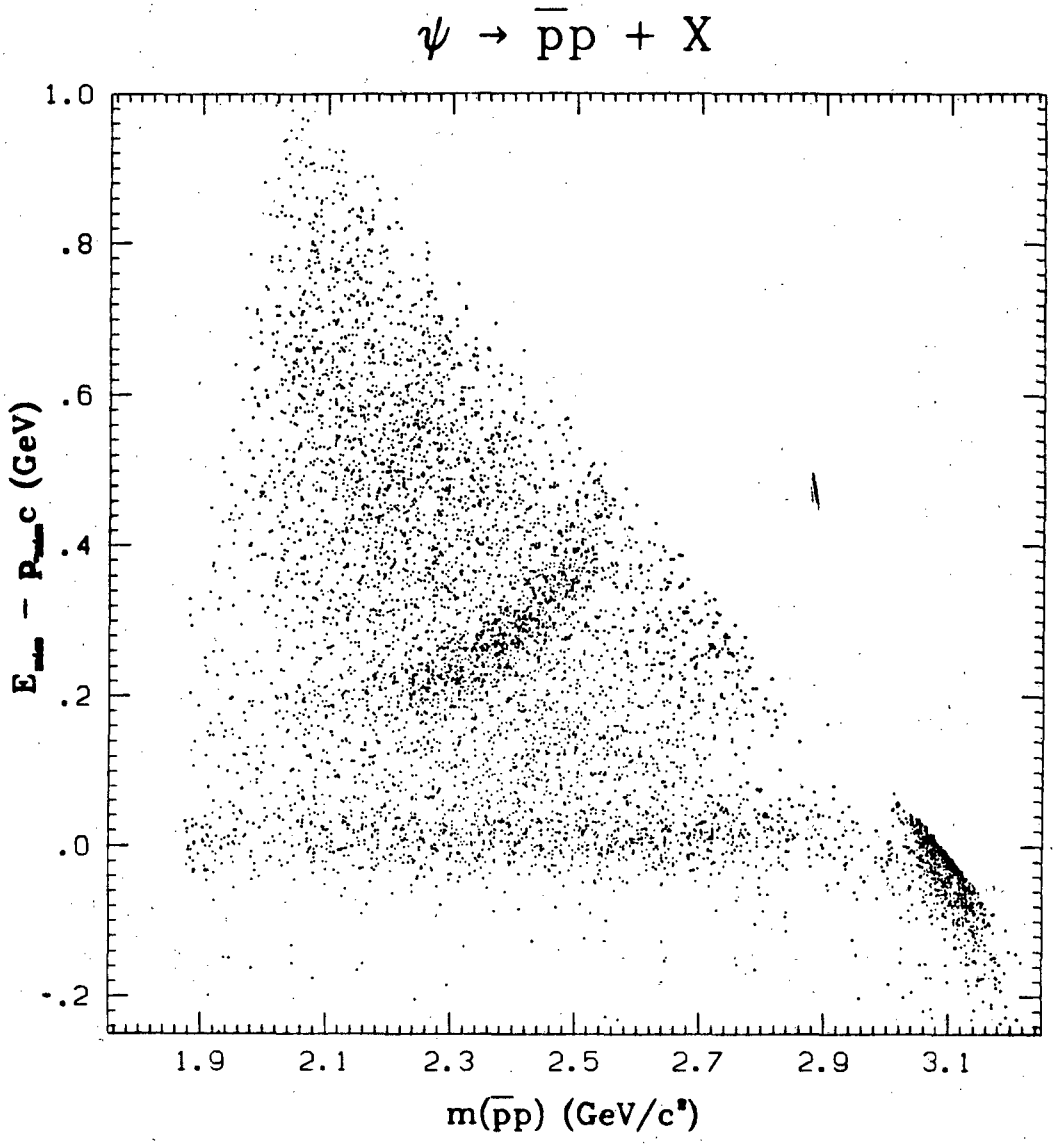

Figure 22: Scatter plot of $\bar{p}p$ mass versus U, all $\bar{p}p$ pairs. The band in the vicinity of U = .3 is due to the decay $\psi \rightarrow \bar{p}p\eta$.

the variable U is that the error in the quantity U is to first order insensitive to the energy of the missing $\gamma(\pi^0)$, whereas the error in mm^2 is proportional to the energy of

the missing $\gamma(\pi^0)$. This cut essentially removes all multi-pion final states opposite the proton antiproton pair, while losing very little of the single $\gamma(\pi^0)$ signal.

3. It is impossible to discern between the reactions

$$\psi \rightarrow \bar{p}p\gamma, \tag{39}$$

and

$$\psi \rightarrow \bar{p}p\pi^0, \tag{40}$$

in the MKII detector without photon detection, as our resolution in mm^2 is not good enough. In the course of the data taking at SPEAR during the spring of 1978, the liquid argon shower system was discovered to have an impurity in it which destroyed its sampling capability for electromagnetic showers. The system was consequently inoperable for a few weeks until the impurity could be removed by replacing the liquid argon supply. This time unfortunately corresponded to the cycle 3 data sample at the ψ, so the data sample for this analysis is correspondingly restricted to run cycles 1 and 2 data when the liquid argon system was functional.

4. We allow more than 1 photon per event. Additional photons frequently occur due to noise hits in the LA.

5. LA storm events (see section 3.3.3) are used in the analysis, but are so few in number as to not significantly alter the analysis.

6. Events are hand scanned for other problems.

7. Events with $m(\bar{p}p) > 2.97$ are eliminated to remove $\psi \rightarrow \bar{p}p$ events which couple with noise photons to form spurious events. Note that no real events will be eliminated as the efficiency due to the 1.36 radiation length coil is near zero below 100 MeV.

5.2.3 q^2 of observed photon

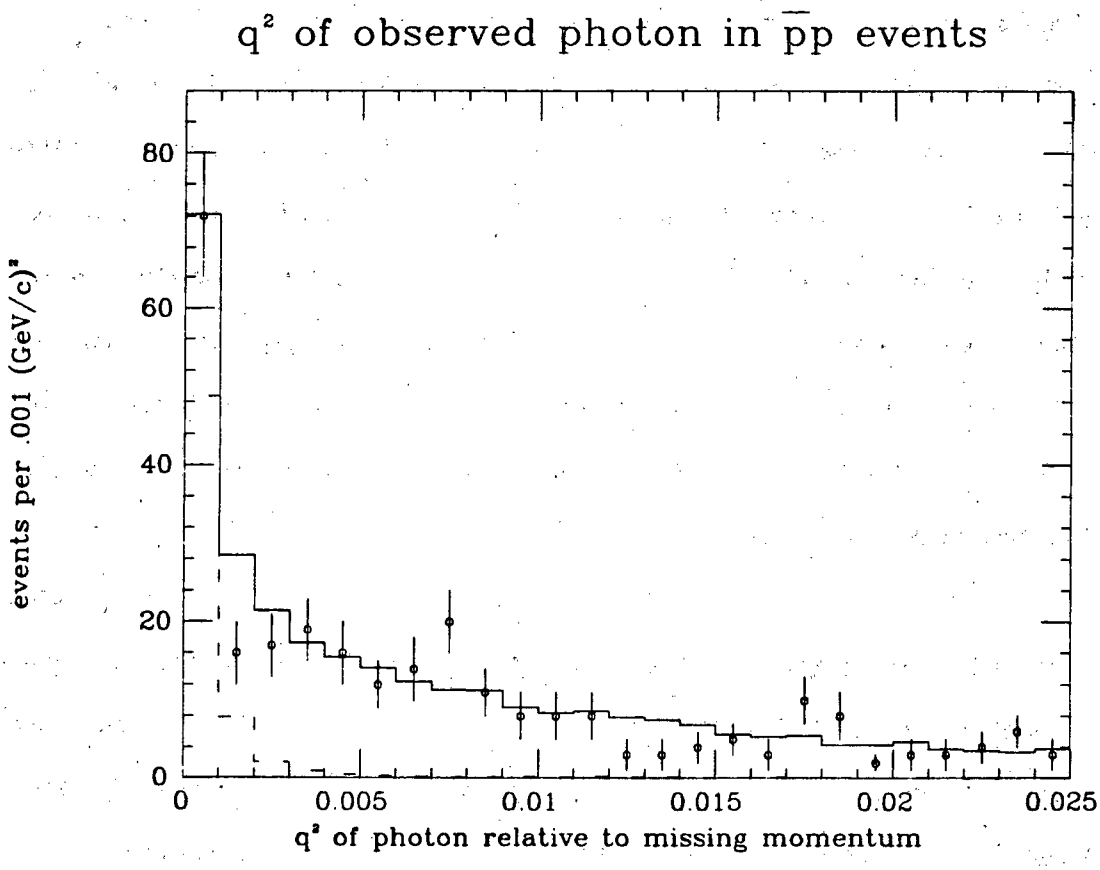

Figure 23: q^2 of observed photons. Solid histogram is expected contribution from sum of π^0 and γ decays, discussed in text. Dot-dashed histogram is direct photon contribution only.

The q^2 of the photon relative to the missing momentum p_{miss} is defined as

$$q^2 = 4p^2_{miss}\sin^2\frac{\theta}{2}, \tag{41}$$

where θ is the angle between the observed photon direction and the direction of the missing momentum. It is important to note that the observed energy of the photon in the liquid argon is not used, only the reconstructed location of the photon in the liquid argon. The q^2 of the observed photon is plotted in figure 23. The reactions under study exhibit markedly different characteristics[56] for the decays under study. The q^2 distribution of direct photon events is very strongly peaked, with $\simeq$ 80% of the events having $q^2 < .001$ $(GeV/c)^2$, while the q^2 distribution of π^0 events is much more gently peaked. There is a significant excess of events with $q^2 < .001$ $(GeV/c)^2$, which we attribute to the decay $\psi \to \bar{p}p\gamma$. Initial state radiation, which in principle could contaminate the sample with the reaction

$$e^+e^- \to e^+e^-\gamma \to \bar{p}p\gamma, \tag{42}$$

where the radiation of the photon occurs in the initial state, can be shown not to contribute due to the very small form factor for $e^+e^- \to \bar{p}p$ off resonance.[57] The region $q^2 < .001$ (GeV/c^2) will subsequently be referred to as the direct photon signal region.

5.2.4 Noise photons, π^0 subtraction and branching fraction

Since we do not explicitly use the photon energy, the possibility of a real $\psi \to \bar{p}p\pi^0$ event coupling with a noise photon to fake a direct photon event must be investigated. The kinematics for the event provide strong constraints on this background. The observed missing momentum spectrum averages to $\simeq .45$ GeV/c. The requirement that the q^2 of the photon relative to the missing momentum of the $\bar{p}p$ system be $< .001$ $(GeV/c)^2$ means that the average $(\Delta\theta)^2$ of the photon relative to the missing momentum is $\simeq 5\times10^{-3}$. The fraction of the total liquid argon solid angle subtended by a cone of this $(\Delta\theta)^2$ is $\simeq 7\times10^{-4}$. From figure 22 we deduce that there are $\simeq 400$ $\bar{p}p\pi^0$ events in run cycles 1 and 2 which have missing momentum that points into the liquid argon fiducial volume. Assuming the fake distribution in the liquid argon is uncorrelated with the missing momentum of the $\bar{p}p$ system, we expect the <u>total</u> number of fake events to be $\simeq .3\times$(fake occupancy per event). Based on a hand scan of $\psi \to \bar{p}p$ events, the mean fake occupancy, weighted by luminosity, is < 1 per event over all eight modules (including storm events), so the number of expected fake events is $< .5$ out of a sample of 49, insignificant relative to the statistical error.

The remaining background in the signal region comes from highly asymmetric decays of π^0's from the decay $\psi \to \bar{p}p\pi^0$. The subtraction of this background may be ascertained from taking a control region $.003 < q^2 < .01$ $(GeV/c)^2$, where the direct photon contribution is negligible. Monte Carlo events of the topology $\psi \to \bar{p}p\pi^0$ are gener-

ated using the full EGS3[58] shower simulation code, according to a phase space distribution. The q^2 distribution is calculated for these events. This distribution is renormalized to the number of events in the control region. The renormalized distribution is then subtracted from the data. We obtain an excess of

$$49 \pm 9 \text{ events,} \tag{43}$$

for $q^2 < .001$ $(GeV/c)^2$, which we ascribe to the decay $\psi \to \bar{p}p\gamma$ (39).

A phase space Monte Carlo is used to renormalize the q^2 distribution to the number of signal events in the bin $q^2 < .001$ $(GeV/c)^2$, shown as a dot-dashed histogram in figure 23. This distribution is then added to the renormalized π^0 Monte Carlo distribution to produce the solid histogram in figure 23. The data agrees well with the Monte Carlo. Using all eight barrels, we estimate an efficiency of

$$\epsilon = .204, \tag{44}$$

for the direct photon decay, and

$$\epsilon = .176, \tag{45}$$

using only seven of eight modules, corresponding to the death of module 8 during run cycle 1 data taking, and a correction of .99 due to "dead" modules in storm events ($n_\gamma > 4$). From this, we deduce a luminosity weighted efficiency of

$$\epsilon = .195, \tag{46}$$

where in all cases we have folded in the photon energy spectrum. Our result is

$$BR(\psi \to \bar{p}p\gamma) = (.38 \pm .07 \pm .07)\times 10^{-3}. \tag{47}$$

where we have folded in another factor of 5% systematically in quadrature allowing for uncorrelated errors between the π^0 and the γ simulations with a 15% model dependent error due to our uncertainty regarding acceptance variations over the available phase space.

5.2.5 $\bar{p}p\pi^0$ branching fraction

As a byproduct on what we have done, we can determine the branching fraction for $\psi \to \bar{p}p\pi^0$ using the q^2 distribution. Our control region is essentially free from all other backgrounds, and we have

$$69 \pm 8 \text{ events}, \tag{48}$$

for which we estimate an efficiency of

$$\epsilon = .074, \tag{49}$$

including module 8 correction.

Thus,

$$BR(\psi \to \bar{p}p\pi^0) = (1.42 \pm .16 \pm .25)\times 10^{-3}, \tag{50}$$

where we have included a 15% model dependent systematic uncertainty as above.

Finally, note that this number will (see section 5.4.2) be improved by not requiring photon detection for the branching fraction.

5.2.6 x spectrum of direct photons

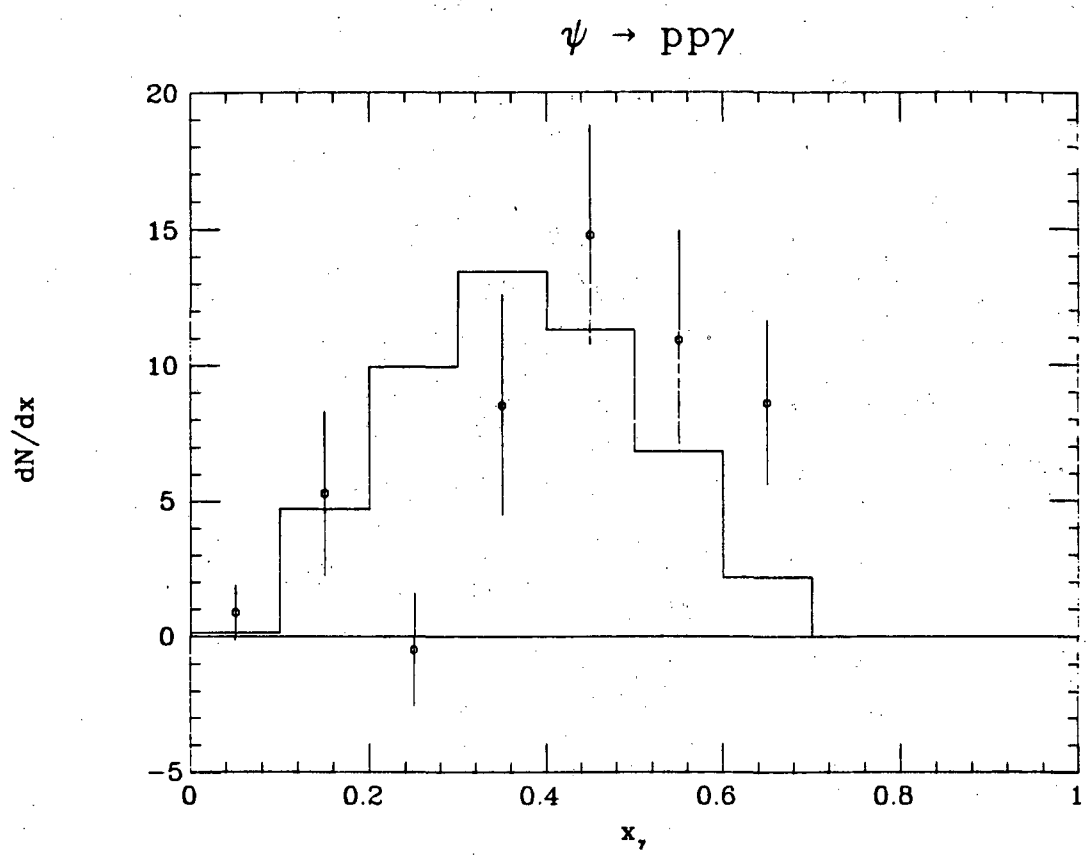

Figure 24: x_γ distribution, expected π^0 component subtracted. Solid histogram is first order QCD prediction.

The spectrum of direct photons from heavy onia is also of interest[43] since it may be calculated to first order in QCD. Now that the background is understood in the signal region, we may extract the direct photon spectrum from the observed x_γ spectrum, where

$$x_\gamma = \frac{p_{miss}}{E_{beam}}. \qquad (51)$$

First of all, we must subtract out the expected background from π^0 contamination. This is done bin by bin as for the q^2 distribution. Finally, the x_γ spectrum is corrected bin by bin for detection efficiency to produce the gamma spectrum shown in Figure 24. The first order QCD prediction,[24] assuming massless gluons, essentially reproduces phase space for $x < .85$, This prediction is modified by the substantial phase space occupied by the $\bar{p}p$ pair and is shown as a solid histogram in figure 24. This modification explains the cutoff beyond x_γ of .7 in the data due to the limited phase space available to the photon.

5.2.7 $\bar{p}p$ mass spectrum

One may also derive the mass spectrum of proton antiproton pairs opposite the direct photon by inverting the x_γ spectrum and subtracting out the expected contribution from the decay $\psi \rightarrow \bar{p}p\pi^0$. If the direct photon decay proceeds via $\psi \rightarrow gg\gamma$, where the final state hadrons result from the fragmentation of the two gluons, the possibility of a two gluon bound state exists.[25,43] The subtracted $\bar{p}p$ mass spectrum is shown in figure 25. There is a tantalizing enhancement just above threshold, but with limited statistics we can draw no definitive conclusions.

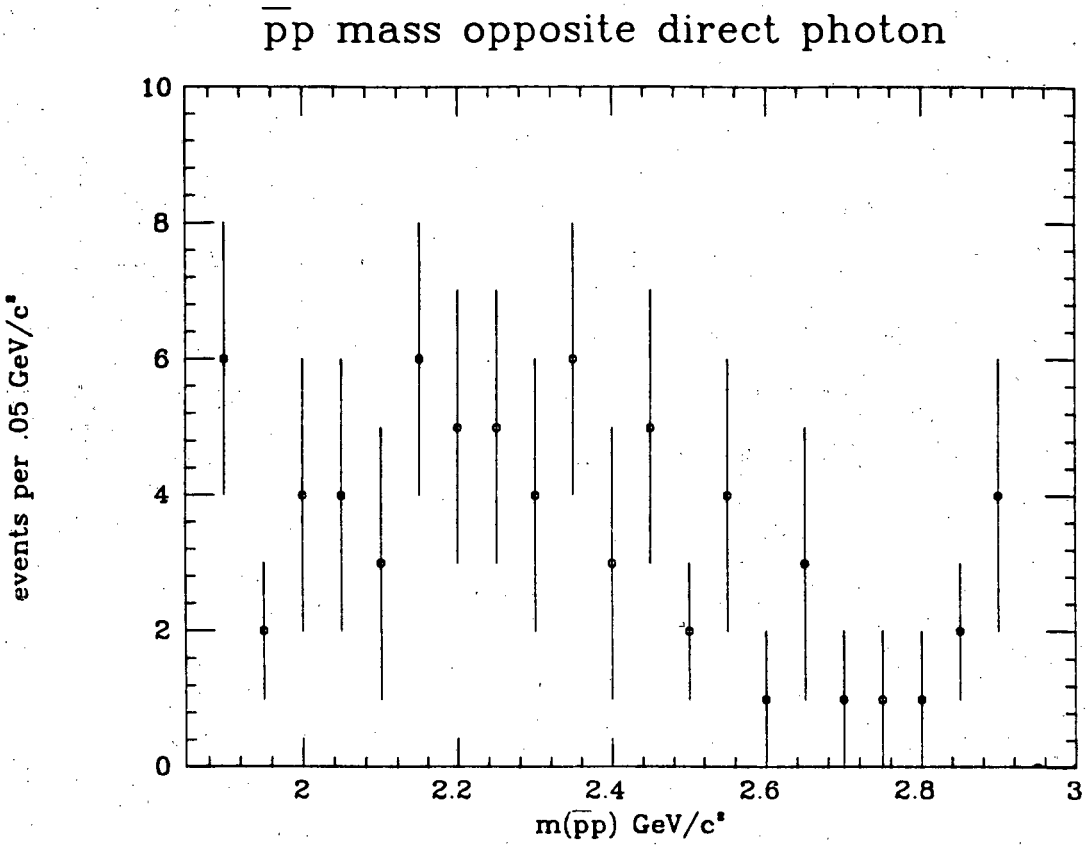

Figure 25: Mass of $\bar{p}p$ pairs opposite direct photons, π^0 background unsubtracted. The rise near 2.9 GeV/c^2 is probably due to $\psi \rightarrow \bar{p}p$ events coupling with noise photons, as the q^2 cut is not very stringent for low momentum photons.

5.3 THE DECAYS $\psi \rightarrow \bar{p}\pi^+n$ + c.c.

5.3.1 Data reduction

Candidate events are required to have exactly two oppositely charged tracks in the primary vertex, one identified as a proton, the other a pion. There must be no VEEs in the event, to eliminate photon conversions and Λ's. Each track must have $p < 1.4$ GeV/c, to eliminate radiative Bhabha pairs from the sample. For these

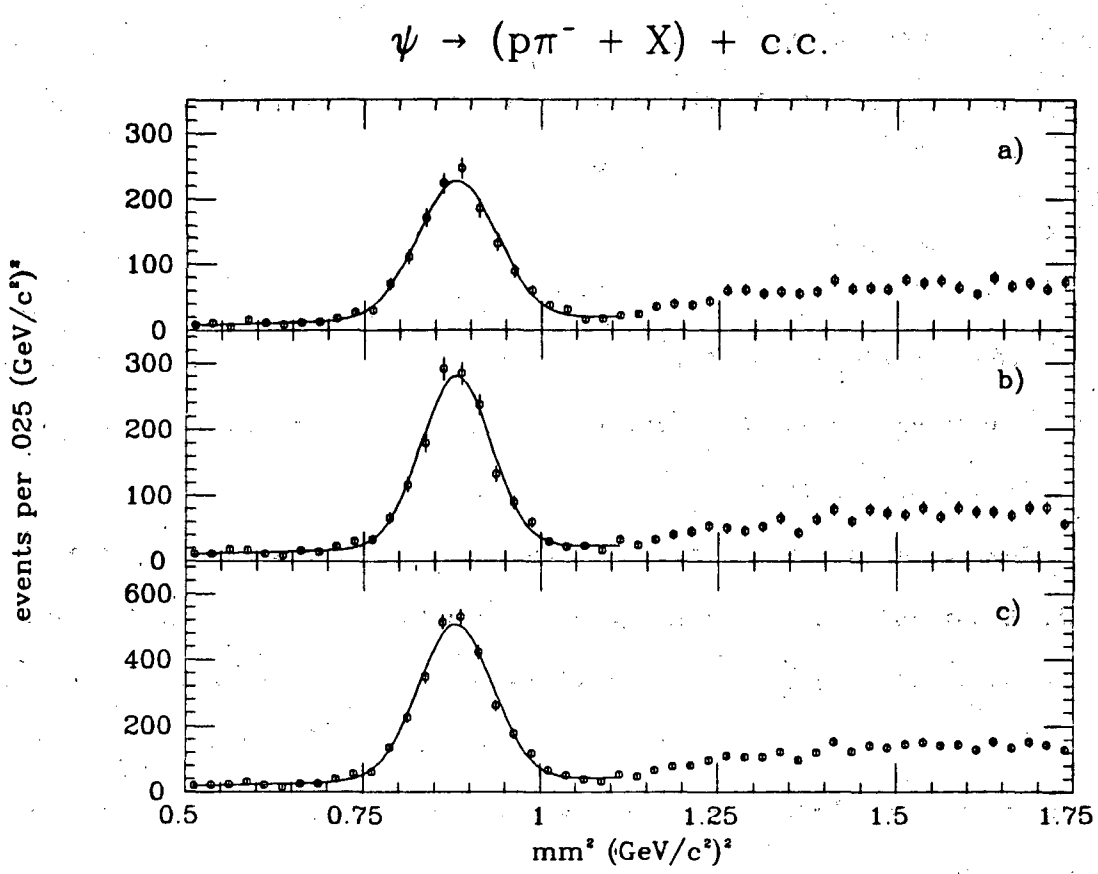

Figure 26: mm^2 against Nπ system.
a) $p\pi^-$
b) $\bar{p}\pi^+$
c) both charge modes

events, we plot the mm^2 opposite the $p\pi$ system in figure 26, for each charge mode separately as well as the sum. There exists a clear peak of events centered about $mm^2 = .88\ (GeV/c^2)^2$, which we attribute to the decays

$$\psi \rightarrow p\pi^-\bar{n}, \tag{52}$$

and

$$\psi \rightarrow \bar{p}\pi^+n. \tag{53}$$

5.3.2 Branching fraction

A phase space Monte Carlo was used to estimate our efficiencies

$$\epsilon(\psi \to p\pi^-\bar{n}) = .482, \tag{54}$$

and

$$\epsilon(\psi \to \bar{p}\pi^+n) = .467. \tag{55}$$

The lower efficiency of (53) relative to (52) is due to nuclear interactions within the material between the interaction point and drift chamber layer 6.

The mm^2 spectrum of each charge mode is then separately fit to the hypothesis of a Gaussian plus a quadratic background. For $\psi \to p\pi^-\bar{n}$, the fit (χ^2 = 28.4 / 19 degrees of freedom) gives us

$$1288 \pm 47 \text{ events}, \tag{56}$$

while for $\psi \to \bar{p}\pi^+n$, the fit (χ^2 = 18.5 / 19 degrees of freedom) gives us

$$1191 \pm 47 \text{ events}. \tag{57}$$

The relatively poor quality of the fits is indicative that the mm^2 spectrum is not exactly Gaussian. This is reproduced by the Monte Carlo simulation.

We then obtain the results

$$BR(\psi \to p\pi^-\bar{n}) = (2.02 \pm .07 \pm .16)\times10^{-3}, \tag{58}$$

and

$$BR(\psi \to \bar{p}\pi^+n) = (1.93 \pm .07 \pm .16)\times10^{-3}, \tag{59}$$

where we have estimated the systematic model dependence uncertainty to be 5%, due to the good uniformity of our acceptance over the Dalitz plot, visible in figures 28 and 29.

5.3.3 Dalitz plot

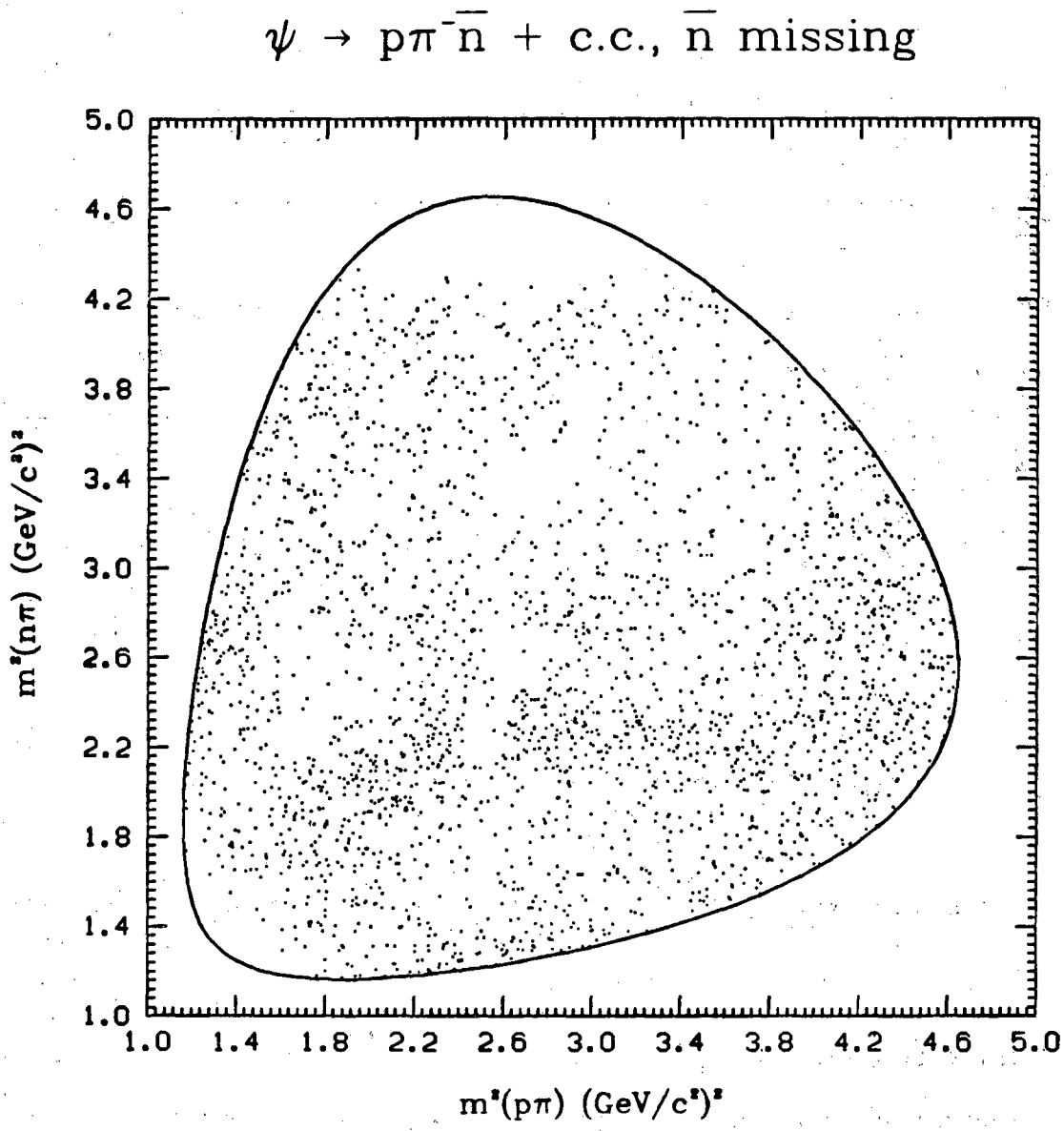

Figure 27: Dalitz plot for $\psi \to \bar{p}\pi^+ n$ + c.c..

These events are then fit to the hypotheses $\psi \to p\pi^-\bar{n}$ and $\psi \to \bar{p}\pi^+ n$ using the kinematical fitting program SQUAW. For success-

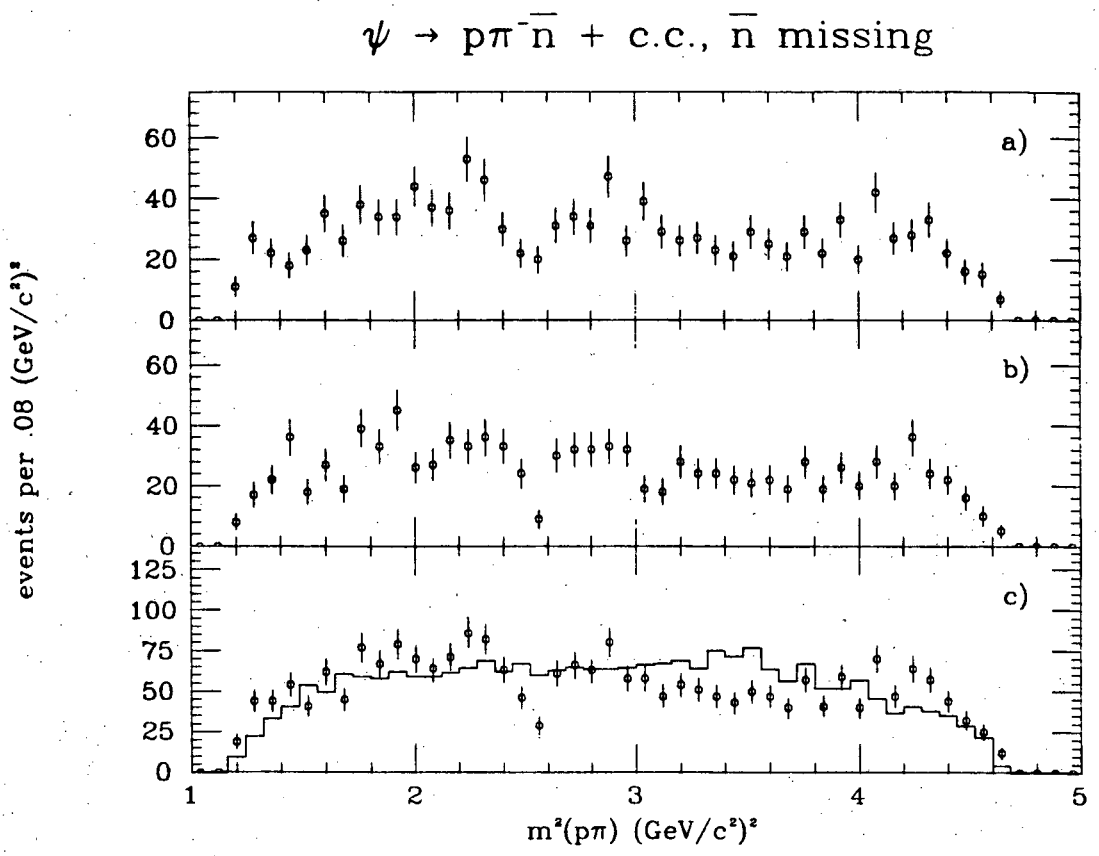

Figure 28: Dalitz projections for $\psi \to \bar{p}\pi^+ n$ + c.c..
a) $p\pi^-$ projection
b) $\bar{p}\pi^+$ projection
c) both charge modes added
Solid histogram is phase space prediction normalized to same number of events.

ful fits (event probability > .14), we then form the Dalitz plot for the events, shown in figure 27, in order to look for possible resonance structure. The Dalitz plot exhibits a number of very distinct features:

1. The depopulation at high $m^2(n\pi)$ is due to low momentum protons. As noted in figure 6, we see very few protons with momenta below about .275 GeV/c.

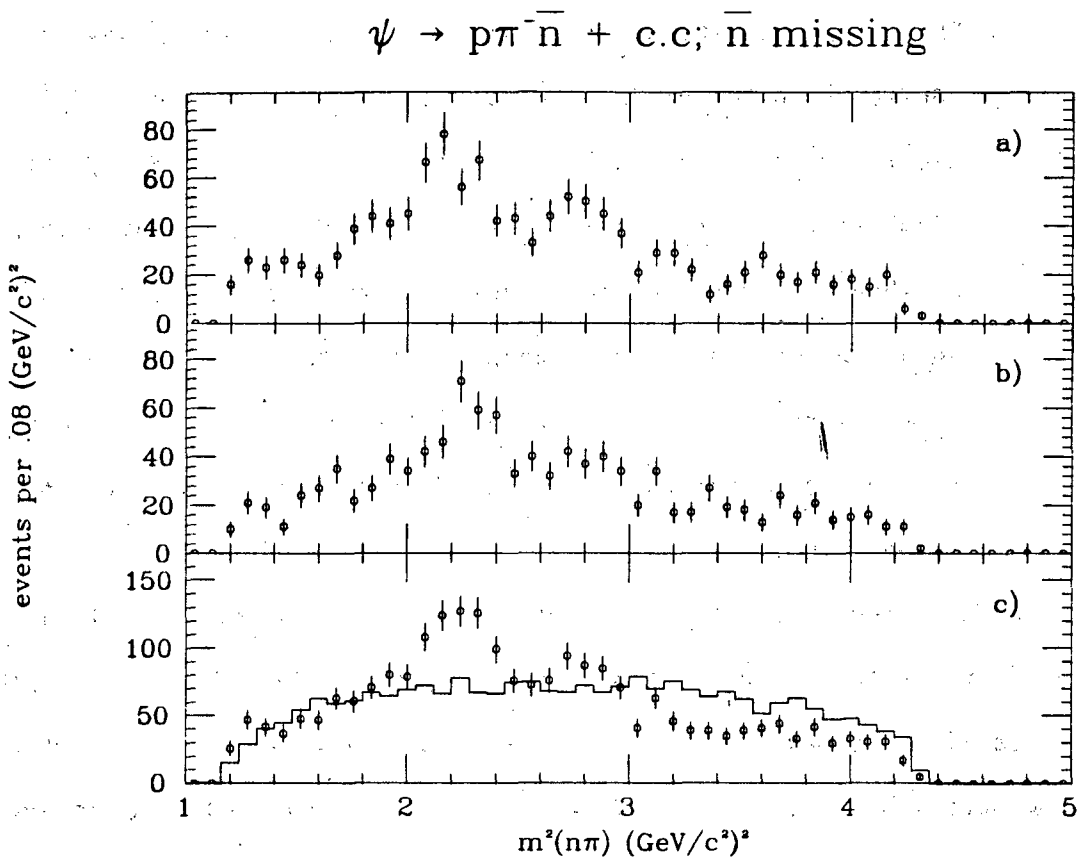

Figure 29: Dalitz projections for $\psi \rightarrow \bar{p}\pi^+ n$ + c.c..
a) $\bar{n}\pi^-$ projection
b) $n\pi^+$ projection
c) both modes added
Solid histogram is phase space prediction normalized to same number of events.

2. The depopulation at low $m^2(pn)$ is similarly due to low momentum pions. Figure 6 shows very little population below about .090 GeV/c.

3. There is clear evidence for resonance formation in the $n\pi$ system.

4. The "droop" of the resonance band in the $n\pi$ system near 2.2 $(GeV/c^2)^2$ could possibly be due to the interference of two similar ψ decay amplitudes, both of which decay to the same final state, and have the same relative phase relationship as they move through their resonances. In this case, the interference will be constructive along a line of $m^2(n\pi) = m^2(p\pi)$, and destructive otherwise. This would produce and enhancement along the diagonal of the Dalitz plot, as observed.

In an attempt to make this more quantitative, we plot the Dalitz projections for the $p\pi$ and $n\pi$ axes, in figures 28 and 29. The $p\pi$ projection is notably featureless, with the exception of a large dip near 2.55 $(GeV/c^2)^2$. This could either be a dip between two resonances or an interference affect, but these interpretations are speculative.

On the other hand, the $n\pi$ projection in figure 29 shows the aforementioned significant resonant formation. There is a clear peak centered near 2.25 $(GeV/c^2)^2$. This we tentatively[59] identify as the P'_{11} nucleon state known as N*(1470). The peak has a full width of $\simeq$ 140 MeV/c^2, certainly not inconsistent with the range of widths obtained by partial wave analysis experiments. Doing the simplest kind of analysis possible, we handfit the background and estimate that there are

$$209 \pm 31 \text{ events,} \tag{60}$$

which we attribute to the decay

$$\psi \rightarrow \bar{p}N^{*+}(1470) + \text{c.c. (charge conjugate).} \tag{61}$$

Thus,

$$BR(\psi \to \bar{p}N^{*+}(1470) + c.c.) = (.89 \pm .13 \pm .22)\times 10^{-3}, \quad (62)$$

where we have used the fact that $N^*(1470)$ decays to $N\pi \simeq 60\%$ of the time and that by a Clebsch-Gordan decomposition, 2/3 of the time the $N\pi$ state will be $n\pi^+$. We have attributed an overall 25% systematic error, due to background subtraction and resonance considerations.

There is a second, less significant enhancement in the $n\pi$ projection, centered near 2.8 $(GeV/c^2)^2$. Its width is the same, $\simeq$ 150 MeV/c^2. Again, there are three states in the vicinity of the mass peak. These are a S''_{11} state $N^*(1650)$, a D'_{15} state $N^*(1670)$, and a F'_{15} state $N^*(1688)$, all of which have large ($\simeq$ 50%) branching fractions into $N\pi$. We tentatively identify the mass peak as $N^*(1670)$, though again it could be an admixture. The results are not sensitive to this fact.

Doing a crude background subtraction, we obtain

$$85 \pm 24 \text{ events}, \quad (63)$$

which we attribute to the decay

$$\psi \to \bar{p}N^{*+}(1670) + c.c.. \quad (64)$$

Thus,

$$BR(\psi \to \bar{p}N^{*+}(1670) + c.c.) = (.43 \pm .10 \pm .11)\times 10^{-3}, \quad (65)$$

with a 25% systematic error as above.

5.4 THE DECAY $\psi \to \bar{p}p\pi^0$

5.4.1 Data reduction

Candidate events are required to have the following criteria: exactly two oppositely charged tracks in the primary vertex, both identified as protons. Events with $m(\bar{p}p) > 2.97$ GeV/c^2 are eliminated to remove events from the ψ tail. This cut should remove no real $\psi \to \bar{p}p\pi^0$ events. For all events which satisfy the above cuts, we plot the invariant mass of the pair versus the variable $U \equiv E_{miss} - p_{miss}c$ as shown in figure 22. Events with a missing π^0 or γ (not required to be detected) show up as a band roughly centered about U = 0. events.

5.4.2 Background and direct γ subtraction, Branching Fraction

To extract the number of $\psi \to \bar{p}p\pi^0$ events, we then take the U projection of figure 22, shown in figure 30. The bins around U = 0 are then fit to a Gaussian plus a quadratic background,[60] shown as the solid line of figure 30. The results of the fit (χ^2 = 19.9 / 24 degrees of freedom) give us a total of

$$901 \pm 41 \text{ events.} \qquad (66)$$

Figure 31 shows the mass spectrum of $\bar{p}p$ pairs for those events consistent with either a missing π^0 or γ. The striking feature about figure 31 is that it exhibits a clear threshold enhancement for $\bar{p}p$ mass below 2 GeV/c^2. Note that the events in figure 31 are predominantly from $\psi \to \bar{p}p\pi^0$ (50), but that this threshold enhancement also shows up in figure 25, which is known to be predomi-

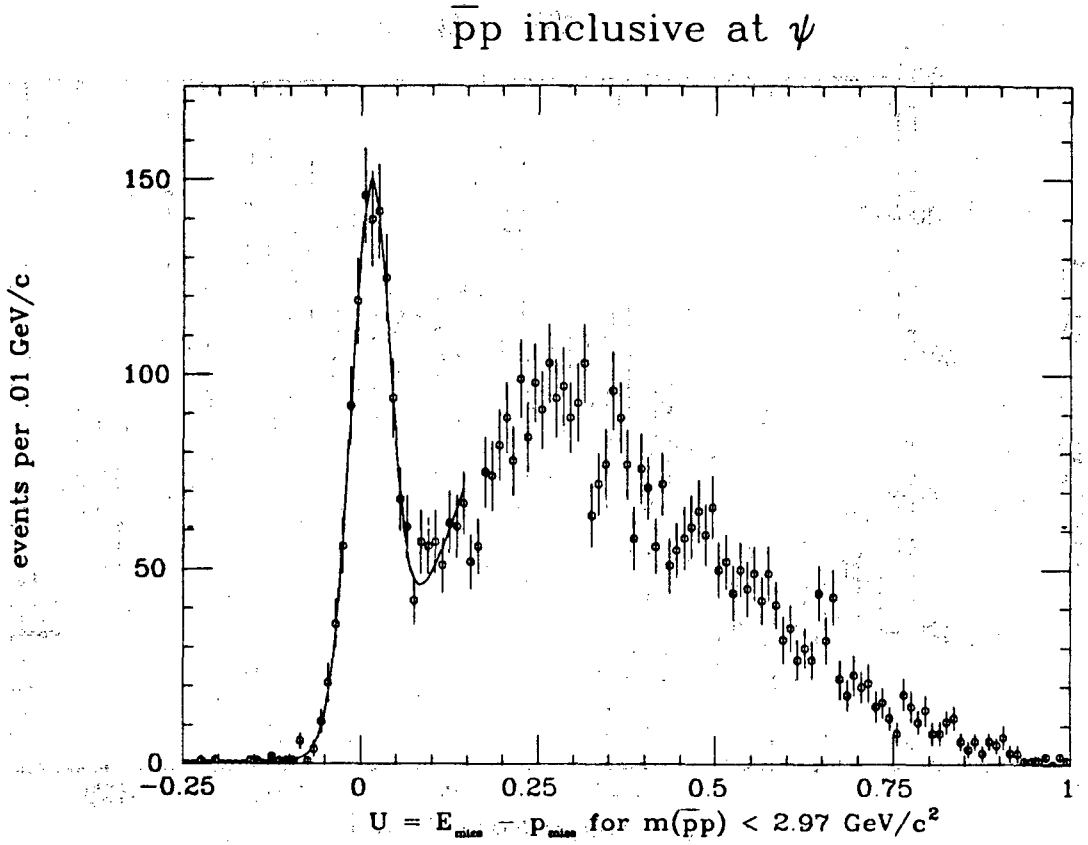

Figure 30: The quantity U for all two prong $\bar{p}p$ pairs.

nantly direct photon events. This tends to suggest that this enhancement is associated with the decay $\psi \rightarrow \bar{p}p\gamma$ (39).

There is another argument which supports the interpretation of this enhancement as associated with a photon. If it were associated with a π^0, then the isoscalar nature of the ψ demands that it be an I = 1 state. It must therefore also show up as an enhancement in the I-spin conjugate reactions $\psi \rightarrow \bar{p}\pi^+n$ (53) and $\psi \rightarrow p\pi^-\bar{n}$ (52). The Dalitz plot in figure 28 shows no such enhancement at low mass as one would expect for an I = 1 state, but at this stage it is difficult to make a conclusive assignment.

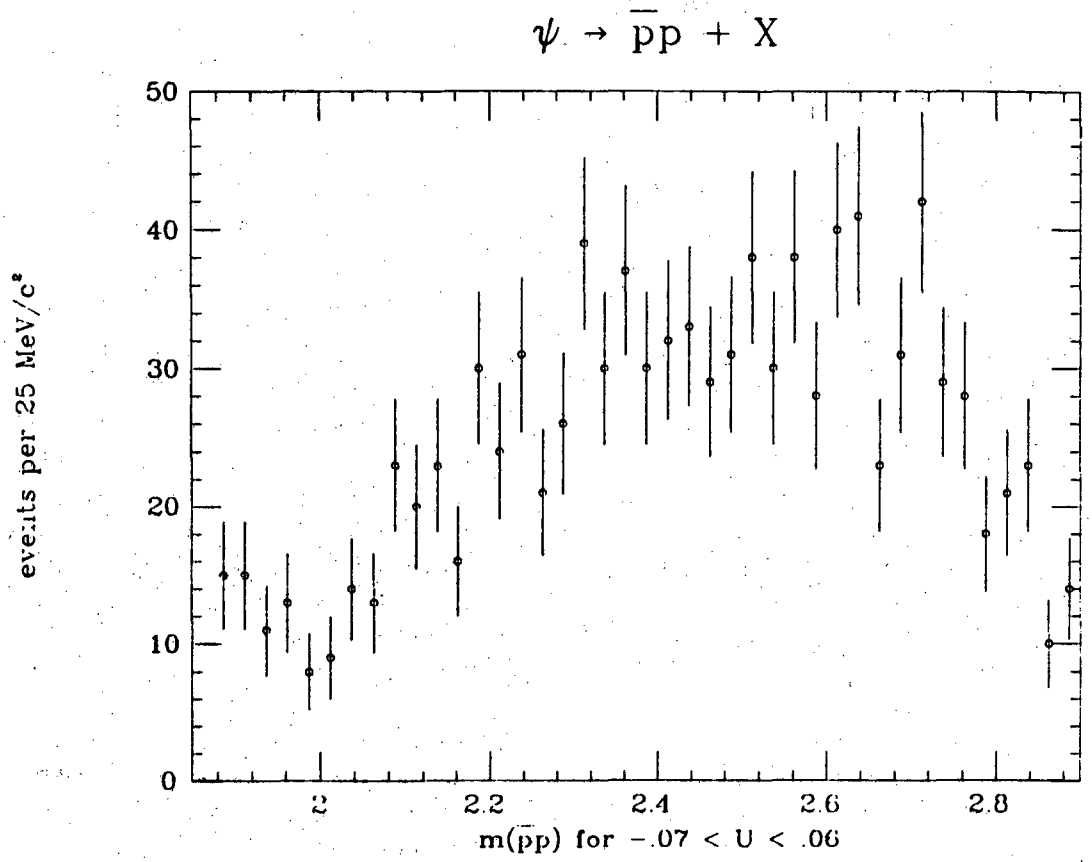

Figure 31: $\bar{p}p$ mass for events consistent with a missing $\gamma(\pi^0)$

As was mentioned in section 5.2.1, we cannot separate out events of $\psi \to \bar{p}p\gamma$ from $\psi \to \bar{p}p\pi^0$ without photon detection. As a consequence, we must remove the known contribution from $\psi \to \bar{p}p\gamma$ from this sample.

We have already determined in Section 5.2.4

$$BR(\psi \to \bar{p}p\gamma) = (.38 \pm .07 \pm .07)\times 10^{-3}, \qquad (47)$$

by observing the photon from the ψ decay. From the phase space Monte Carlo, we estimate a detection efficiency of

$$\epsilon(\psi \to \bar{p}p\gamma) = .430, \qquad (67)$$

where the photon is not required to be detected.

Consequently, we expect a feed down from $\psi \to \bar{p}p\gamma$ of

$$216 \pm 38 \text{ events,} \tag{68}$$

from which we deduce an excess of

$$685 \pm 56 \text{ events,} \tag{69}$$

which we attribute to the decay $\psi \to \bar{p}p\pi^0$.

From the phase space Monte Carlo, we estimate a detection efficiency of

$$\epsilon(\psi \to \bar{p}p\pi^0) = .458, \tag{70}$$

where the π^0 is not required to be detected. Our result is

$$BR(\psi \to \bar{p}p\pi^0) = (1.13 \pm .09 \pm .09)\times 10^{-3}, \tag{71}$$

where we have added contributions due to the direct photon branching fraction of 3.2×10^{-5} and an estimated 5% model dependent uncertainty from acceptance variations over the Dalitz plot systematically in quadrature.

5.4.3 Dalitz plot

These events are then fit to the event hypothesis $\psi \to \bar{p}p\pi^0$. For successful fits (event probability > .1), we form the Dalitz plot of the events, shown as figure 32, in order to investigate possible resonance formation. The depopulations at high $m^2(p\pi)$ are due to soft protons. Statistics are limited, but there does appear to be some evidence for an enhancement near $m^2 = 2.2\ (GeV/c^2)^2$.

In an attempt to be more quantitative, we plot the projections onto the $p\pi$ axes of the Dalitz plot in figure 33. Phase space is clearly a poor description of the background, possibly due to in

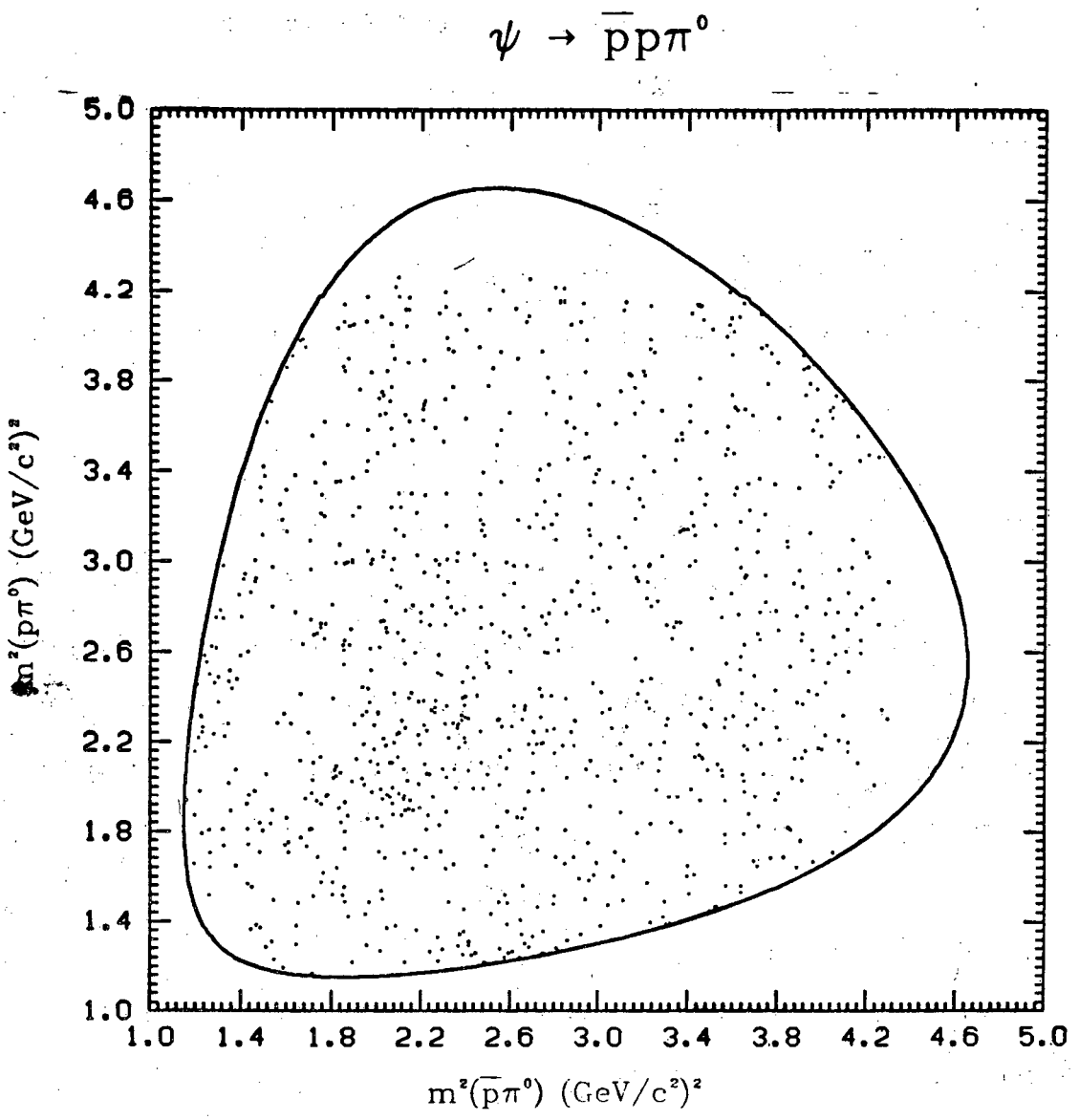

Figure 32: Dalitz plot for $\psi \to \bar{p}p\pi^0$.

part the large contamination of $\bar{p}p\gamma$ events in the sample, but there is good evidence for a resonance centered near 2.16 $(GeV/c^2)^2$. We tentatively identify this bump as the P'_{11} nucleon state N*(1470). All arguments mentioned in section 5.3.3 regarding this state in the reaction $\psi \to \bar{p}\pi^+n$ + c.c. apply here also.

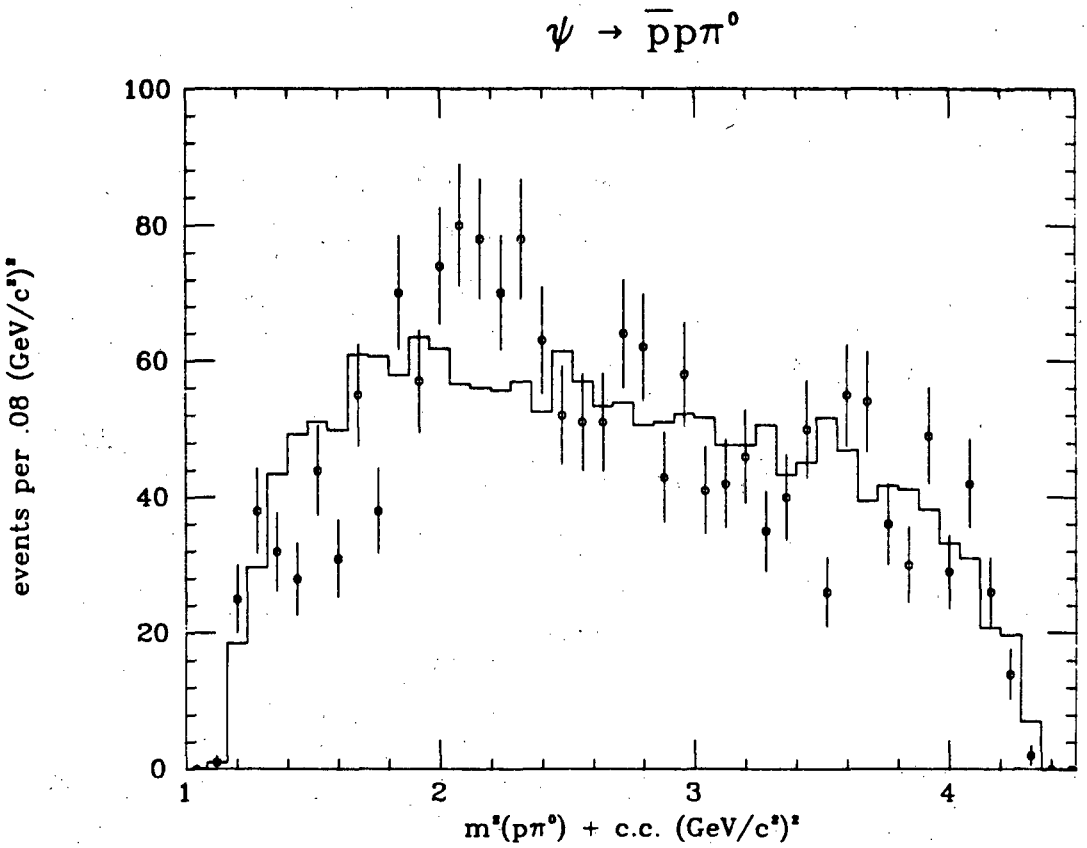

Figure 33: $p\pi^0$ + c.c. projection of $\psi \to \bar{p}p\pi^0$ Dalitz plot. Solid histogram is phase space normalized to same number of events.

Paralleling the logic of section 5.3.3, we estimate there are

$$100 \pm 25 \text{ events,} \tag{72}$$

which we attribute to the decay

$$\psi \to \bar{p}N^{*+}(1470) + \text{c.c.}. \tag{73}$$

Thus,

$$BR(\psi \to \bar{p}N^{*+}(1470) + \text{c.c.}) = (.84 \pm .21 \pm .21)\times 10^{-3}, \tag{74}$$

where we have used the fact that the $N\pi$ final state decays 1/3 of the time into $p\pi^0$, and the usual 25% systematic error.

5.5 THE DECAY $\psi \rightarrow \bar{p}p\eta$

5.5.1 Data reduction

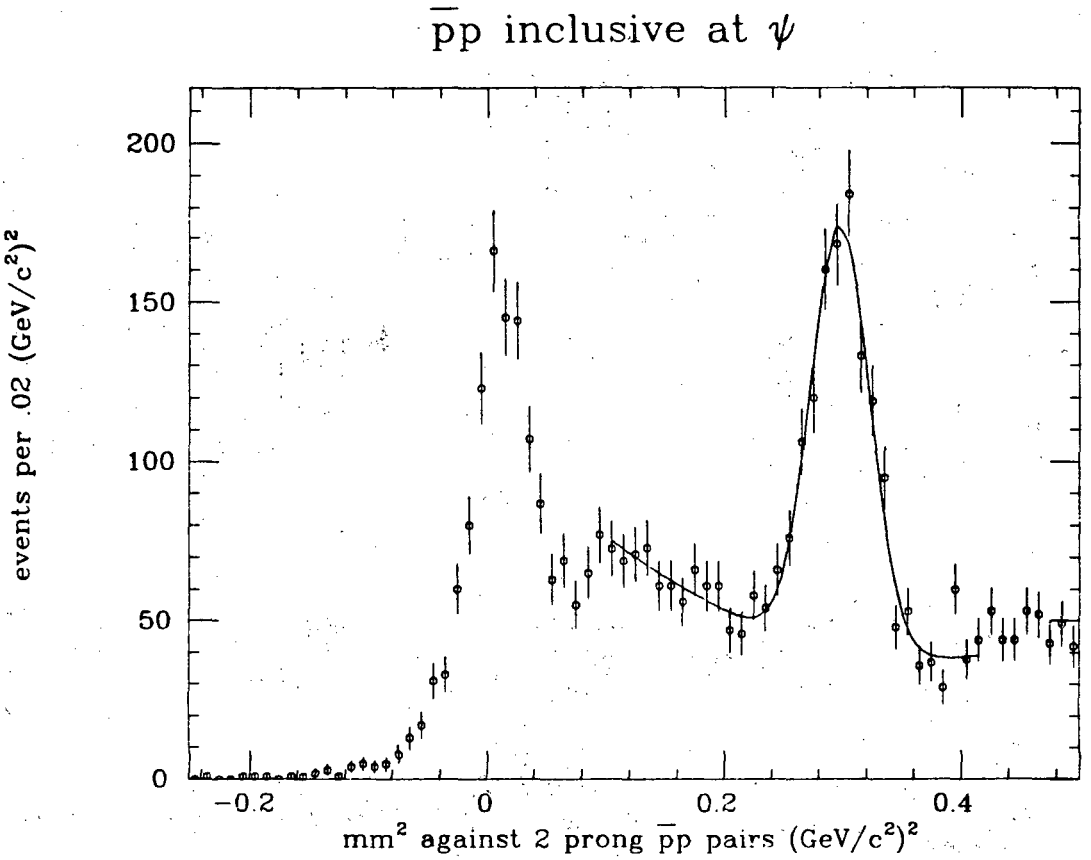

Figure 34: mm^2 against two prong $\bar{p}p$ pairs at ψ.

Candidate events are selected using the following criteria: We know that > 70% of the decays of the η involve just neutrals, consequently we may improve our signal to noise by requiring exactly two oppositely charged prongs coming from the primary vertex, both identified as protons. Unlike the π^0 case mentioned in section 5.4.1, mm^2 is a more useful variable due to the significant mass

difference between the η and the π^0. For these events, we plot the mm^2 opposite the $\bar{p}p$ pair in figure 34. There is a clear enhancement centered about $mm^2 = .3\ (GeV/c^2)^2$, which we attribute to the decay

$$\psi \rightarrow \bar{p}p\eta. \tag{75}$$

5.5.2 Branching fraction

To extract the number of $\bar{p}p\eta$ events, a fit is done to the mm^2 distribution to the hypothesis of a Gaussian plus a quadratic background. From the fit ($\chi^2 = 11.7$ / 14 DF), we obtain

$$826 \pm 52 \text{ events}, \tag{76}$$

which satisfy the event hypothesis.

A phase space Monte Carlo is used to determine our efficiency, where the η is allowed to decay to various final states according to its known branching fractions. From this, we estimate an efficiency of

$$\epsilon = .309. \tag{77}$$

This yields the result

$$BR(\psi \rightarrow \bar{p}p\eta) = (2.03 \pm .13 \pm .16)\times 10^{-3}, \tag{78}$$

which includes a 5% systematic model uncertainty due to the good uniformity of our acceptance over the Dalitz plot, visible in figure 36.

5.5.3 Dalitz plot

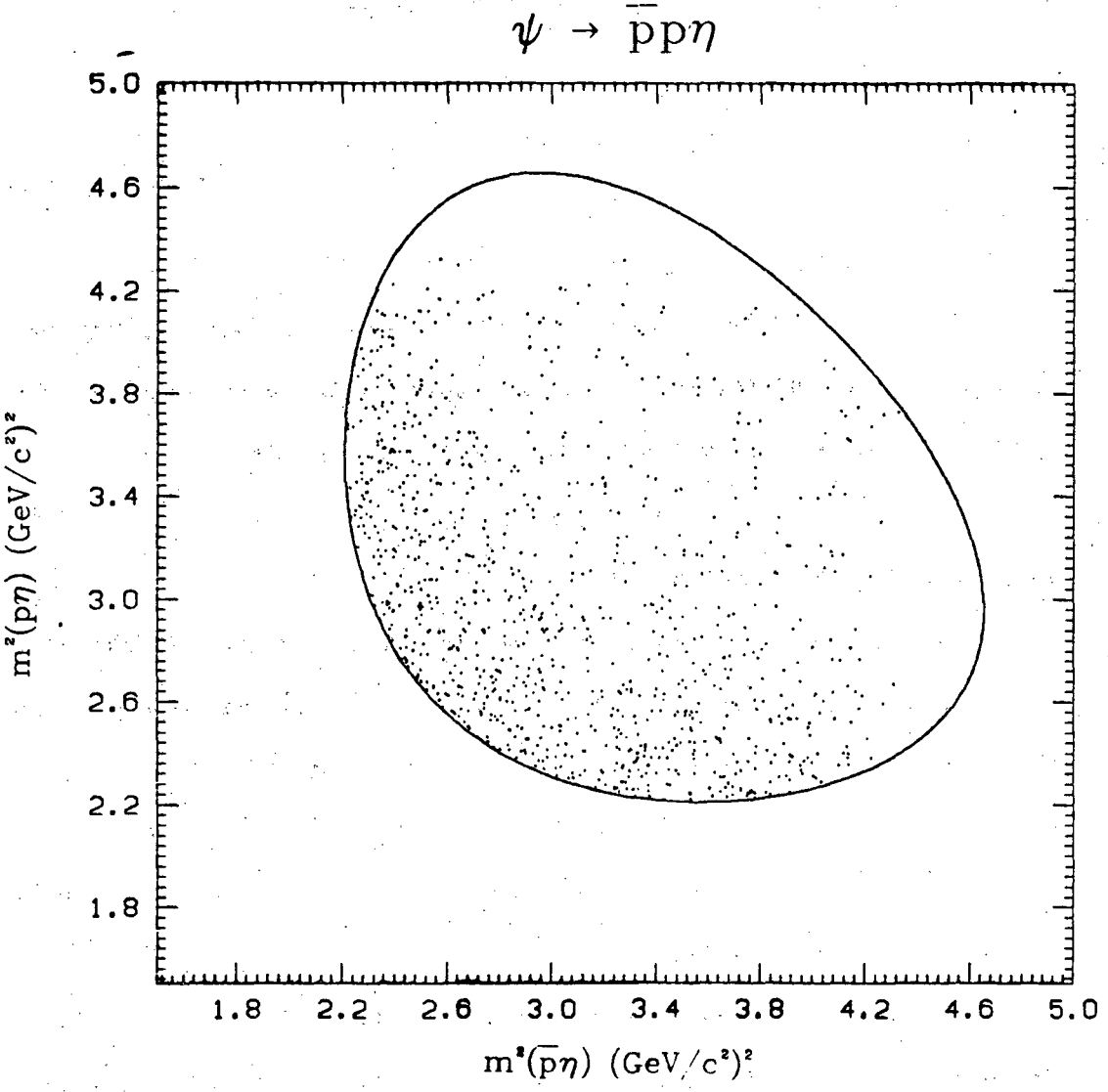

Figure 35: Dalitz plot for $\psi \to \bar{p}p\eta$.

These events are then fit (roughly 30 to 40% background) to the event hypothesis $\psi \to \bar{p}p\eta$. For the 1101 events (signal plus back-

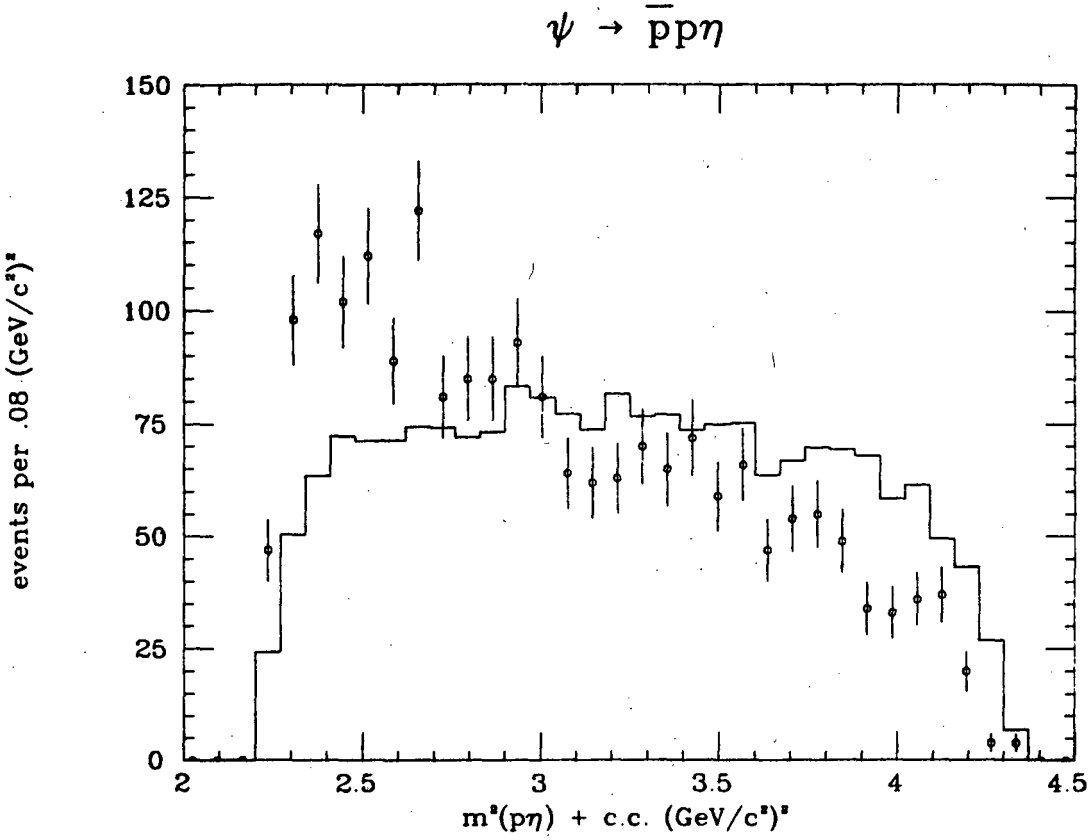

Figure 36: $p\eta$ + c.c projection of $\psi \rightarrow \bar{p}p\eta$ Dalitz plot.
Solid histogram is phase space normalized to same number of events.

ground) which have successful fits (event probability > .1), we form the Dalitz plot of the events, shown in figure 35. The depopulations at high $m^2(p\eta)$ are due to soft protons. The Dalitz plot exhibits nonuniform population, poorly described by phase space. This may be seen by plotting the $p\eta$ projections in figure 36. The projections tend to peak at $\simeq 2.52$ $(GeV/c^2)^2$, but resonant formation is not clear. There is a S'_{11} nucleon state N*(1535) with a substantial branching fraction ($\simeq$ 55%) into $N\eta$, and we may be see-

ing the influence of this resonance, but further conclusions are difficult.

5.6 THE DECAY $\psi \rightarrow \bar{p}p\omega$

5.6.1 Branching fraction

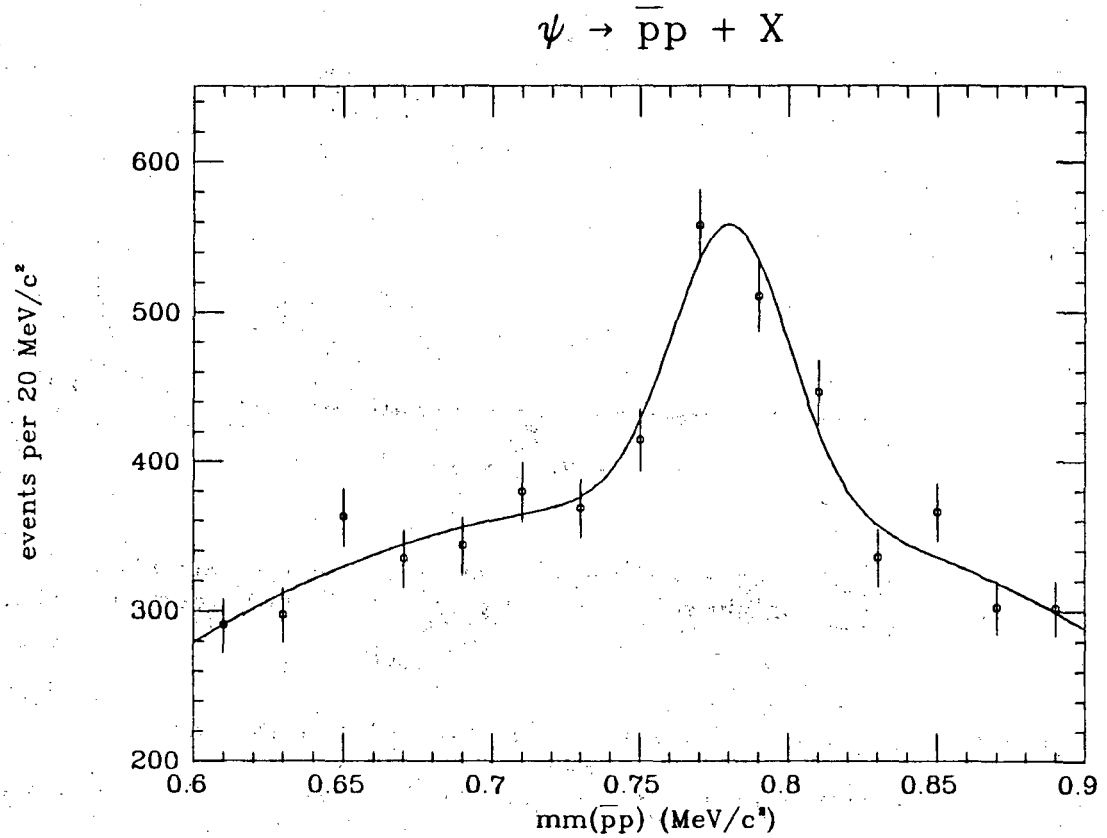

Figure 37: Missing mass against inclusive $\bar{p}p$ pairs at the ψ.

Candidate events are required to have both an identified proton and antiproton in the event. For these events, we plot the mm against the dibaryon pair, shown in figure 37. There is a clear

enhancement centered near .78 GeV/c^2, which we attribute to the decay

$$\psi \rightarrow \bar{p}p\omega. \tag{79}$$

To ascertain the number of events in the peak, we fit the missing mass spectrum to the hypothesis of a Gaussian with a quadratic background. The results of the fit (χ^2 = 13.9/9 DF) yield an excess of

$$468 \pm 73 \text{ events}, \tag{80}$$

attributable to reaction (79).

Our efficiency is determined by a phase space Monte Carlo. The ω is allowed to decay with its known branching fractions. Similarly, all the ω decay products (e.g. charged pions) are allowed to decay. Final state particle correlations, however, between the ω decay products are ignored. From this, we estimate an efficiency

$$\epsilon = .323, \tag{81}$$

for the decay (79). Combining (80) and (81), we obtain

$$BR(\psi \rightarrow \bar{p}p\omega) = (1.10 \pm .17 \pm .18)\times 10^{-3}, \tag{82}$$

which includes a 15% model uncertainty from resonant considerations.

5.7 THE DECAY $\psi \rightarrow \bar{p}p\eta'$

5.7.1 Data Reduction

The η' has two principal decay modes:

1. 65.6% of the time the η' decays in to $\eta\pi\pi$, and
2. 29.8% of the time the η' decays into $\rho^0\gamma$.

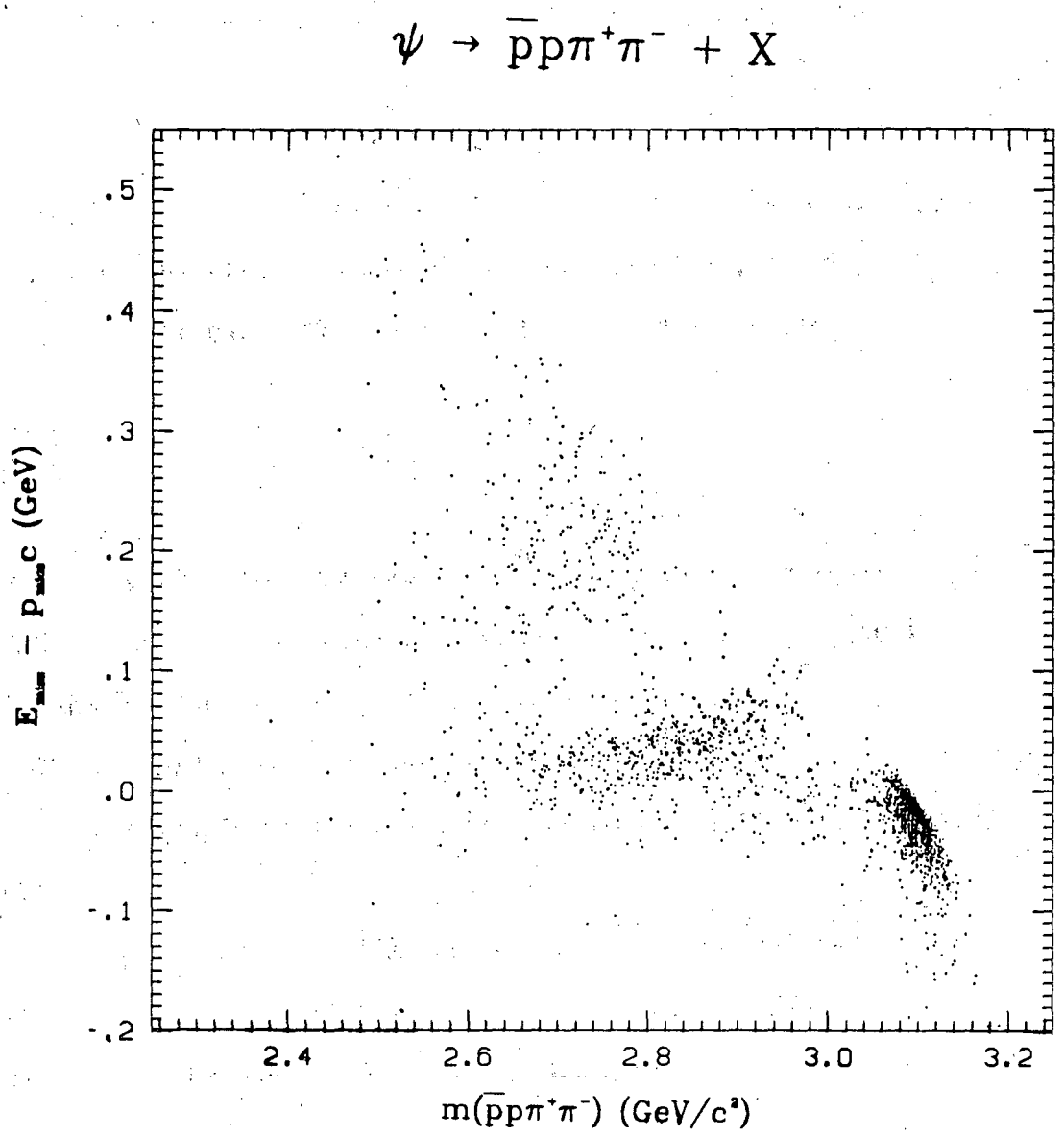

Figure 38: Scatterplot of the quantity U vs. $m(\bar{p}p\pi^+\pi^-)$.

One might hope to reconstruct the η' decay by observing both pions from the η' decay opposite the η as well as both protons, but this fails for the following reasons:

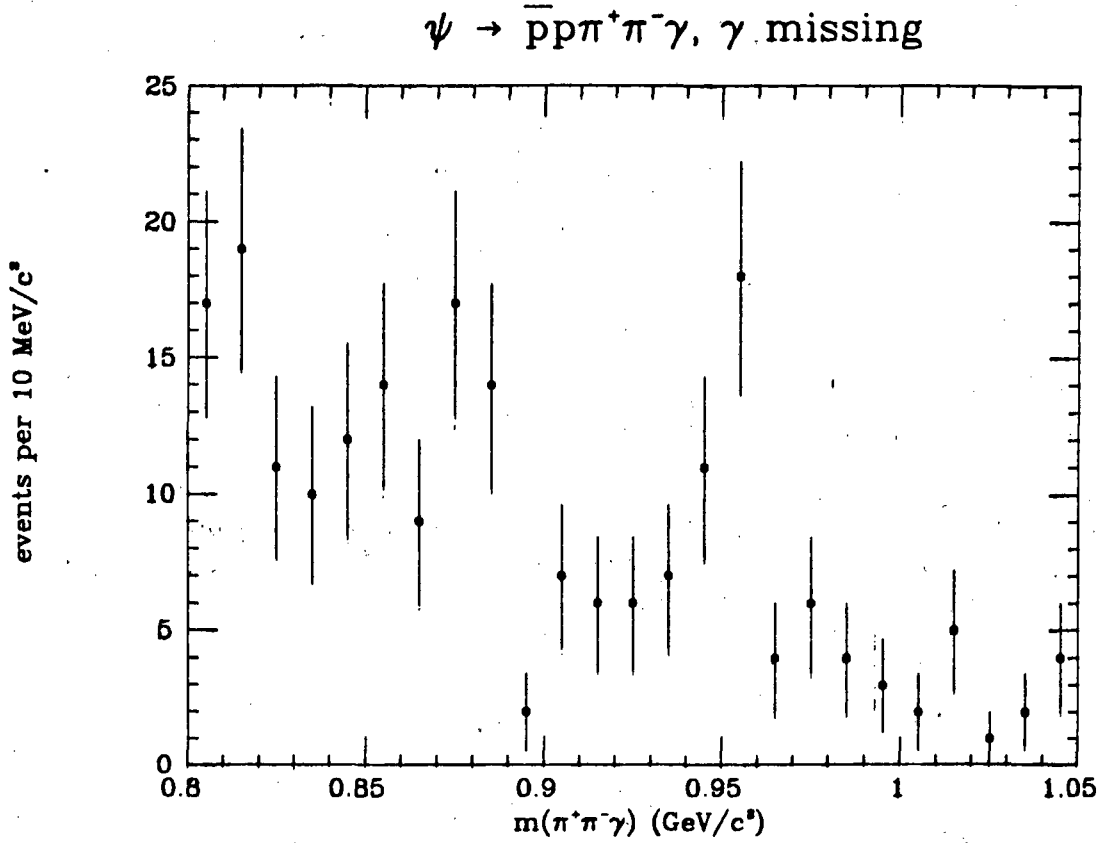

Figure 39: $\pi^+\pi^-\gamma$ mass in $\psi \rightarrow \bar{p}p\pi^+\pi^-\gamma$ events.

1. The η' decay into $\eta\pi\pi$ has a very small Q value. The maximum momentum either pion may have in the η' center of momentum frame is 231 MeV/c. The average momentum will be substantially less. Consequently, there will be very few times when the η' decays so that both of the pions are detectable.
2. We also lose via isospin arguments. Both the η and the η' are isoscalar particles. It immediately follows that the two pion system must be in an I = 0 state. Doing a simple Clebsch-Gordan decomposition, it follows that the two pions

are charged in only two thirds of the η' decays. We of course have a reasonable detection efficiency only for the charged pion decays.

It is then clear that we must detect the η' via its $\rho^0\gamma$ decay mode. We lose in the branching fraction of the η' to $\rho^0\gamma$, but we gain since the ρ^0 decays essentially 100% of the time into $\pi^+\pi^-$.[61] We could never hope to observe the soft photon from the η' decay as the maximum momentum available to the photon in the η' center of mass is only 164 MeV/c.

Candidate events are required to have exactly four charged tracks in the primary vertex, two oppositely charged tracks identified as protons, the other oppositely charged pair consistent with being pions. For these events, we plot the quantity U (see section 5.2.1) vs. the mass of the $\bar{p}p\pi^+\pi^-$ system, shown in figure 38. There is a clear band of events centered near U = 0, which are consistent with the decays

$$\psi \rightarrow \bar{p}p\pi^+\pi^-\gamma, \tag{83}$$

and

$$\psi \rightarrow \bar{p}p\pi^+\pi^-\pi^0 \tag{84}$$

As mentioned in section 5.2.1, we cannot distinguish between (83) and (84) without photon detection. We therefore hope to constrain the events and possibly see a signal above the π^0 background. For events which fall in this band, we perform a 1C fit to the event hypothesis (83). for events which pass this fit (event probability > .15), we plot the $\pi^+\pi^-\gamma$ mass, shown in figure (83).

There is a small but narrow enhancement centered at $\simeq .95$ GeV/c^2, which we attribute to the decay

$$\psi \to \bar{p}p\eta'. \tag{85}$$

Our task is now to determine the branching fraction. Fitting the peak is futile as there are but two bins in the peak and three independent parameters in a Gaussian peak. Statistics prohibit finer binning of the data. Consequently, we trust our eyesight and simply do an handfit subtraction of the background. Taking as the signal region the two high bins centered at .945 and .955, where there are a total (signal plus background) of

$$29 \pm 3 \text{ events.} \tag{86}$$

The results of our handfit background yield

$$10 \pm 3 \text{ events.} \tag{87}$$

Combining (86) and (87), we obtain a total of

$$19 \pm 6 \text{ events,} \tag{88}$$

which we attribute to the decay (85). The significance of this peak may be ascertained by calculating the Poisson probability that one gets 29 events when one expects 10:

$$P_{10}(29) = 5.1\times10^{-7}. \tag{89}$$

From (89), it is clear this bump is not a fluctuation.

In order to determine our efficiency, events of the topology (85) are generated according to a phase space distribution. The η' is allowed to decay according to its known branching fractions, as are its decay products. Correlations between the final state particles (e.g. the $\pi^+\pi^-$ in the ρ^0 decay) are ignored. From this, we estimate an efficiency of

$$\epsilon = .021. \tag{90}$$

Combining (88) and (90), we find

$$BR(\psi \to \bar{p}p\eta') = (.68 \pm .23 \pm .17)\times 10^{-3}, \tag{91}$$

where we attributed an overall 25% systematic error due to model dependent uncertainty and background subtraction.

5.8 THE DECAY $\psi \to \bar{p}p\pi^+\pi^-$

5.8.1 Data reduction

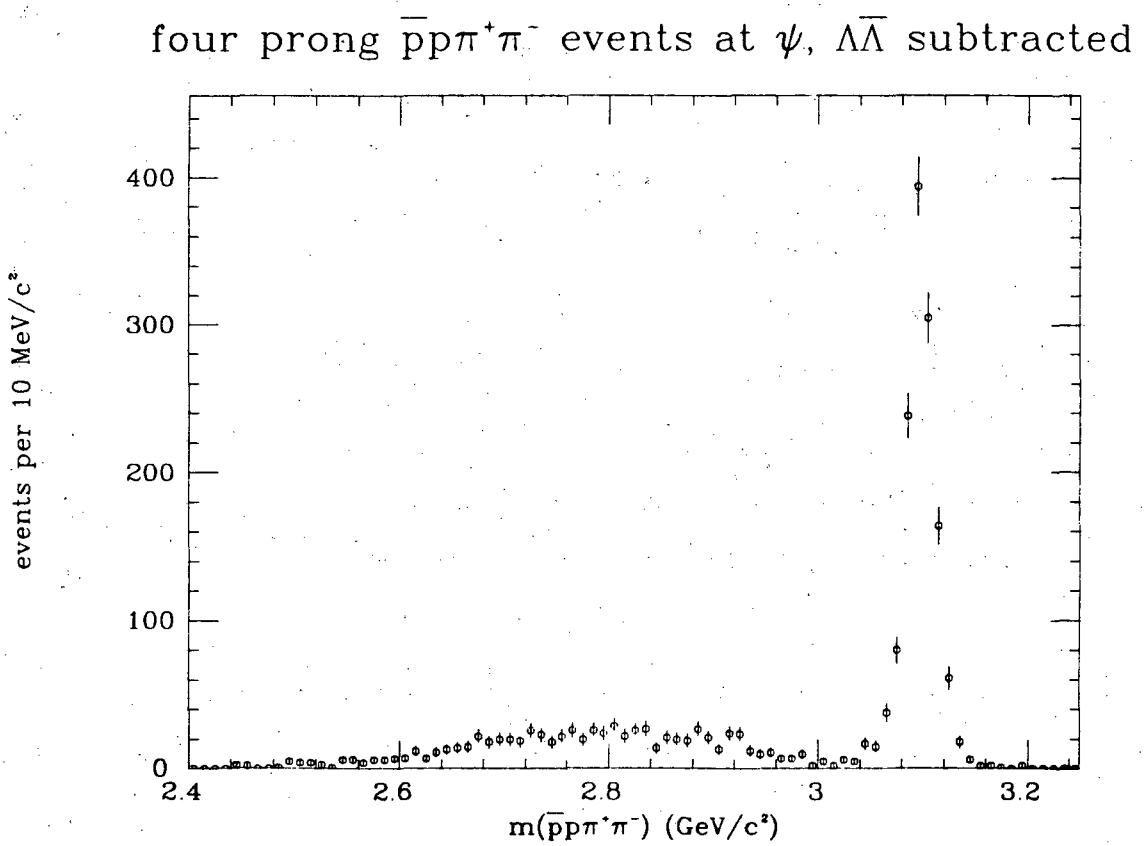

Figure 40: Mass plot for 4 prong $\bar{p}p\pi^+\pi^-$ events.

Candidate events are required to have exactly 4 prongs eminating from the primary vertex, where the total vertex charge is zero. There must be one each of a proton, antiproton, π^+, and π^-. Even with the vertex constraint, there is still a substantial contamination from the decay $\psi \to \Lambda\bar{\Lambda}$, where neither Λ traveled far enough before decaying to be tracked to a secondary vertex. We remove these events by requiring that all further events lie outside a circle of radius 10 MeV/c^2 about the nominal $\Lambda\bar{\Lambda}$ point in the Goldhaber plot (see section 5.8.3). For these events, we then plot the mass of the $\bar{p}p\pi^+\pi^-$ system, as shown in figure 40. There is a clear excess of events centered at the center of mass energy, which we attribute to the decay

$$\psi \to \bar{p}p\pi^+\pi^-. \tag{92}$$

We further require that $3.05 < m(\bar{p}p\pi^+\pi^-) < 3.14$ GeV/c^2, so that events are well within the mass peak.

5.8.2 Branching fraction

In the signal region, we have

$$1435 \pm 38 \text{ events.} \tag{93}$$

From the phase space Monte Carlo, we estimate an efficiency of

$$\epsilon = .168. \tag{94}$$

Combining (93) and (94), we get

$$BR(\psi \to \bar{p}p\pi^+\pi^-) = (6.46 \pm .17 \pm .43)\times 10^{-3}, \tag{95}$$

which incudes a 5% model dependent systematic uncertainty from resonance and acceptance considerations.

5.8.3 Goldhaber plots

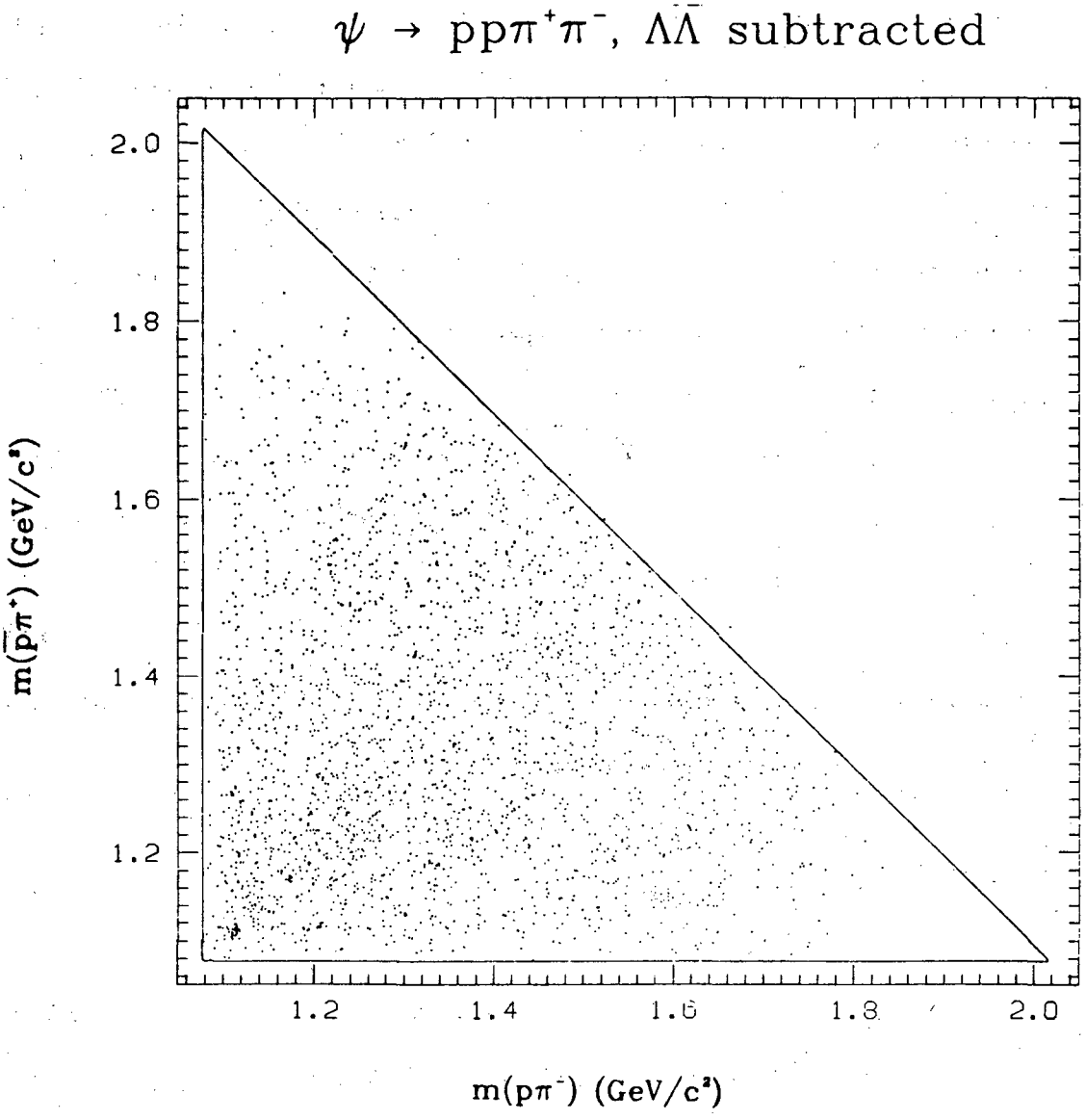

Figure 41: Goldhaber plot of $m(p\pi^-)$ vs. $m(\bar{p}\pi^+)$.

In order to investigate possible resonance formation in this final state, we form the Goldhaber, or triangle plot, of the decay

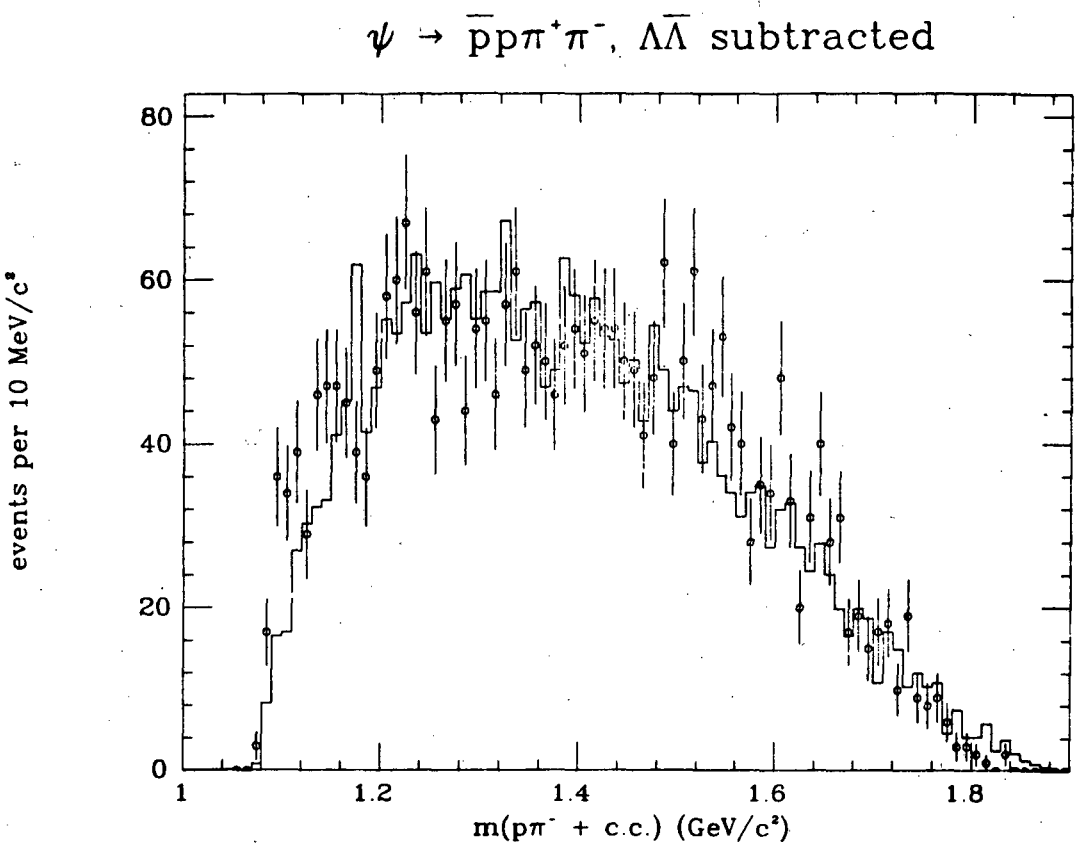

Figure 42: m(pπ⁻ + c.c.) in $\psi \rightarrow \bar{p}p\pi^+\pi^-$ events. Solid line is phase space Monte Carlo prediction, normalized to same number of events.

products. Due to our good momentum resolution for charged tracks, we do not gain much information from constraining the events. Hence, these are unconstrained Goldhaber plots.

Figure 41 shows the Goldhaber plot for neutral pπ pairs. No resonance behavior is observed, with the exception of a small residual $\Lambda\bar{\Lambda}$ contamination, visible in the lower left hand corner. We compare this channel directly with the Monte Carlo by plotting the summed projections for the neutral pπ combinations, as shown in

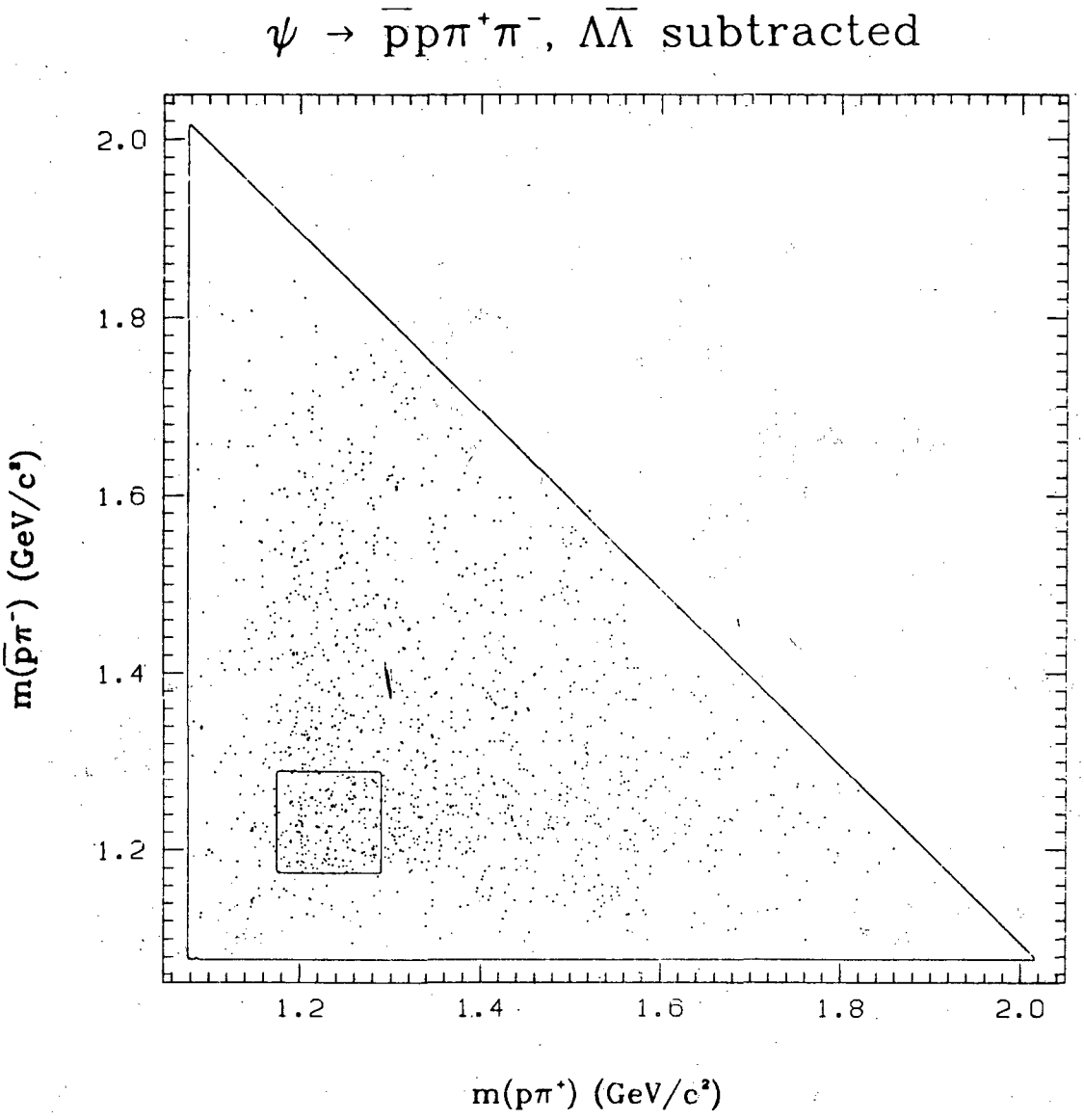

Figure 43: Goldhaber plot of $m(p\pi^+)$ vs. $m(\bar{p}\pi^-)$. Box is $\Delta^{++}\bar{\Delta}^{--}$ signal region.

figure 42. Each event enters twice into the plot. The Monte Carlo is seen to be in superb agreement with the data.

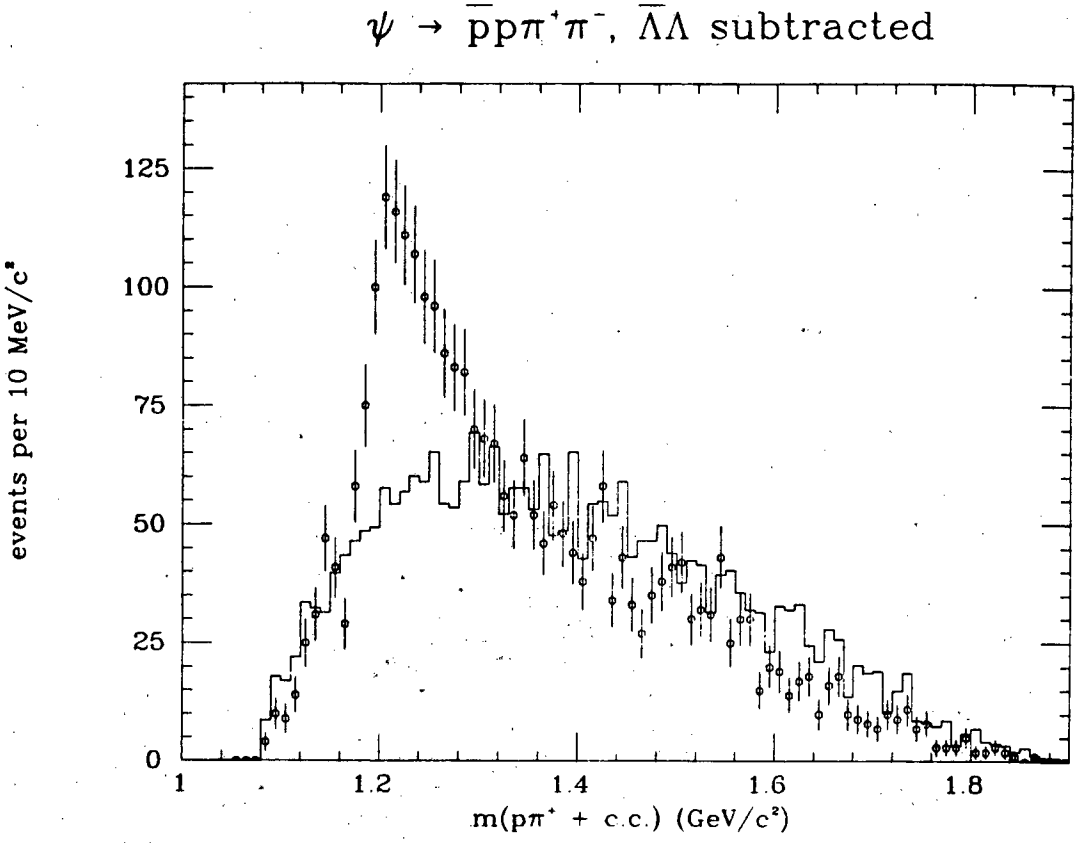

Figure 44: $m(p\pi^+ + c.c.)$ for $\psi \rightarrow \bar{p}p\pi^+\pi^-$ events. Solid histogram is phase space distribution normalized to same number of events.

At this point, we might be tempted to drop this analysis, confident that the phase space Monte Carlo is an accurate description of the reaction. This would be a mistake, as shown in figure 43. The Goldhaber plot for doubly charged pπ combinations exhibits strong enhancements centered near 1.2 GeV/c². This is readily interpreted as the P'_{33} state, the Δ^{++}. In an attempt to be more quantitative, we plot the summed doubly charged mass projections, shown in figure 44. The distinctive line shape characteristic of the Δ^{++} is

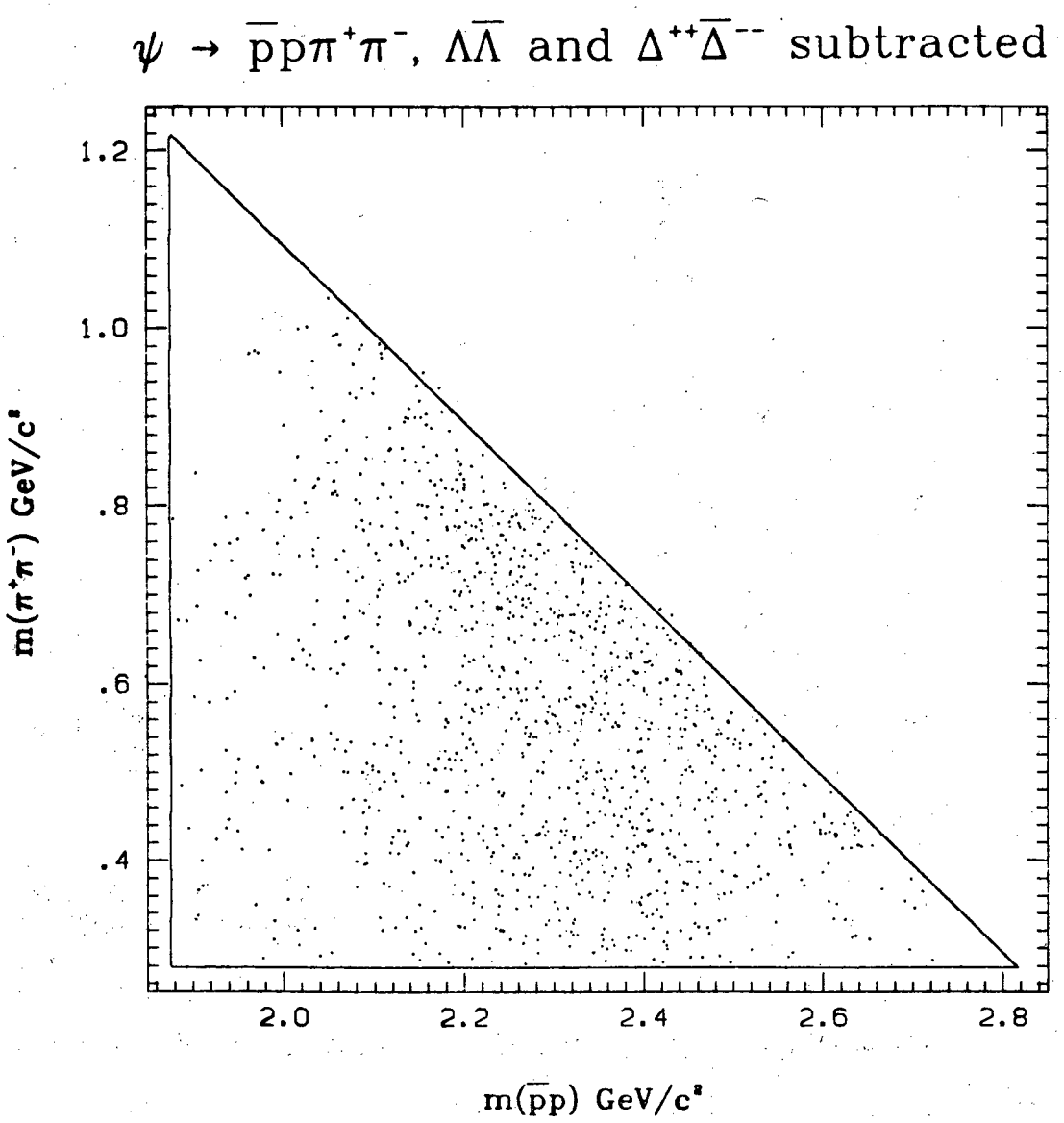

Figure 45: Goldhaber plot of $m(\bar{p}p)$ vs. $m(\pi^+\pi^-)$. $\Lambda\bar{\Lambda}$ and $\Delta^{++}\bar{\Delta}^{--}$ subtracted.

clearly visible. The solid histogram is the Monte Carlo normalized to the same number of events as the data. Taking the signal region as $1.18 < m(p\pi) < 1.32$, there is a total of

$$1278 \pm 36 \text{ pairs,} \qquad (96)$$

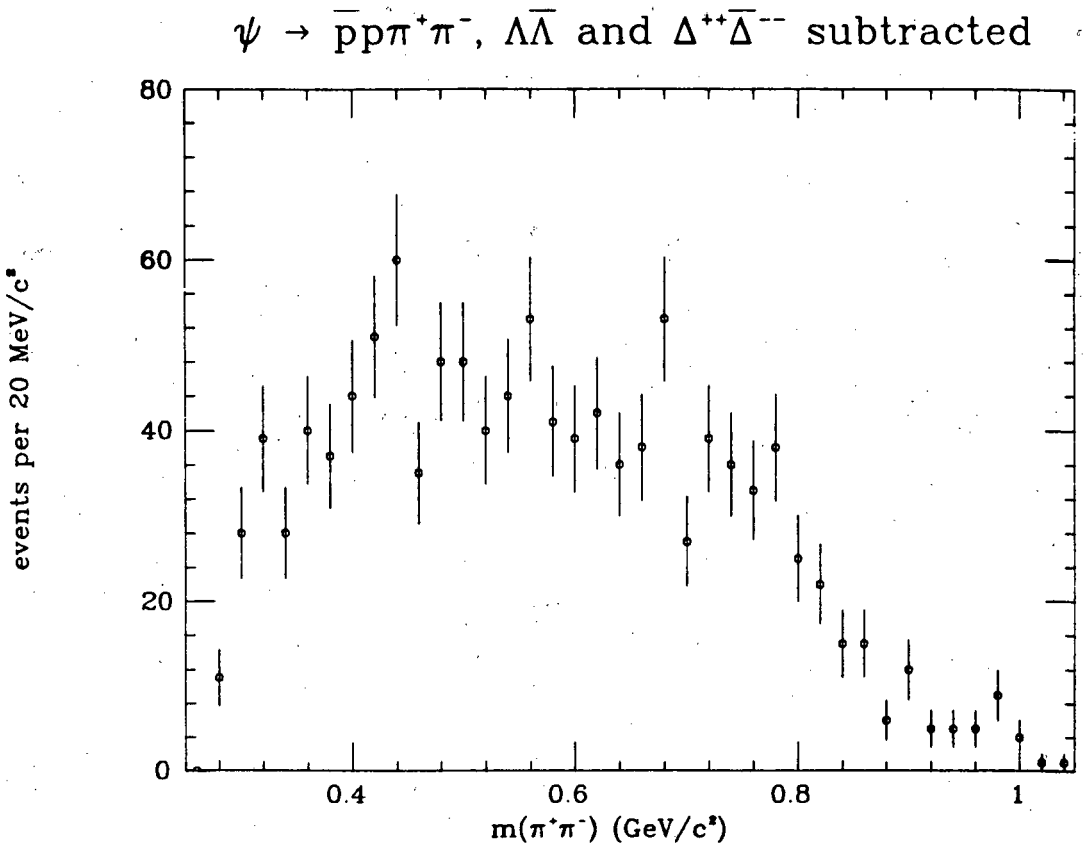

Figure 46: $m(\pi^+\pi^-)$ in $\psi \to \bar{p}p\pi^+\pi^-$ events. $\Lambda\bar{\Lambda}$ and $\Delta^{++}\bar{\Delta}^{--}$ subtracted.

which we attribute to Δ^{++} production. Of course, events from the decay

$$\psi \to \Delta^{++}\ \bar{\Delta}^{--}$$
$$\quad\ \ \hookrightarrow p\pi^+\ \hookrightarrow \bar{p}\pi^-, \tag{97}$$

will be counted twice in this plot. We define a background region as $m(p\pi) > 1.4$ GeV/c², and renormalize the Monte Carlo to the same number of data events in this region. We then estimate a background of

$$600 \pm 14 \text{ pairs}, \tag{98}$$

whence the number of pairs originating from Δ^{++} decays is

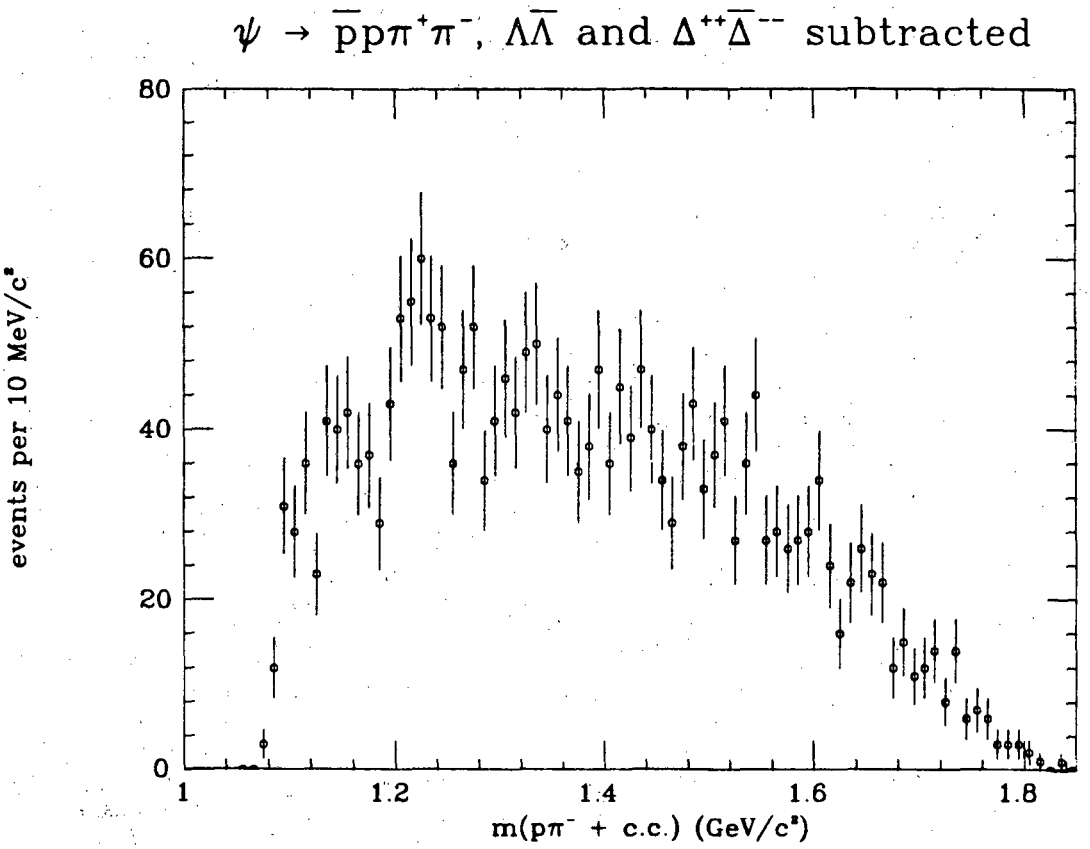

Figure 47: $m(p\pi^-)$, $\Lambda\bar{\Lambda}$ and $\Delta^{++}\bar{\Delta}^{--}$ subtracted.

$$678 \pm 39 \text{ pairs.} \tag{99}$$

Thus, we may quote the fraction of times f a doubly charged $p\pi$ pair will be in a Δ^{++} as

$$f(p\pi^+ + \text{c.c. as } \Delta^{++}) = .195 \pm .030 \pm .049, \tag{100}$$

which includes a 25% systematic error.

The problem now becomes how to determine the number of events due to reaction (97). Returning to figure 43, we define the $\Delta^{++}\bar{\Delta}^{--}$ signal region as the square bounded by $1.18 < m(p\pi) < 1.32$ GeV/c^2. In this region, there are

$$100 \pm 10 \text{ events.} \tag{101}$$

We then scale this number by the relative populations from the phase space Monte Carlo. This takes into account not only the non-uniform phase space inherent in the Goldhaber plot, but also acceptance variations over the plot. Consequently, the expected background in the signal region is

$$49 \pm 9 \text{ events.} \tag{102}$$

Thus, we are left with

$$233 \pm 19 \text{ events,} \tag{103}$$

which we attribute to the decay (97). Using (94), we may easily calculate a branching ratio, as the Δ^{++} decays 100% of the time to $p\pi^+$. Thus,

$$BR(\psi \to \Delta^{++}\bar{\Delta}^{--}) = (1.05 \pm .09 \pm .26)\times 10^{-3}. \tag{104}$$

From (99) and (103), it is clear that reaction (97) accounts for much of the Δ^{++} production. There is however some residual production. We may ascertain this fraction by taking bands bounded by $1.18 < m(p\pi) < 1.32$ GeV/c^2 and excluding the $\Delta^{++}\bar{\Delta}^{--}$ region as previously defined. We find

$$700 \pm 26 \text{ events,} \tag{105}$$

whereas the Monte Carlo would predict

$$368 \pm 42 \text{ events.} \tag{106}$$

Thus, there appears to be an excess of

$$332 \pm 49 \text{ events,} \tag{107}$$

which we attribute to the decay

$$\psi \to \underset{\hookrightarrow p\pi^+}{\Delta^{++}}\bar{p}\pi^- + \text{c.c.}. \tag{108}$$

Thus,

$$BR(\psi \to \Delta^{++}\bar{p}\pi^- + \text{c.c.}) = (1.40 \pm .19 \pm .35)\times 10^{-3}. \tag{109}$$

We now explicitly remove the $\Delta^{++}\bar{\Delta}^{--}$ region from further analysis. Figure 45 shows the Goldhaber plot for the $\bar{p}p$ system relative to the $\pi^+\pi^-$ system. No compelling evidence for any resonance formation is seen. In particular, we plot the $\pi^+\pi^-$ projection, shown in figure 46, looking for the decay

$$\psi \rightarrow \bar{p}p\rho. \tag{110}$$

No signal is seen. If we make the unlikely assumption that the small excess of

$$38 \pm 16 \text{ events}, \tag{111}$$

in the region $.71 < m(\pi^+\pi^-) < .79$ GeV/c^2 is due to (110), then we may place a limit of

$$BR(\psi \rightarrow \bar{p}p\rho) < .31\times10^{-3}, \tag{112}$$

at the 90% confidence level.

We now return our attention to the neutral $p\pi$ system. Shown in figure 47, we plot the invariant mass of the neutral $p\pi$ combinations, after subtracting out the $\Lambda\bar{\Lambda}$ and $\Delta^{++}\bar{\Delta}^{--}$ regions. There is a slight excess of

$$78 \pm 22 \text{ events}, \tag{113}$$

centered near 1.22 GeV/c^2, which we attribute to the neutral P'_{33} counterpart of the Δ^{++}, the Δ^0. Correcting for the $\Delta^{++}\bar{\Delta}^{--}$ region subtracted out which reflects into the neutral $p\pi$ signal region, we can quote the fraction of the time f that the neutral $p\pi$ system is in a Δ^0

$$f(p\pi^- + \text{c.c. as } \Delta^0) = .029 \pm .008 \pm .007 \tag{114}$$

Further analysis is difficult.

5.9 THE DECAY $\psi \rightarrow \bar{p}p\pi^+\pi^-\gamma$

5.9.1 Data reduction

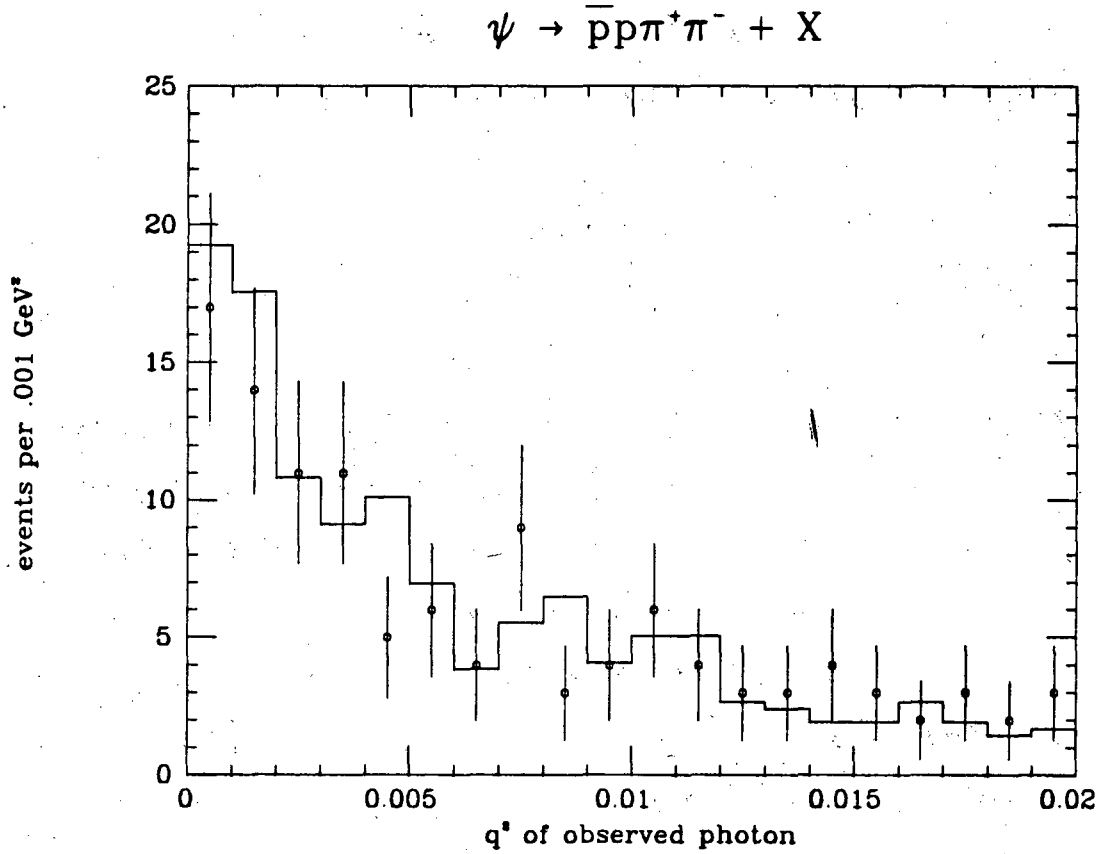

Figure 48: q^2 of observed photon.

The next logical place to look for direct photon decays of the ψ is in the four prong exclusive channel with two pions opposite the dibaryon system. The selection criteria for this channel are completely analogous to that for the decay

$$\psi \rightarrow \bar{p}p\gamma, \tag{39}$$

presented in section 5.2.1, with the obvious modification that we require four charged tracks; one oppositely charged pair identified as protons; the other pair consistent with pions.

For these events, we plot the quantity U (defined in section 5.2.1) vs. the mass of the $\bar{p}p\pi^+\pi^-$ system, shown in figure 38. There is a clear band of events centered near U = 0, which is consistent with the decays

$$\psi \rightarrow \bar{p}p\pi^+\pi^-\gamma, \tag{83}$$

and

$$\psi \rightarrow \bar{p}p\pi^+\pi^-\pi^0. \tag{84}$$

At this point, we attempt to distinguish between reactions (83) and (84) by use of the LA system. Again, this analysis is completely analogous to that presented in section 5.2.1. Figure 48 show the q^2 of the observed photon relative to the missing momentum of the $\bar{p}p\pi^+\pi^-$ system. Events with $m(\bar{p}p\pi^+\pi^-) > 2.99$ GeV/c^2 have been eliminated to remove 4C events coupling with noise photons to fake direct photon events. The q^2 distribution due to a missing photon is much more highly peaked at low q^2 ($\simeq$ 90% of the events have $q^2 < 2\times10^{-3}$ GeV^2), whereas the q^2 distribution due to a missing π^0, shown as a solid histogram in figure 48, is much broader. There is no evidence for a direct photon opposite the $\bar{p}p\pi^+\pi^-$ system.

5.9.2 Branching fraction

We may place a limit on reaction (83) from figure 48. From the statistics, we attribute

$$< 12 \text{ events (90\% confidence level)}, \tag{115}$$

to the direct photon decay, where we have taken the first data bin ($q^2 < 1\times10^{-3}$) as the signal region. From the phase space Monte Carlo, we estimate an efficiency

$$\epsilon = .023, \tag{116}$$

where we have included the module 8 correction (see section 5.2.4). Thus,

$$BR(\psi \rightarrow \bar{p}p\pi^+\pi^-\gamma) < .79\times10^{-3}, \tag{117}$$

at the 90% confidence level.

5.10 THE DECAY $\psi \rightarrow \bar{p}p\pi^+\pi^-\pi^0$

5.10.1 Data reduction

We proceed in a manner analogous to section 5.4.1, except with the obvious modification that we require four charged prongs in the primary vertex; one charged zero pair identified as protons, and the other pair consistent with pions. For these events, we plot the quantity U, defined in section 5.2.1, versus the mass of the $\bar{p}p\pi^+\pi^-$ system, shown in figure 38. There is a clear band near U = 0, which is consistent with the decays

$$\psi \rightarrow \bar{p}p\pi^+\pi^-\gamma, \tag{83}$$

and

$$\psi \rightarrow \bar{p}p\pi^+\pi^-\pi^0. \tag{84}$$

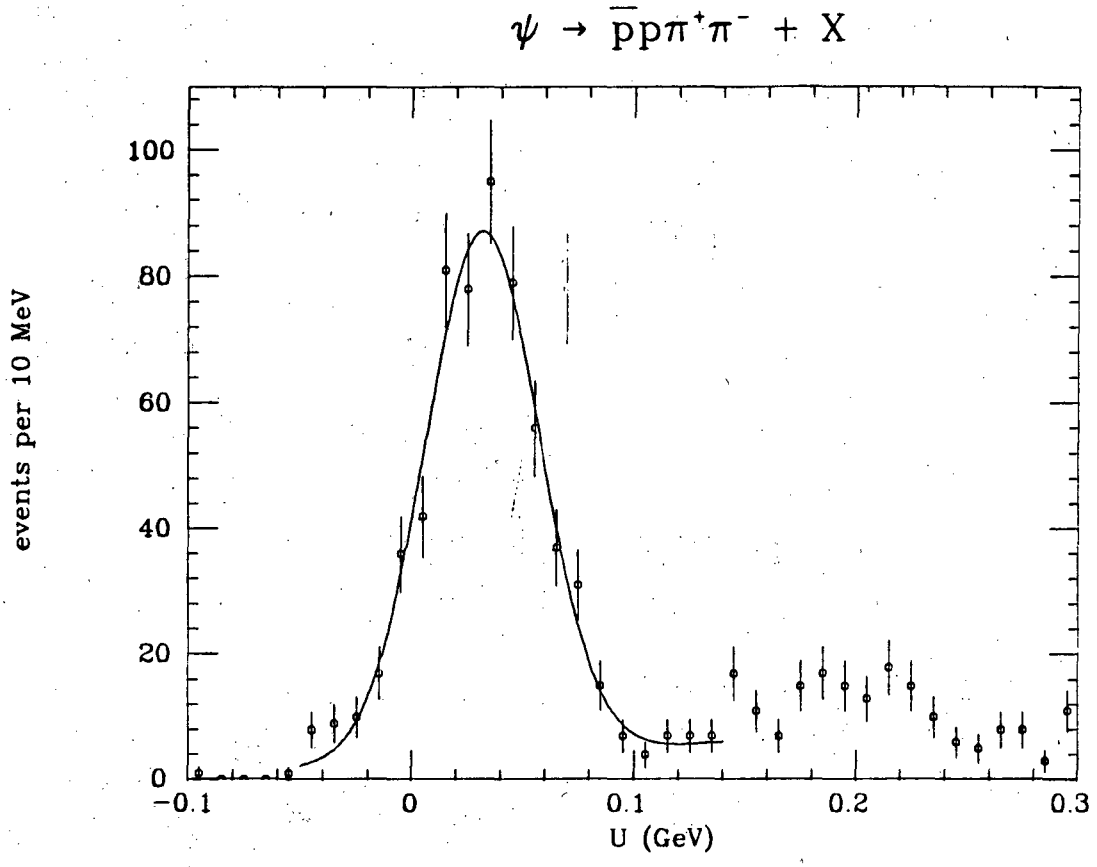

Figure 49: The quantity U for all $\bar{p}p\pi^+\pi^-$ events. Solid curve is fit described in text.

We have already placed a limit on (83) in section 5.9.2, and found a null result, so there is no background subtraction.

To determine the number of events due to reaction (84), we plot the quantity U for all events with $m(\bar{p}p\pi^+\pi^-) < 3$ GeV/c^2, shown in figure 49. We extract the number of events by fitting the peak to the hypothesis of a Gaussian plus a quadratic background. The results of the fit (χ^2 = 16.0/14 DF) give us

$$542 \pm 66 \text{ events.} \qquad (118)$$

Included in this number are contributions from

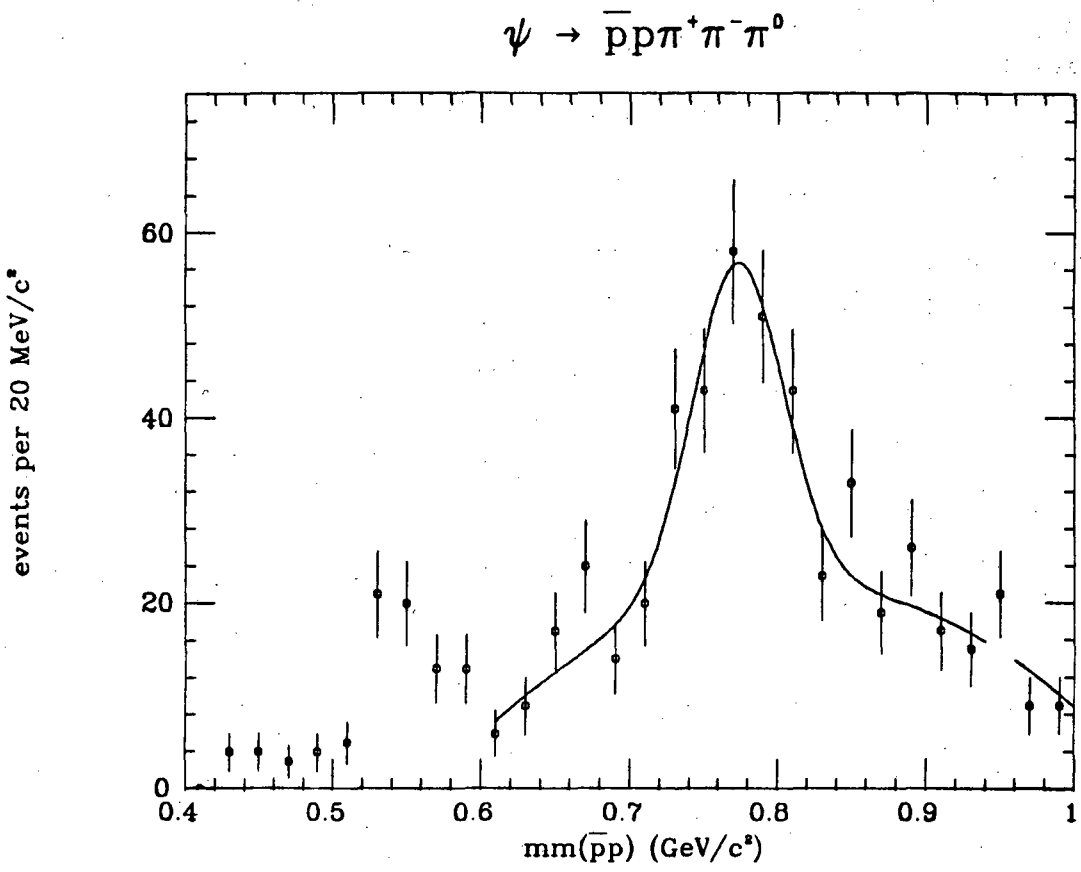

Figure 50: Missing mass opposite the $\bar{p}p$ system. Solid curve is fit described in text.

$$\psi \rightarrow \bar{p}p\omega, \tag{79}$$

and

$$\psi \rightarrow \bar{p}p\eta. \tag{75}$$

Figure 50 shows the missing mass against the $\bar{p}p$ system for these events. the contributions from the decays (79) and (75) are clearly visible. To ascertain the number of events from reaction (79), we fit the background region plus the signal region to the hypothesis of a Gaussian plus a quadratic background. The $\bar{p}p\eta'$

feed through region (one bin) is excluded from the fit. The results of the fit (χ^2 = 17.1/16 DF) gives us a total of

$$136 \pm 22 \text{ events}, \tag{119}$$

attributable to the decay (79). Our efficiency, determined from the same Monte Carlo as discussed in section 5.6.1, is

$$\epsilon = .085, \tag{120}$$

whence

$$BR(\psi \to \bar{p}p\omega) = (1.21 \pm .19 \pm .20)\times 10^{-3}, \tag{121}$$

including 15% model uncertainty.

The contribution from reaction (75) is more difficult to calculate due to its small size. We proceed intrepidly and handfit the background underneath the $\bar{p}p\eta$ signal region. Based on the analysis, we estimate

$$42 \pm 8 \text{ events}, \tag{122}$$

attributable to the decay (75). Our efficiency, determined from the same Monte Carlo as in section 5.5.2, is

$$\epsilon = .017, \tag{123}$$

whence

$$BR(\psi \to \bar{p}p\eta) = (1.9 \pm .4 \pm .5)\times 10^{-3}, \tag{124}$$

with the usual 25% systematic error overall from background subtraction.

5.10.2 Branching fraction

Having accounted for the two known contributions (we neglect the small feed through from the $\bar{p}p\eta'$ decay), we may proceed to calculate the remaining nonresonant contribution. Subtracting (122) and (119) from (118), we get

$$364 \pm 70 \text{ events}, \tag{125}$$

which we attribute to the decay (84). From the phase space simulation, we estimate an efficiency of

$$\epsilon = .082. \tag{126}$$

Combining (125) and (126), we get

$$BR(\psi \to \bar{p}p\pi^+\pi^-\pi^0) = (3.36 \pm .65 \pm .28)\times 10^{-3}, \tag{127}$$

which includes an estimated 5% models uncertainty from acceptance and resonance considerations.

5.11 SUMMARY

5.11.1 Discussion of non-strange baryon decays

The MKI[62] has found

$$BR(\psi \to \bar{p}p\gamma) < .11\times 10^{-3}, \tag{128}$$

(± 15% systematic errors).

The γ branching fraction (47) is a factor of 3 larger than the MKI upper limit (128). Consultation with the authors of reference 62 did not resolve the apparent discrepancy. One possible reason for the discrepancy is the superior performance of the MKII liquid argon over the MKI shower counters, which would tend to imply that the MKI shower counter efficiency may have been overestimated.

Furthermore, there appears to be a discrepancy in the MKI paper between the number of observed events, the known sample size, and the quoted detection efficiency.

The possibility has been pointed out that the overall normalization of the two Monte Carlo q^2 spectra in figure 23 might be incorrect in this analysis. This was suggested by the fact that the data point for $.001 < q^2 < .002$ $(GeV/c)^2$ seems to be too low relative to the Monte Carlo spectra point. If the direct photon q^2 distribution is not well reproduced by the Monte Carlo (e.g. the data has a longer tail than the Monte Carlo), then it is possible that the normalizations of the two Monte Carlo distributions could be different. This would tend to decrease the amount of the π^0 background. However, since the bin $q^2 < .001$ $(GeV/c)^2$ is predominantly direct photon events, in order for the Monte Carlo to remain consistent with the data, the number of direct photon events will not radically change and is thus relatively insensitive to the π^0 subtraction.

Since we have measured the branching ratios for reactions $\psi \to \bar{p}p$ (29) and $\psi \to \bar{p}p\gamma$ (39), we may compare the ratio of the two branching fractions (47) and (36) with the first order QCD prediction[24] for the direct photon branching fraction

$$BR(\psi \to \gamma X) = .08. \tag{129}$$

We have measured

$$\frac{BR(\psi \to \bar{p}p\gamma)}{BR(\psi \to \bar{p}p)} = .18 \pm .04. \tag{130}$$

It would seem that the direct photon decay $\psi \to \bar{p}p\gamma$ (39) occurs more frequently than one would have imagined, suggesting that the two gluon decay to $\bar{p}p$ is preferential to the three gluon decay.

The x spectrum of the direct photon in the decay $\psi \to \bar{p}p\gamma$ has been calculated and compared with the first order QCD prediction. No conclusive evidence for a possible two gluon state opposite the direct photon is possible with our statistics.

We have presented the constrained Dalitz plot for the decays $\psi \to \bar{p}\pi^+n$ (53) and $\psi \to p\pi^-\bar{n}$ (52), and noted resonant contributions. Evidence for the decay $\psi \to N^*N$ at the level of 20% to 40% of the rate of $\psi \to \bar{p}p$ has been shown. Further conclusions at this level of analysis regarding resonance formation are difficult.

Since the ψ is an isoscalar, we can make an absolute prediction for the ratios of these two decays and the decay $\psi \to \bar{p}p\pi^0$, discussed in section 5.4.2. From simple Clebsch-Gordan arguments, it follows that the branching fractions $\psi \to \bar{p}p\pi^0$, $\psi \to \bar{p}\pi^+n$, and $\psi \to p\pi^-\bar{n}$ should be in the ratios 1:2:2. The results of this experiment (58), (59), and (71) are in excellent agreement with this prediction.

We have presented the constrained Dalitz plot for the decay $\psi \to \bar{p}p\pi^0$ (50). Even with the large contamination of $\bar{p}p\gamma$ events N^*N production has been observed. The two different values (62) and (74) for the branching fraction $\psi \to \bar{p}N^{*+}(1470) + c.c.$ agree remarkably well with each other, despite the crudity of the measurements.

We have presented the constrained Dalitz plot for the decay $\psi \to \bar{p}p\eta$ (75). The Dalitz plot population is inconsistent with that expected by a pure phase space distribution. Resonance production is possible, but difficult at this level of analysis to determine due to the nonuniform Dalitz plot density.

We have investigated the Dalitz plot for $\bar{p}p$ events which are consistent with the decay $\psi \to \bar{p}p\omega$ (79). No evidence of resonance formation was found.

The MKI[62] has found

$$BR(\psi \to \bar{p}p\eta') = (1.8 \pm .6)\times 10^{-3}, \qquad (131)$$

(± 15% systematic errors). The two experiments disagree at the 2σ level based on statistical errors alone. In order to check our results, we investigated the $\eta\pi\pi$ decay mode of the η'. As mentioned in section 5.7.1, our detection efficiency is dramatically suppressed. Based on the data in the $\rho^0\gamma$ decay mode and our Monte Carlo simulation, we would expect

$$\simeq 1 \text{ event}, \qquad (132)$$

in the $\eta\pi^+\pi^-$ decay mode of the η'. The data has two events in the region of the η' mass on a background of less than an event. Our two results are certainly consistent. In addition, the MKI result involves a substantial background subtraction.

Examination of the various Goldhaber plots for the reaction $\psi \to \bar{p}p\pi^+\pi^-$ (92) yields the following information:

1. The neutral $p\pi$ Goldhaber plot shows essentially no structure in it, apart from a small residual $\Lambda\bar{\Lambda}$ contamination. The phase space Monte Carlo is in good agreement with the data.

2. The doubly charged $p\pi$ Goldhaber plot exhibits strong resonance production. Roughly 20% of the doubly charged $p\pi$ pairs are consistent with arising from Δ^{++} decays. The two body decay $\psi \to \Delta^{++}\bar{\Delta}^{--}$ (97) is seen, as well as the three body decays $\psi \to \Delta^{++}\bar{p}\pi^{-}$ + c.c. (108).
3. The Goldhaber plot of the dipion mass vs. the dibaryon mass exhibits no structure. In particular, the three body decay $\psi \to \bar{p}p\rho$ (110) is strongly suppressed.
4. Reexamination of the neutral $p\pi$ Goldhaber plot after explicitly removing Δ^{++} events show some evidence for Δ^{0} production. Since the ψ is an isoscalar, all four of the I = 3/2 isospin states should be evenly[63] populated. Consequentially, the fraction of Δ^{++} pairs should be nine times that of the Δ^{0} pairs, as the Δ^{0} decays to $p\pi^{-}$ only one third of the time. Our measured rates (114) and (100) are in good agreement with I-spin conservation.

We may use our limit on the decay $\psi \to \bar{p}p\pi^{+}\pi^{-}\gamma$ (117) to gain some information on the two gluon decay to hadrons. We have measured

$$\frac{BR(\psi \to \bar{p}p\pi^{+}\pi^{-}\gamma)}{BR(\psi \to \bar{p}p\pi^{+}\pi^{-})} < .12. \qquad (133)$$

This experiment is not sufficient to establish a preference for either the two gluon or the three gluon decay mode into $\bar{p}p\pi^{+}\pi^{-}$.

The MKI[62] has found

$$BR(\psi \to \bar{p}p\pi^{+}\pi^{-}\pi^{0}) = (1.6 \pm .6)\times 10^{-3}, \qquad (134)$$

(± 15% systematic errors). The two measurements (134) and (127) differ by 2σ. The MKI measurement (134) consists of relatively larger subtractions from the total number of events due to known resonant contributions $\psi \to \bar{p}p\eta$ (75) and $\psi \to \bar{p}p\omega$ (79) than the MKII measurement (127). We also know that the subtracted components in the MKII measurement have branching fractions (121) and (124) which agree well with those measured previously, (82) and (78).

5.11.2 Summary of non-strange decays

In table 3, we summarize all the results presented in the chapter, including instances where more than one measurement of a given mode has been made. In table 4, we summarize the results of this chapter for both this experiment and the MKI experiment. When more than one measurement has been made from this experiment, we list the "best" result, where "best" is defined as the measurement with the smallest combined error.

TABLE 3

Chapter summary of non-strange decays (units of 10^{-3})

Decay mode	Events	ϵ	BR for this experiment
$\psi \to \bar{p}p$	1420 ± 37	.497	2.16 ± .07 ± .15 (36)
$\psi \to \bar{p}p\gamma$	49 ± 9	.195	.38 ± .07 ± .07 (47)
$\psi \to \bar{p}p\pi^0$	69 ± 8	.074	1.42 ± .16 ± .23 (50)
	685 ± 56	.458	1.13 ± .09 ± .09 (71)
$\psi \to p\pi^-\bar{n}$	1288 ± 47	.482	2.02 ± .07 ± .16 (58)
$\psi \to \bar{p}\pi^+n$	1191 ± 47	.467	1.93 ± .07 ± .16 (59)
$\psi \to \bar{p}N^{*+}(1470?)$ + c.c.	209 ± 31	.178	.89 ± .13 ± .22 (62)
	100 ± 25	.090	.84 ± .21 ± .21 (74)
$\psi \to \bar{p}N^{*+}(1670?)$ + c.c.	85 ± 24	.150	.43 ± .10 ± .11 (65)
$\psi \to \bar{p}p\eta$	826 ± 52	.309	2.03 ± .13 ± .15 (78)
	42 ± 8	.017	1.9 ± .4 ± .5 (124)
$\psi \to \bar{p}p\omega$	486 ± 73	.323	1.10 ± .17 ± .18 (82)
	136 ± 22	.085	1.21 ± .19 ± .20 (121)
$\psi \to \bar{p}p\eta'$	19 ± 6	.021	.68 ± .23 ± .17 (91)
$\psi \to \bar{p}p\pi^+\pi^-$	1435 ± 38	.168	6.46 ± .17 ± .43 (95)
$\psi \to \Delta^{++}\bar{\Delta}^{--}$	233 ± 19	.160	1.05 ± .09 ± .26 (104)
$\psi \to \Delta^{++}\bar{p}\pi^-$ + c.c.	332 ± 49	.159	1.40 ± .19 ± .35 (109)
$\psi \to \bar{p}p\rho$	38 ± 16	.158	< .31 (112)
$\psi \to \bar{p}p\pi^+\pi^-\gamma$	< 12	.023	< .79 (117)
$\psi \to \bar{p}p\pi^+\pi^-\pi^0$	364 ± 70	.082	3.36 ± .65 ± .28 (127)

TABLE 4

Comparison of non-strange decays of $\psi(3.095)$ (units of 10^{-3})

Decay mode	This experiment	MKI[62] (± 15% sys. errors)
$BR(\psi \to \bar{p}p)$	$2.16 \pm .07 \pm .15$	$2.2 \pm .2$
$BR(\psi \to \bar{p}N^{*+}(1470?) + c.c.)$	$.89 \pm .13 \pm .22$	
$BR(\psi \to \bar{p}N^{*+}(1670?) + c.c.)$	$.43 \pm .10 \pm .11$	
$BR(\psi \to \Delta^{++}\bar{\Delta}^{--})$	$1.05 \pm .09 \pm .26$	
$BR(\psi \to \bar{p}p\gamma)$	$.38 \pm .07 \pm .07$	$< .11$
$BR(\psi \to \bar{p}p\pi^0)$	$1.13 \pm .09 \pm .09$	$1.00 \pm .15$
(incl. $\bar{p}N^{*+}(1470?) + c.c.$)		
$BR(\psi \to p\pi^-\bar{n})$	$2.02 \pm .07 \pm .16$	$2.16 \pm .29$
(incl. $p\bar{N}^{*-}(1470?)$ and $p\bar{N}^{*-}(1670?)$)		
$BR(\psi \to \bar{p}\pi^+n)$	$1.93 \pm .07 \pm .16$	$2.04 \pm .27$
(incl. $\bar{p}N^{*+}(1470?)$ and $\bar{p}N^{*+}(1670?)$)		
$BR(\psi \to \Delta^{++}\bar{p}\pi^- + c.c.)$	$1.40 \pm .19 \pm .35$	
$BR(\psi \to \bar{p}p\eta)$	$2.03 \pm .13 \pm .15$	$2.3 \pm .4$
$BR(\psi \to \bar{p}p\rho)$	$< .31$	
$BR(\psi \to \bar{p}p\omega)$	$1.10 \pm .17 \pm .18$	$1.6 \pm .3$
$BR(\psi \to \bar{p}p\eta')$	$.68 \pm .23 \pm .17$	$1.8 \pm .6$
$BR(\psi \to \bar{p}p\pi^+\pi^-)$	$6.46 \pm .17 \pm .43$	$5.5 \pm .6$
(incl. $\Delta^{++}\bar{\Delta}^{--}$ and $\Delta^{++}\bar{p}\pi^- + c.c.$)		
$BR(\psi \to \bar{p}p\pi^+\pi^-\gamma)$	$< .79$	
$BR(\psi \to \bar{p}p\pi^+\pi^-\pi^0)$	$3.36 \pm .65 \pm .28$	$1.6 \pm .6$

Chapter VI

HYPERON DECAYS OF ψ(3.095)

6.1 THE DECAY $\psi \to \Lambda\bar{\Lambda}$

6.1.1 Data reduction

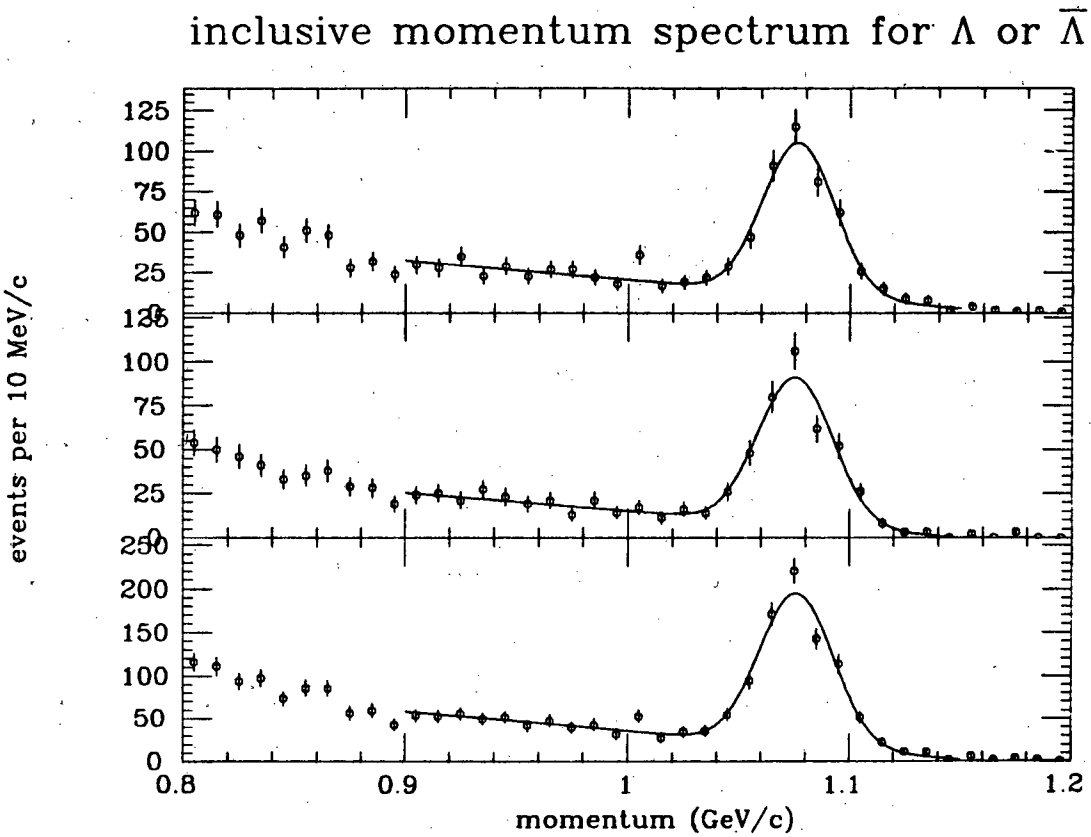

Figure 51: Inclusive momentum spectrum of Λ or $\bar{\Lambda}$ at the ψ.
a) Λ
b) $\bar{\Lambda}$
c) both Λ and $\bar{\Lambda}$ added

The selection of particles decaying at a secondary vertex has been discussed in section 3.4.2. For this measurement, we make the additional requirement that the secondary vertex lie at least 8mm in the transverse direction from the beam-beam interaction point. Figure 51 shows the inclusive momentum spectrum of Λ and $\bar{\Lambda}$ at the ψ. There is a clear enhancement centered near $p = 1.07$ GeV/c, which corresponds to the decay

$$\psi \rightarrow \Lambda\bar{\Lambda}. \qquad (135)$$

6.1.2 Angular distribution

For events which have a Λ or $\bar{\Lambda}$ with $1.05 < p < 1.12$ GeV/c, we form the angular distribution of the Λ direction with respect to the positron beam direction. Only one VEE per event is allowed to enter the plot if both are reconstructed.

In order to determine our acceptance, events of the topology (135) are generated in the following way:

1. A random number is thrown to determine the ψ decay angle with respect to the positron direction.
2. A random number is thrown to determine the ψ helicity state along the positron beam direction.[64]
3. Using the known spin rotation matrices,[65] the ψ helicity is calculated along the ψ decay angle.
4. The Λ and $\bar{\Lambda}$ helicities are then determined by the ψ helicity state by addition of angular momenta. In the case of the $|1,0\rangle$ helicity state, a random number is thrown to distinguish between the two possibilities.

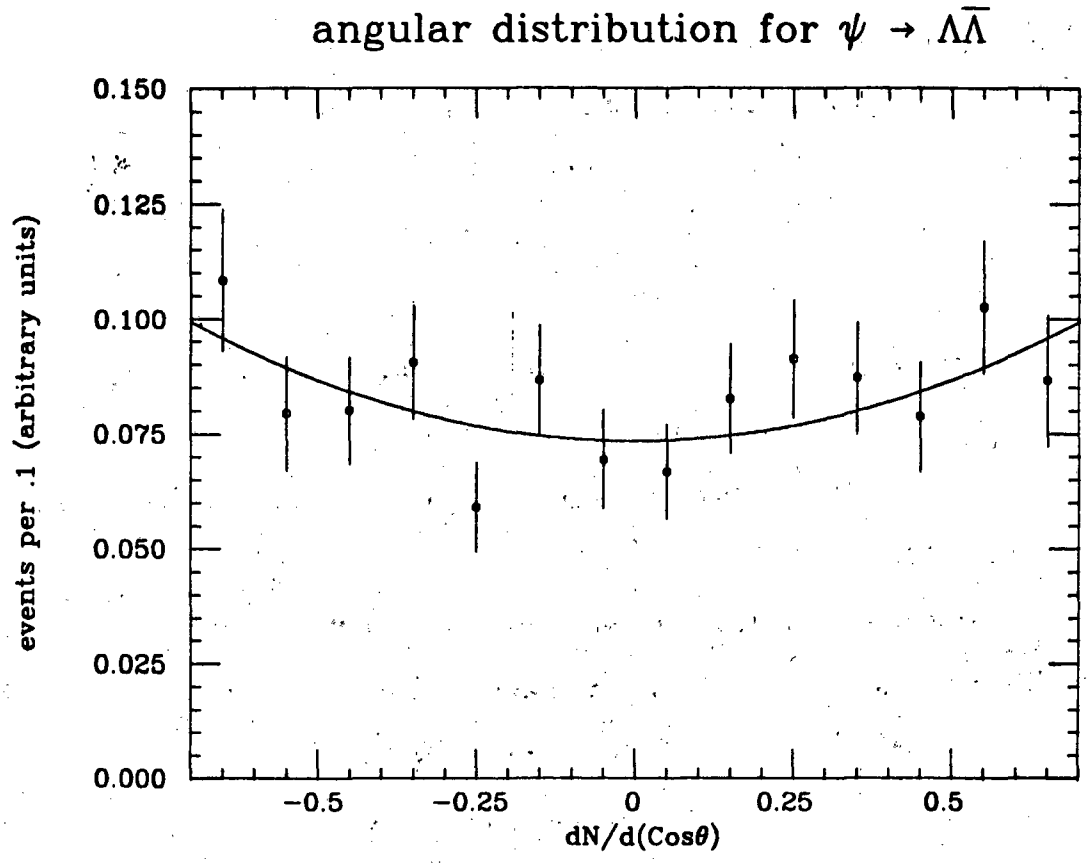

Figure 52: Angular distribution for $\psi \rightarrow \Lambda\bar{\Lambda}$. Solid curve is fit describe in text.

5. The Λ and $\bar{\Lambda}$ are then decayed according to the (see appendix A) known polarized angular distributions

$$\frac{dN_p}{dx} = 1 \pm \alpha \mathrm{Cos}x, \qquad (136)$$

where x is the angle between the decay proton and the hyperon polarization (in this case the Λ line of flight), and α is a measured parameter which is the asymmetry of the hyperon decay. For Λ decay,

$$\alpha = -.622 \pm .048 \qquad (137)$$

The positive sign in (136) corresponds to positive helicity, and the negative sign to negative helicity. A random number is then thrown, weighted by the polarized decay distribution (136), which determines the hyperon decay products direction in the hyperon rest system. With this, the event generation is complete.

An acceptance is then calculated as a function of polar angle Cosθ. We then divide the data distribution by the Monte Carlo distribution to get the acceptance corrected angular distribution, shown in figure 52.

Spin-spin correlations were kept in the Monte Carlo as a check on how these correlations might affect the angular acceptance. We also generated events of the topology (135) according to a phase space distribution for comparison, as there can be no <u>net</u> polarization of the Λ's from an unpolarized ψ. The angular acceptance is found to be insensitive for this measurement to spin-spin correlations. As a result, all subsequent analyses of ψ decays involving hyperons will use a phase space Monte Carlo as it is conceptually much simpler to understand.

The acceptance corrected distribution is then fit to the hypothesis (31). The results of the fit (χ^2 = 10.7/12 DF) give us

$$\alpha = .72 + .38 - .34. \qquad (138)$$

In figure 52, there is a small feed through from events other than from (135). We have repeated the analysis defining a "Λ" as a sideband outside of the true Λ mass range, adjusting the momentum

cut such that these fake Λ's have the beam energy, and then made the same data plot as in figure 52. Very few events survive this analysis, and within errors their contribution is consistent with that of the actual distribution. Thus we are justified in ignoring the contamination from events not arising from (135) in the calculation of (138).

6.1.3 Branching fraction

Having determined the angular distribution of $\Lambda\bar{\Lambda}$ pa[illegible] (138), we may now calculate the branching fraction for (135). Figure 51 shows the inclusive momentum spectra for both charge modes separately, as well as the sum of the two charge modes. We individually fit each of the three plots to a Gaussian with a linear background, shown as the solid curves in figure 51. For the Λ, we get (χ^2 = 18.9/20 DF)

$$N_\Lambda = 378 \pm 23 \text{ events}, \tag{139}$$

while for the $\bar{\Lambda}$ we get (χ^2 = 14.3/20 DF)

$$N_{\bar{\Lambda}} = 352 \pm 22 \text{ events}, \tag{140}$$

and for both modes we get (χ^2 = 23.1/20 DF)

$$N_{\Lambda \text{ or } \bar{\Lambda}} = 734 \pm 32 \text{ events}. \tag{141}$$

Note the excellent agreement between the sum of (139) and (140) with (141).

We are now ready to calculate the branching fraction. We use the same Monte Carlo as mentioned in section 6.1.2, with the exception that we weight the events with the measured production distri-

bution α given by (138). The acceptances, corrected for the $\Lambda\bar{\Lambda}$ angular distribution, are respectively

$$\epsilon_{\Lambda} = .181, \tag{142}$$

and

$$\epsilon_{\bar{\Lambda}} = .170, \tag{143}$$

where we have included a factor of .642 for the $\Lambda \to p\pi^-$ branching fraction. We can separately calculate the branching fraction for (135) from the combination of (139) and (142)

$$BR(\psi \to \Lambda\bar{\Lambda}) = (1.58 \pm .10 \pm .19)\times 10^{-3}, \tag{144}$$

and the combination of (140) and (143)

$$BR(\psi \to \Lambda\bar{\Lambda}) = (1.57 \pm .10 \pm .19)\times 10^{-3}. \tag{145}$$

All measurements include a systematic error of $.12\times 10^{-3}$ due to the systematic error in the production angular distribution (138). By virtue of the two data samples (139) and (140) being relatively independent,[66] we may combine the two results (144) and (145) to reduce the statistical error somewhat, whence

$$BR(\psi \to \Lambda\bar{\Lambda}) = (1.58 \pm .08 \pm .19)\times 10^{-3}, \tag{146}$$

6.2 THE DECAYS $\psi \to \bar{p}K^+\Lambda$ AND $\psi \to pK^-\bar{\Lambda}$

6.2.1 Data reduction

For events which have two oppositely charged tracks which satisfy the proton and kaon TOF hypotheses, we plot the missing mass opposite the pK system, shown in figure 53a). There are two clear peaks in the vicinity of 1.15 GeV/c^2. The first peak, centered near 1.115 GeV/c^2, we attribute to the decays

$$\psi \to \bar{p}K^+\Lambda, \tag{147}$$

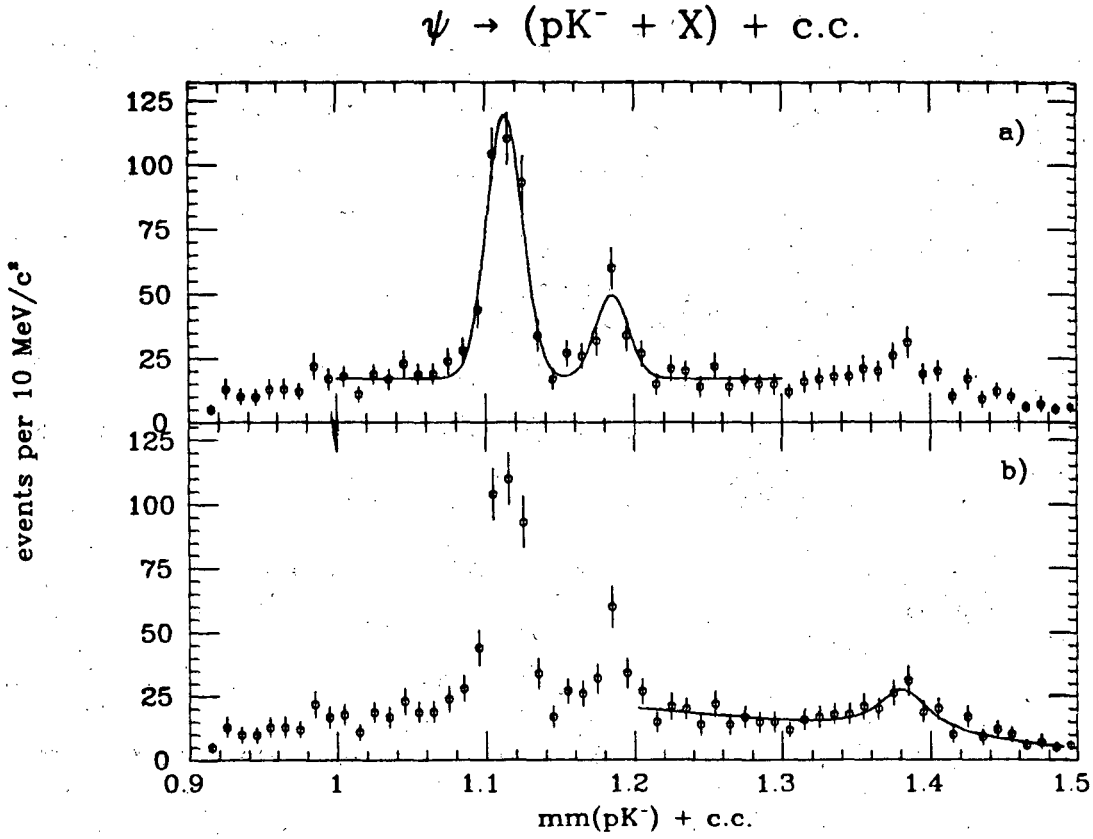

Figure 53: Missing mass opposite pK^- and $\bar{p}K^+$ pairs combined. Solid curves are fits described in text. The same data is plotted in both a) and b) to illustrate the different fits.

and

$$\psi \rightarrow pK^-\bar{\Lambda}, \tag{148}$$

while the peak centered near 1.19 GeV/c^2 we attribute to the decays

$$\psi \rightarrow \bar{p}K^+\Sigma^0, \tag{149}$$

and

$$\psi \rightarrow pK^-\bar{\Sigma}^0. \tag{150}$$

These are the first observations of three-body decays the ψ to hyperons in the final state.

6.2.2 Branching fraction

Due to the proximity of the Λ and the Σ^0 masses, we simultaneously fit the missing mass spectrum of both peaks to Gaussians plus a flat background. The simultaneous fit properly accounts for the background under the peaks. The results of the fit (χ^2 = 24.5/23 DF) give us a total of

$$307 \pm 25 \text{ events,} \tag{151}$$

which we attribute to the decays (147) and (148). From the phase space Monte Carlo, we estimate an efficiency of

$$\epsilon = .262, \tag{152}$$

whence combining (151) and (152), we get

$$BR(\psi \to \bar{p}K^+\Lambda + c.c.) = (.89 \pm .07 \pm .14)\times 10^{-3}, \tag{153}$$

which includes an estimated 15% model dependent error from resonance and acceptance considerations.

We have investigated the constrained Dalitz plot for these events. No evidence was found for any resonance formation.

6.3 THE DECAYS $\psi \to \bar{p}K^+\Sigma^0$ AND $\psi \to pK^-\bar{\Sigma}^0$

6.3.1 Branching fraction

Data reduction has been discussed in section 6.2.1. There is clear evidence for decays (149) and (157) in figure 53a). We determined the number of events from reaction (149) and (150) by a simultaneous fit to the Λ and Σ peaks, discussed in section 6.2.2. The results of the fit give us a total of

$$90 \pm 19 \text{ events.} \tag{154}$$

From the phase space Monte Carlo, we estimate an efficiency of

$$\epsilon = .236. \quad (155)$$

The branching fraction is

$$BR(\psi \to \bar{p}K^+\Sigma^0 + c.c.) = (.29 \pm .06 \pm .05)\times 10^{-3}, \quad (156)$$

which includes an estimated 15% model dependent systematic error.

6.4 THE DECAYS $\psi \to \bar{p}K^+\Sigma^{*0}(1385)$ AND $\psi \to pK^-\bar{\Sigma}^{*0}(1385)$

6.4.1 Branching fraction

Data reduction has already been discussed in section 6.2.1. The missing mass against the pK system is replotted in figure 53b). There is a broad but unmistakable peak centered near 1.38 GeV/c^2, which we attribute to the decays

$$\psi \to \bar{p}K^+\Sigma^{*0}(1385), \quad (157)$$

and

$$\psi \to pK^-\bar{\Sigma}^{*0}(1385). \quad (158)$$

In order to estimate the number of events in the peak, we fit the spectrum to the hypothesis of an P-wave, non-relativistic Breit-Wigner on a linear background. The results of the fit (χ^2 = 20.7/27 DF) give us a total of

$$115 \pm 46 \text{ events}. \quad (159)$$

From the phase space Monte Carlo, we estimate our detection efficiency to be

$$\epsilon = .132. \quad (160)$$

Combining (159) and (160), our result is

$$BR(\psi \to \bar{p}K^+\Sigma^{*0}(1385) + c.c.) = (.66 \pm .26 \pm .11)\times 10^{-3}, \quad (161)$$

which includes the usual 15% model dependent systematic error.

6.5 THE DECAYS $\psi \to \Lambda\pi^-\bar{\Sigma}^+$ and $\psi \to \bar{\Lambda}\pi^+\Sigma^-$

6.5.1 Data reduction

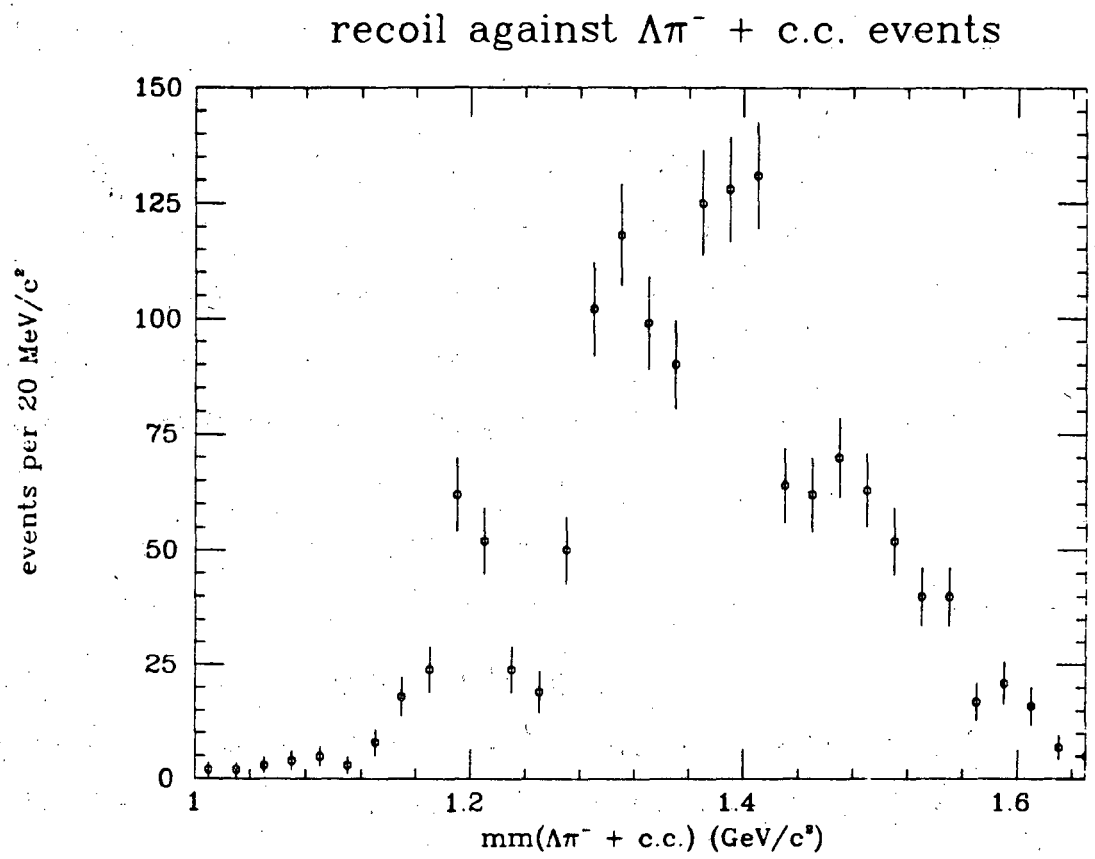

Figure 54: Missing mass opposite $\Lambda\pi^-$ + c.c. events.

Candidate events are selected by taking $\Lambda\pi^-(\bar{\Lambda}\pi^+)$ events, where the π^- is required to have $|z| < 8$cm and $r < 1.5$cm with respect to the primary vertex. In addition, the pion is required not to originate from another secondary vertex. For these events, we plot the missing mass opposite the $\Lambda\pi$ system, shown in figure 54. There is a clear enhancement centered near 1.18 GeV/c^2, which we attribute to the decays

$$\psi \to \Lambda\pi^-\bar{\Sigma}^+, \tag{162}$$

and

$$\psi \to \bar{\Lambda}\pi^+\Sigma^-. \tag{163}$$

6.5.2 Branching fraction

In order to determine the number of events due to reactions (162) and (163), we must subtract off the background component. For this analysis, this is a very difficult process. Real $\Lambda\pi$ events must have either another $\Lambda\pi$ or a stable particle like the Σ recoiling against it in order to simultaneously conserve charge and strangeness. $\Lambda\pi$ threshold is at about 1.25 GeV/c^2. Therefore, the background must radically change slope in the vicinity of the higher edge of the Σ peak. Consequently, we use our theoretical prejudice and hand subtract the background due to the especially volatile nature of the background behavior. This leaves us with

$$135 \pm 15 \text{ events}, \tag{164}$$

which we attribute to the reactions (162) and (163). The phase space Monte Carlo estimates our efficiency to be

$$\epsilon = .067, \tag{165}$$

whence

$$BR(\psi \to \Lambda\pi^-\bar{\Sigma}^+ + \text{c.c.}) = (1.53 \pm .17 \pm .38)\times 10^{-3}, \tag{166}$$

where we have included an estimated 25% overall systematic error from background and resonance considerations.

6.5.3 Resonance production

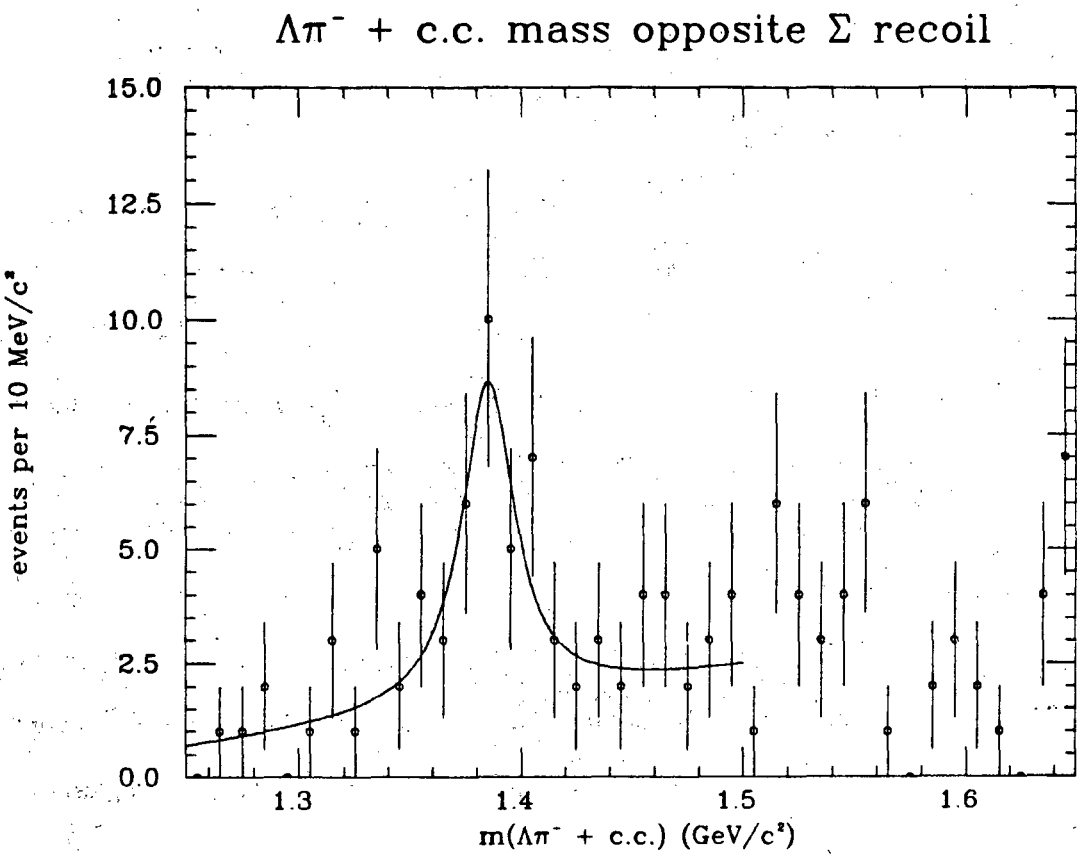

Figure 55: $\Lambda\pi^-$ + c.c. mass opposite Σ recoil. Solid line is fit described in text.

We now investigate the $\Lambda\pi$ system for possible resonance formation, spurred by the hints in section 6.8.1. As will be discussed in section 6.8.1, we were worried about the feed through from the decays (162) and (163) into the $\Sigma^*(1385)$ signal region. We now select events which have $1.14 < mm_{\Lambda\pi} < 1.24$ as $\Lambda\pi$ events which have a Σ recoiling against them. Figure 55 shows the $\Lambda\pi$ mass opposite

the tagged Σ recoil. There is good evidence for the SU(3) violating decays

$$\psi \rightarrow \Sigma^{*-}(1385)\bar{\Sigma}^{+}, \tag{167}$$

and

$$\psi \rightarrow \bar{\Sigma}^{*+}(1385)\Sigma^{-}. \tag{168}$$

To ascertain the resonant contribution, we fit the peak to a nonrelativistic P-wave Breit-Wigner on a linear background. The results of the fit (χ^2 = 14.6/20 DF) give us a total of

$$32 \pm 16 \text{ events}, \tag{169}$$

which we attribute to decays (167) and (168). The phase space Monte Carlo predicts an efficiency of

$$\epsilon = .067, \tag{170}$$

whence

$$BR(\psi \rightarrow \Sigma^{*-}(1385)\bar{\Sigma}^{+} + c.c.) = (.36 \pm .18 \pm .09)\times 10^{-3}, \tag{171}$$

which includes an estimated 25% systematic error from model dependent parameters.

6.6 THE DECAYS $\psi \rightarrow \Lambda\pi^{+}\bar{\Sigma}^{-}$ and $\psi \rightarrow \bar{\Lambda}\pi^{-}\Sigma^{+}$

6.6.1 Branching fraction

Data reduction has already been discussed in section 6.5.1, where we have made the obvious interchange of the opposite sign pion associated with the VEE. For these events, we plot the missing mass opposite the Λπ system, shown in figure 56. While in the previous section, the $\Lambda\pi^{-}$ can be the decay of a Ξ^{-}, here no such decay is present, producing a radically different background shape

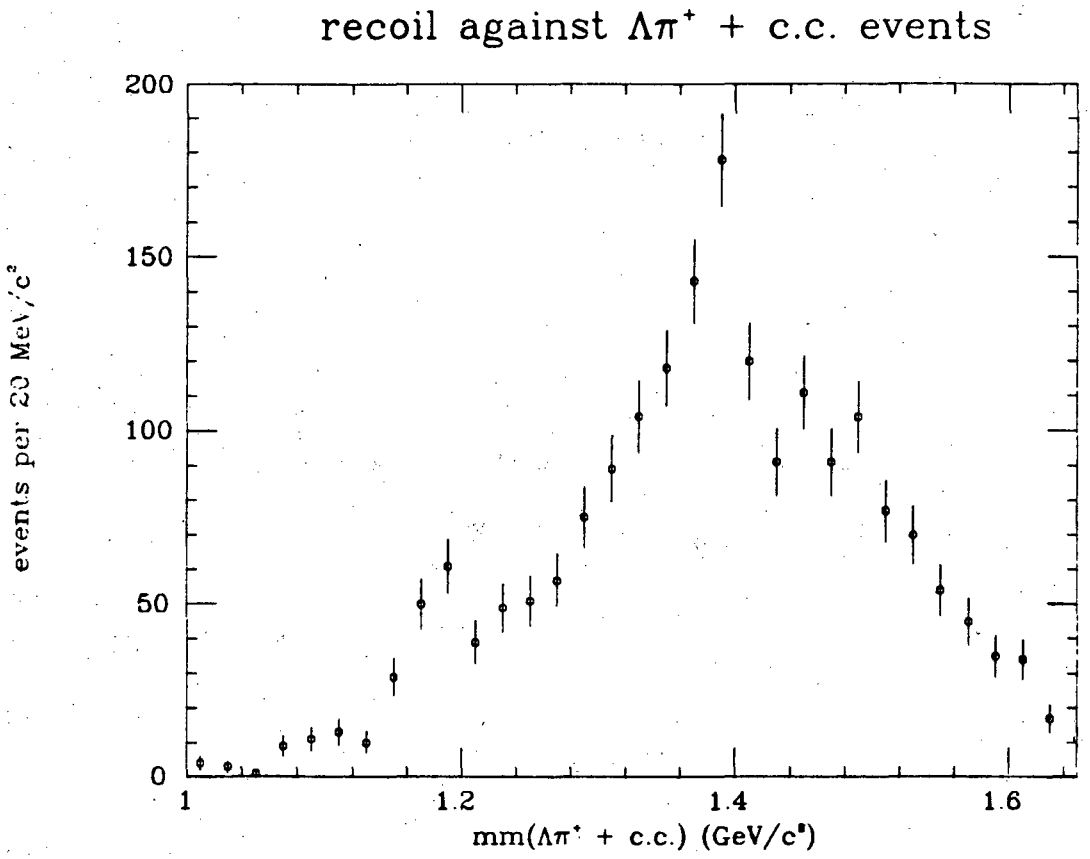

Figure 56: Missing mass opposite $\Lambda\pi^+$ + c.c. events.

in figure 56. There is good evidence for an enhancement on top of a combinatorial background, centered near 1.18 GeV/c^2, which we attribute to the decays

$$\psi \rightarrow \Lambda\pi^+\bar{\Sigma}^-, \tag{172}$$

and

$$\psi \rightarrow \bar{\Lambda}\pi^-\Sigma^+. \tag{173}$$

Again, we have a difficult background subtraction for the reasons mentioned in section 6.5.2. Consequently, we use the prejudices of section 6.5.2 and hand subtract the background. This leaves us with

$$118 \pm 18 \text{ events}, \tag{174}$$

which we attribute to the reactions (172) and (173). The phase space Monte Carlo estimates our efficiency to be

$$\epsilon = .065, \tag{175}$$

whence

$$BR(\psi \to \Lambda\pi^+\bar{\Sigma}^- + \text{c.c.}) = (1.38 \pm .21 \pm .35)\times 10^{-3}, \tag{176}$$

where we have included a 25% overall systematic error.

6.6.2 Resonance production

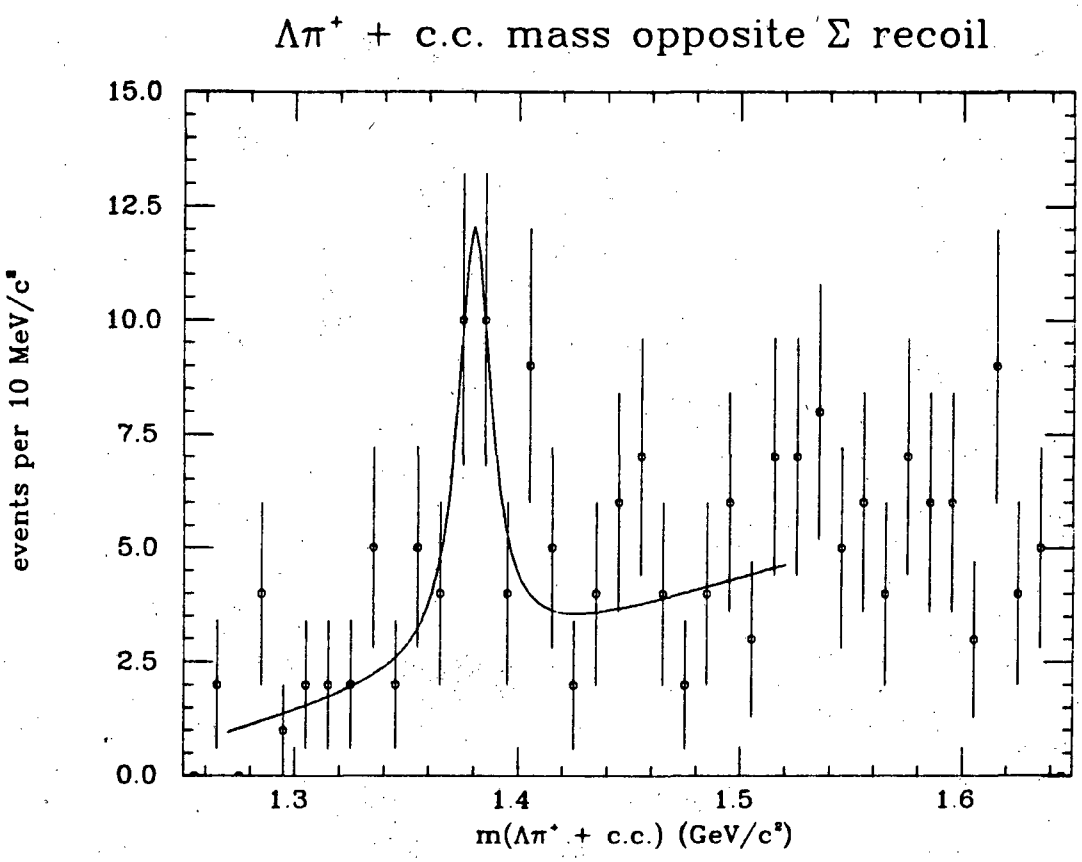

Figure 57: $\Lambda\pi^+$ + c.c. mass opposite Σ recoil. Solid line is fit described in text.

We now investigate the $\Lambda\pi$ system for possible resonance formation, encouraged by the results in section 6.5.3. We select events which have $1.14 < mm_{\Lambda\pi} < 1.24$ as $\Lambda\pi$ events which have a Σ recoiling against them. Figure 57 shows the $\Lambda\pi$ mass opposite the tagged Σ recoil. There is fair evidence for the SU(3) violating decays

$$\psi \rightarrow \Sigma^{*+}(1385)\bar{\Sigma}^{-}, \tag{177}$$

and

$$\psi \rightarrow \bar{\Sigma}^{*-}(1385)\Sigma^{+}. \tag{178}$$

We fit the peak in exactly the same way as in section 6.5.3. The results of the fit (χ^2 = 17.4/20 DF) give us a total of

$$27 \pm 10 \text{ events}, \tag{179}$$

which we attribute to decays (177) and (178). The phase space Monte Carlo predicts an efficiency of

$$\epsilon = .068, \tag{180}$$

whence

$$BR(\psi \rightarrow \Sigma^{*+}(1385)\bar{\Sigma}^{-} + c.c.) = (.30 \pm .11 \pm .08)\times 10^{-3}, \tag{181}$$

which includes an estimated 25% systematic error.

6.7 THE DECAY $\psi \rightarrow \Xi^{-}\bar{\Xi}^{+}$

6.7.1 Data reduction

For events which have either a Λ and additional π^{-} or a $\bar{\Lambda}$ and an π^{+}, we form the invariant mass of the $\Lambda\pi$ system, shown in figure 58. There is a clear enhancement, centered near 1.32 GeV/c^2, indicating $\Xi^{-}(\bar{\Xi}^{+})$ production. For events with

$$1.312 < m_{\Lambda\pi} < 1.33 \text{ GeV}/c^2, \tag{182}$$

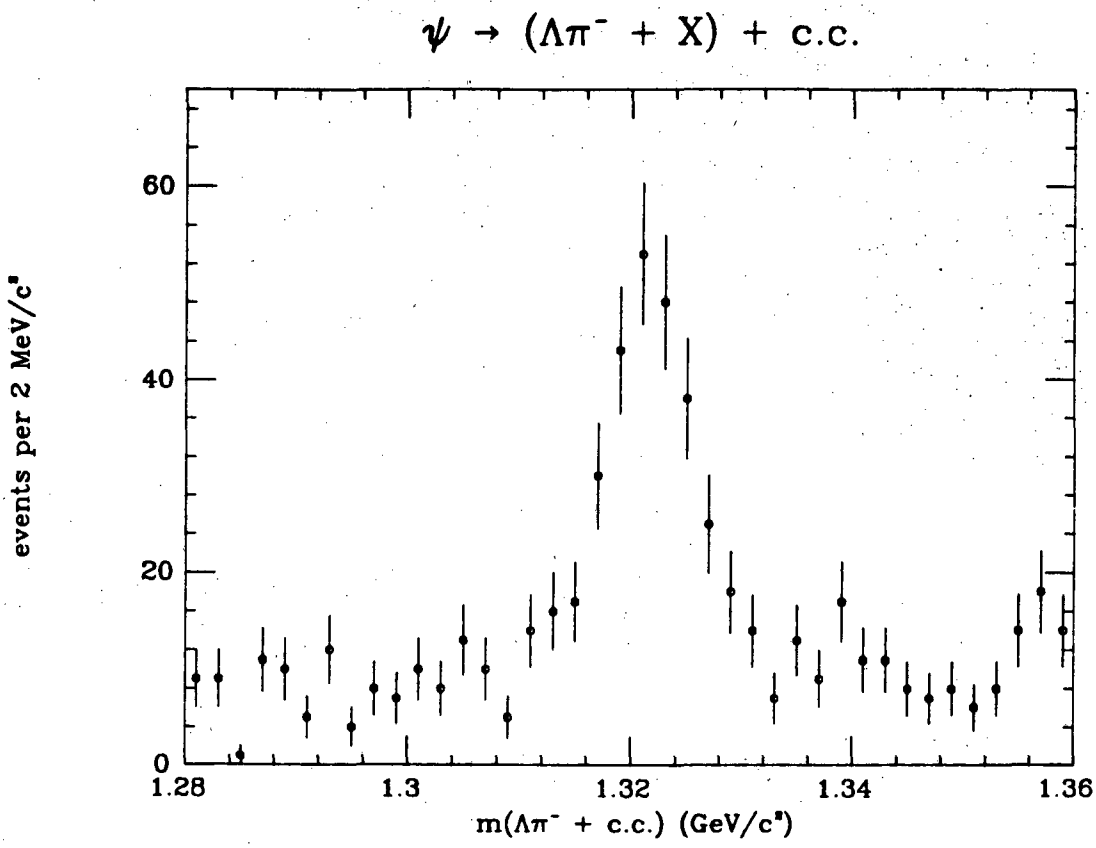

Figure 58: $m(\Lambda\pi^- + c.c.)$.

the three body mass is set to the known (1.32132 GeV/c^2) Ξ^- mass, and the Ξ energy is recalculated. This is very similar to a 1C fit. Figure 59 shows the missing mass opposite the $\Lambda\pi$ system for events which satisfy the Ξ hypothesis. There is a clear enhancement, centered near 1.32 GeV/c^2, which we attribute to the decay

$$\psi \to \Xi^-\bar{\Xi}^+. \qquad (183)$$

Figure 60 shows a beautiful $\psi \to \Xi^-\bar{\Xi}^+$ event.

The events with mm_Ξ > 1.5 GeV/c^2 are due to the decay

$$\psi \to \Xi^-\bar{\Xi}^+\pi^0, \qquad (184)$$

or possibly the SU(3) violating decays

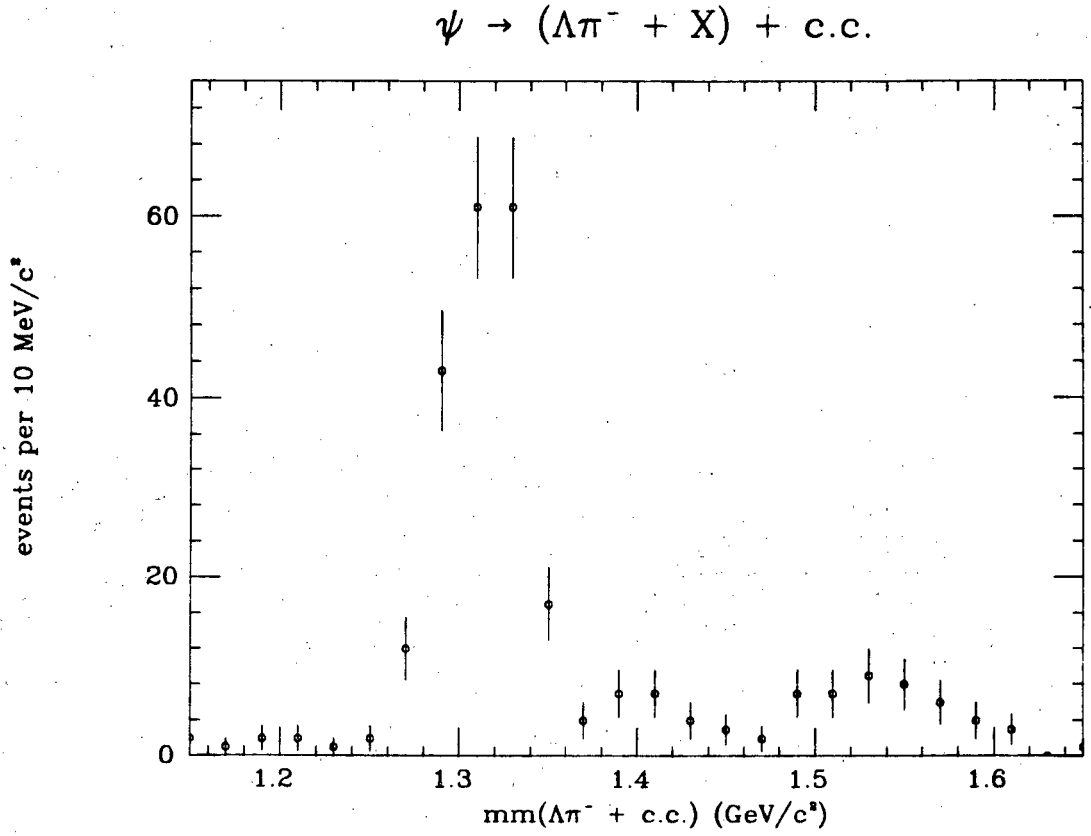

Figure 59: mm(Ξ^- + c.c.).

$$\psi \rightarrow \Xi^-\Xi^{*+}(1530) + \text{c.c.}. \qquad (185)$$

At this stage it is difficult to separate out the two contributions.

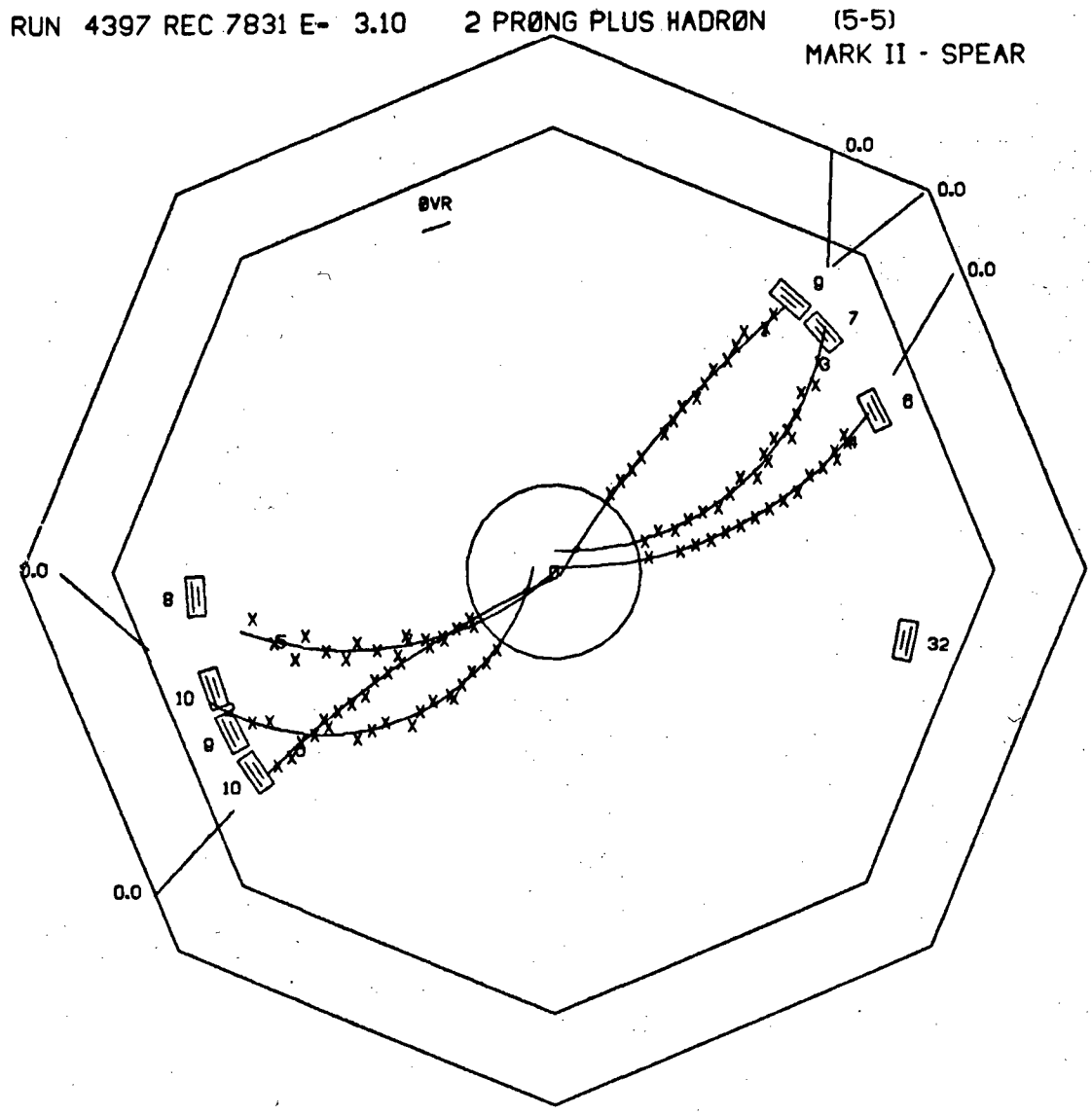

Figure 60: A spectacular $\psi \to \Xi^-\bar{\Xi}^+$ event. Both Λ's decay over 10cm from the primary vertex, and the Ξ vertices are visible as neither of the other two pions seem to come from the primary vertex. Track 1 is an antiproton, track 6 is a proton, tracks 3 and 4 are π^+'s, and tracks 2 and 5 are π^-'s.

6.7.2 Angular distribution

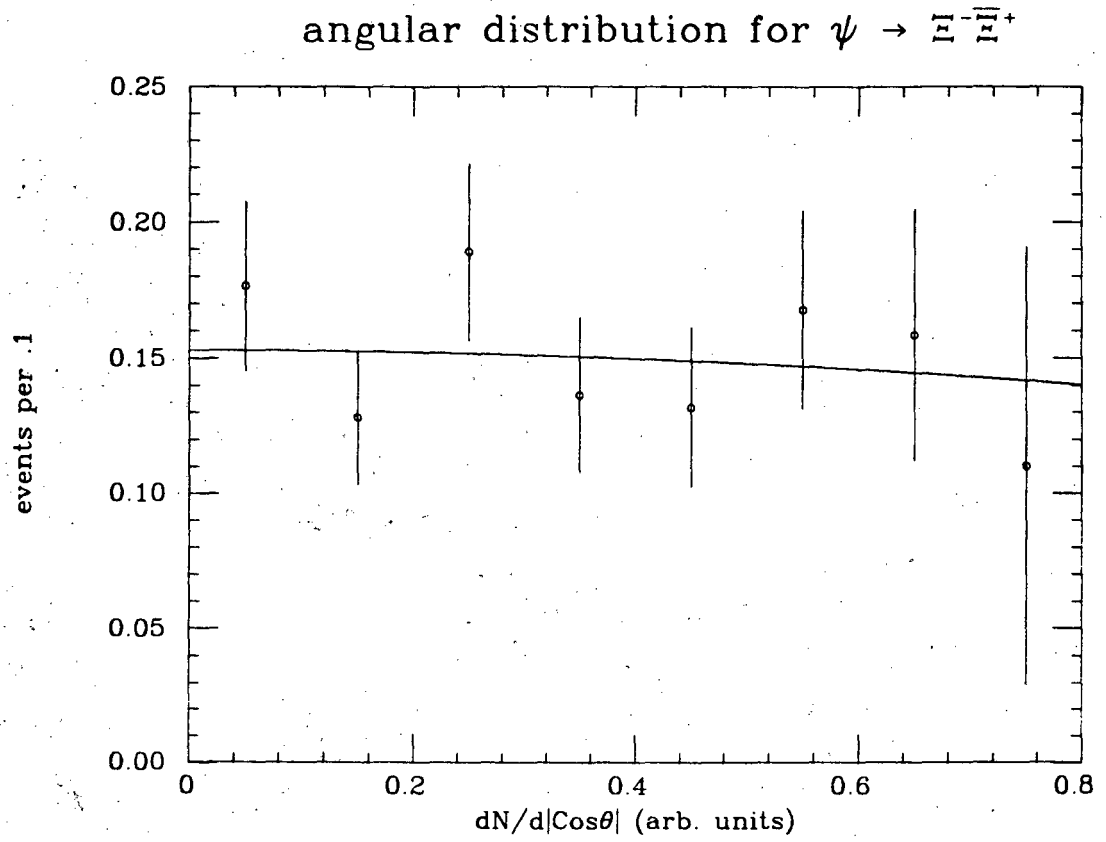

Figure 61: Angular distribution for $\psi \rightarrow \Xi^-\bar{\Xi}^+$.

For events which have

$$1.26 < mm_{\Xi} < 1.36 \text{ GeV}/c^2, \qquad (186)$$

we plot the direction of the Ξ^- with respect to the positron beam direction, shown in figure 61. The distribution has been corrected by acceptance by the phase space Monte Carlo, where spin-spin correlations have been ignored. A fit is done to the hypothesis

$$\frac{dN}{d|Cos\theta|} = N_0(1 + \alpha Cos^2\theta), \qquad (187)$$

where we reflected the distribution about $\cos\theta = 0$ due to the marginal statistics. The results of the fit ($\chi^2 = 4.0/6$ DF) give us

$$\alpha = -.13 + .59 - .51 \qquad (188)$$

Obviously, (188) is not well determined by this experiment.

6.7.3 Branching fraction

From figure 59, we attribute

$$194 \pm 14 \text{ events}, \qquad (189)$$

to the decay (183). Since (188) is very consistent with zero, we do not correct for the production mechanism. From this, we estimate an efficiency of

$$\epsilon = .129. \qquad (190)$$

Combining (189) and (190), we get

$$BR(\psi \to \Xi^-\bar{\Xi}^+) = (1.14 \pm .08 \pm .20)\times 10^{-3}, \qquad (191)$$

where we have included a 15% model dependent systematic error.

6.8 THE DECAY $\psi \to \Sigma^{*-}(1385)\bar{\Sigma}^{*+}(1385)$

6.8.1 Data reduction

Selection of Λ's has been discussed in section 3.4.2. We select pions by imposing the additional constraint that the pion not originate from any secondary vertex. This cut eliminates pions from K_S decays.

For these events, we form the $\Lambda\pi^-(\bar{\Lambda}\pi^+)$ mass, shown in figure 62. There is a narrow Ξ^- peak, centered near 1.32 GeV/c^2, and a broader peak centered near 1.38 GeV/c^2, which we attribute to the P'_{13} I=1 strange baryon resonance, the $\Sigma^{*-}(1385)(\bar{\Sigma}^{*+}(1385))$.

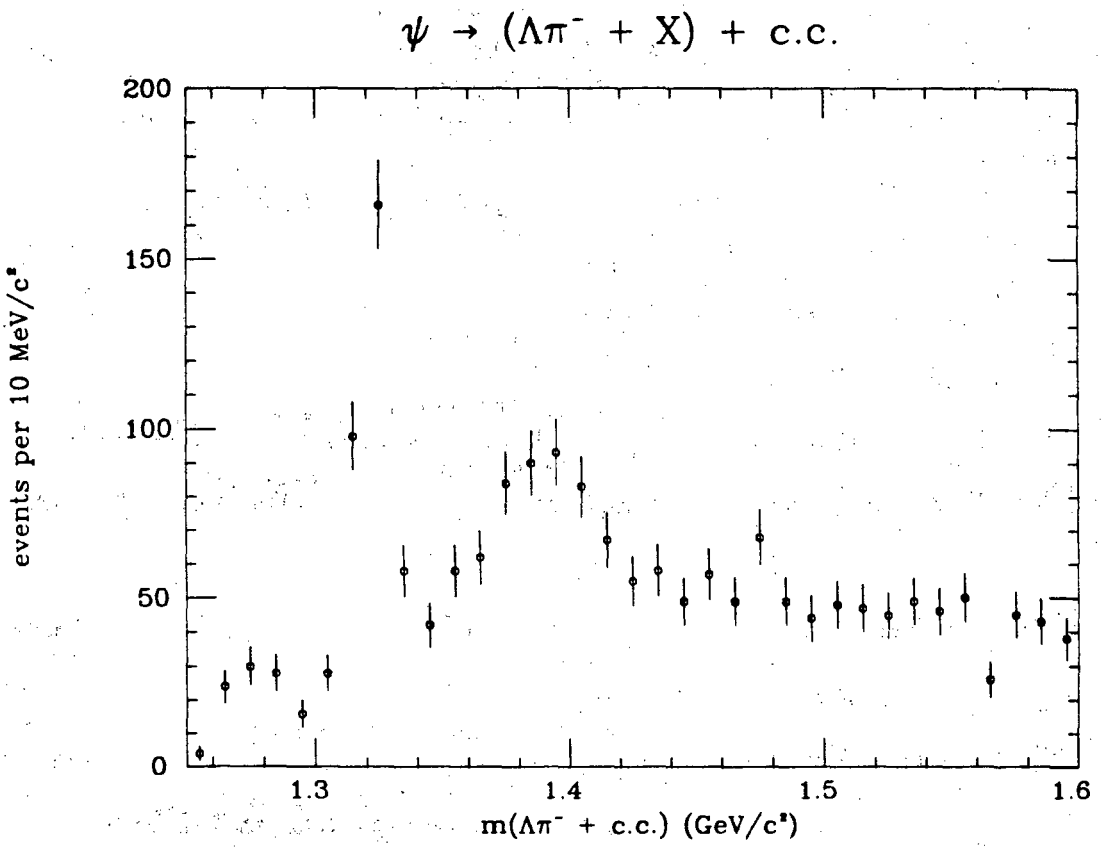

Figure 62: $m(\Lambda\pi^- + c.c.)$.

We then plot the missing mass against the $\Sigma^{*-}(1385)$, shown in figure 63. There is clear evidence of a peak near 1.38 GeV/c^2, which we attribute to the decay

$$\psi \rightarrow \Sigma^{*-}(1385)\bar{\Sigma}^{*+}(1385). \qquad (192)$$

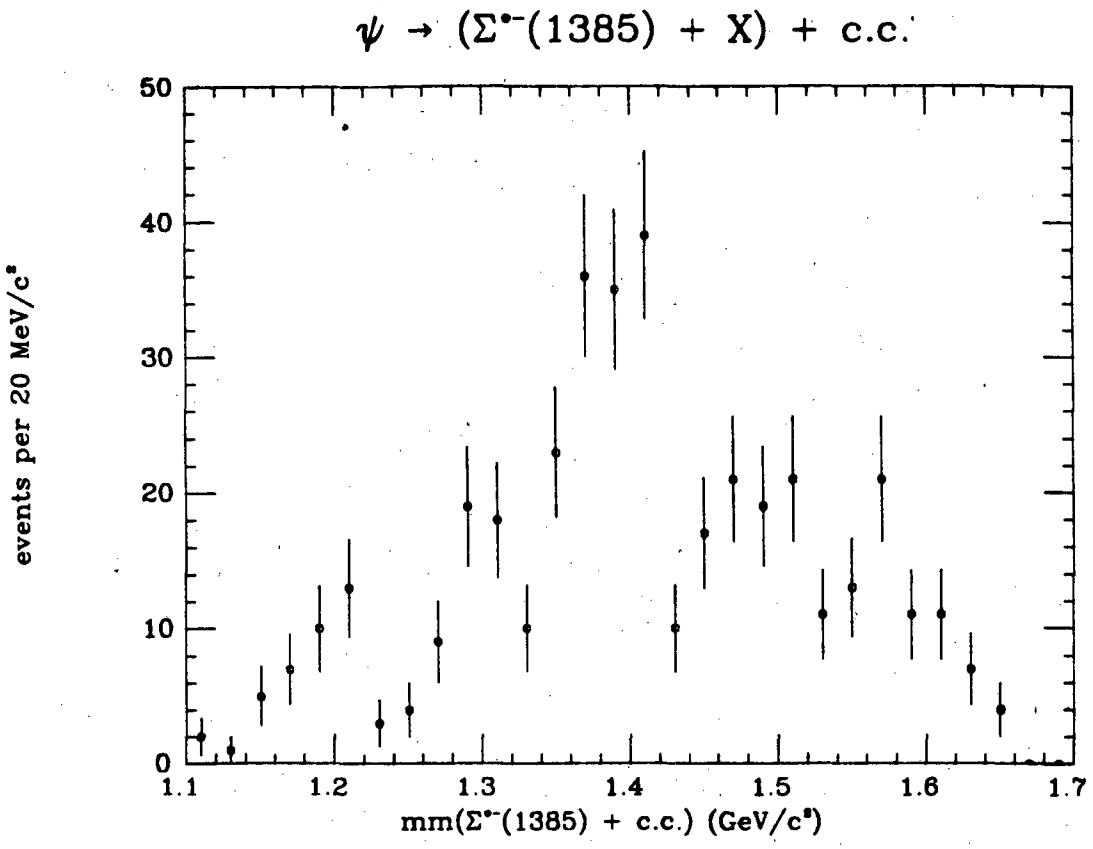

Figure 63: mm(Σ^{*-}(1385) + c.c.).

6.8.2 Branching fraction

Due to the paucity of events from (192) in the data, we use our personal prejudice and subtract the background underneath the peak by hand. From this, we estimate

$$47 \pm 10 \text{ events}, \tag{193}$$

due to (192). Our efficiency was calculated by generating events of the topology (192) according to a phase space distribution, where the Σ^{*-}(1385) is a 40 MeV wide resonance of the Λ and the π^-. From this, we estimate an efficiency of

$$\epsilon = .058, \tag{194}$$

where we have included a factor of .88 for the $\Sigma^* \to \Lambda\pi$ branching fraction. Combining (193) and (194), our result is

$$BR(\psi \to \Sigma^{*-}(1385)\bar{\Sigma}^{*+}(1385)) = (.80 \pm .17 \pm .20)\times 10^{-3}, \quad (195)$$

where we have included an overall 25% systematic error.

6.9 THE DECAY $\Psi \to \Sigma^{*+}(1385)\bar{\Sigma}^{*-}(1385)$

6.9.1 Data reduction

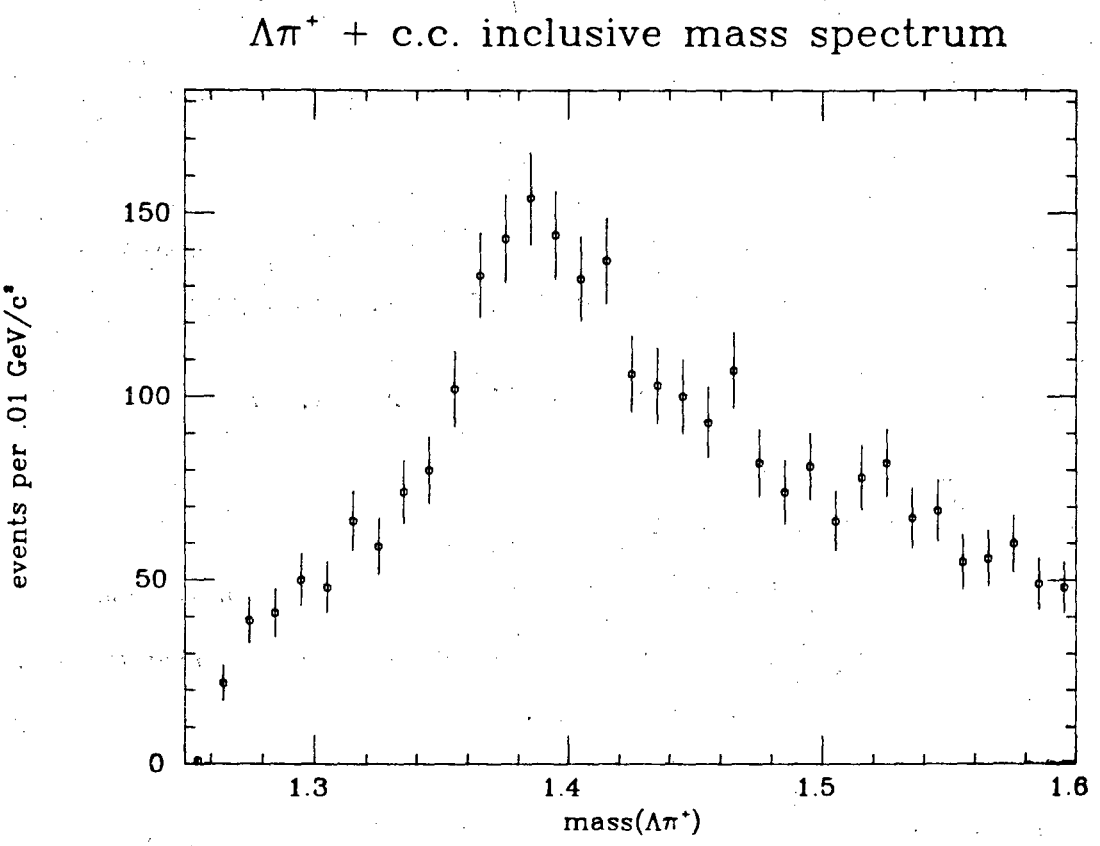

Figure 64: $m(\Lambda\pi^+ + c.c.)$. Note there is no Ξ signal in this charge mode.

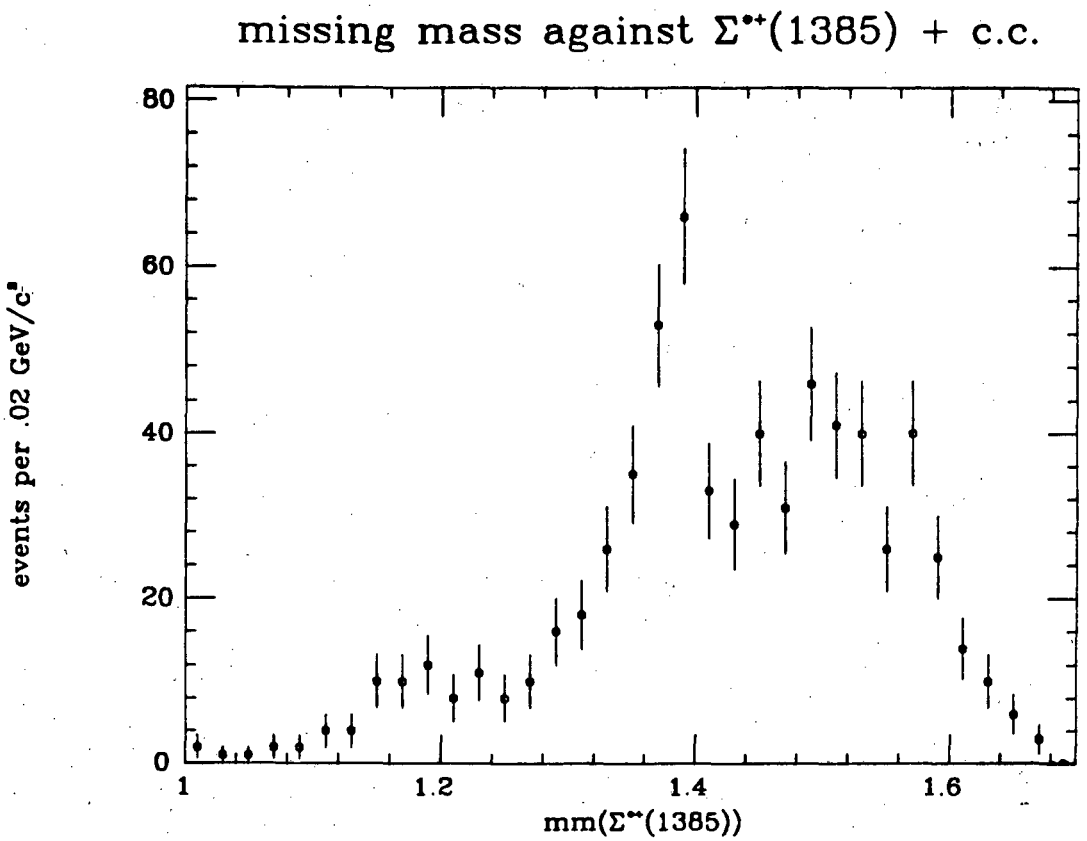

Figure 65: mm(Σ^{*+}(1385) + c.c.).

Λ identification has been previously discussed in section 3.4.2. For this measurement, we require that the pion not originating from the Λ decay come from the primary vertex. This eliminates pions which originate from other secondary vertices (primarily other Λ decays but also K_S decays). For these events, we plot the invariant mass of the $\Lambda\pi^+(\bar{\Lambda}\pi^-)$, shown in figure 64. There is a clear peak centered near 1.38 GeV/c^2, indicating Σ^{*+}(1385) production on top of a substantial combinatoric background.

The missing mass for events with

$$1.36 < m(\Lambda\pi) < 1.41 \text{ GeV}/c^2, \qquad (196)$$

is shown in figure 65. There is a peak centered near 1.38 GeV/c^2, indicating the decay

$$\psi \rightarrow \Sigma^{*+}(1385)\bar{\Sigma}^{*-}(1385). \qquad (197)$$

6.9.2 Branching fraction

Do to the rapidly changing background in the vicinity of the recoil peak and the statistics of the peak, we subtract the background under the peak by hand. From this, we estimate

$$80 \pm 15 \text{ events}, \qquad (198)$$

associated with reaction (197). Our efficiency was calculated by generating events of the topology (197) according to a phase space distribution, the $\Sigma^{*+}(1385)$ being a 35 MeV/c^2 wide resonance of the $\Lambda\pi$ system. From this, we estimate an efficiency of

$$\epsilon = .067, \qquad (199)$$

where we have included a factor of .88 due to the $\Sigma^*(1385) \rightarrow \Lambda\pi$ branching fraction. Our result is

$$BR(\psi \rightarrow \Sigma^{*+}(1385)\bar{\Sigma}^{*-}(1385)) = (1.17 \pm .22 \pm .29)\times 10^{-3}, \qquad (200)$$

where we have included an overall 25% systematic error.

6.10 THE DECAY $\psi \rightarrow \Sigma^0\bar{\Sigma}^0$

6.10.1 Data reduction

The Σ^0 decays essentially 100% of the time into $\Lambda\gamma$. The momentum of either decay product in the Σ^0 rest system is only 74 MeV/c. Consequently, we have very little possibility of reconstructing the Σ^0 from its decay products. We can, however, get a handle on this decay by a slightly more clever technique.

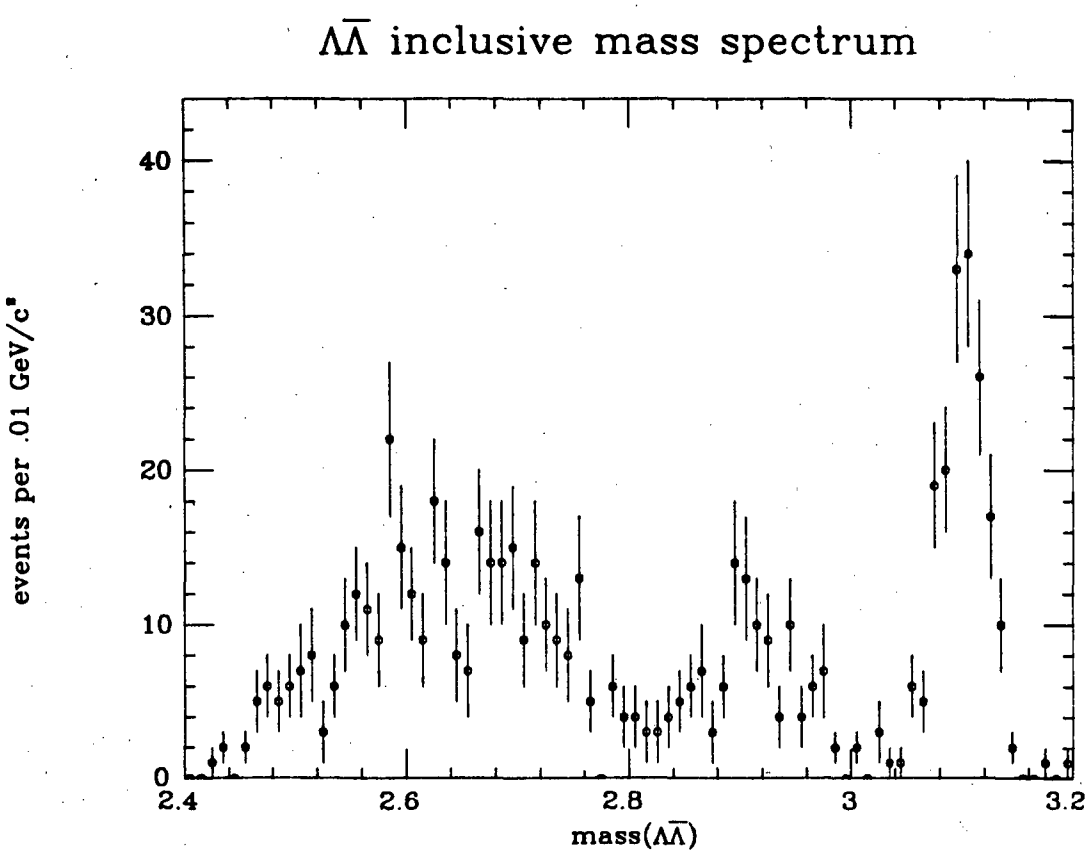

Figure 66: m($\Lambda\bar{\Lambda}$) for all events.

Figure 66 shows the invariant mass distribution for all events with a reconstructed Λ and $\bar{\Lambda}$. For this measurement, we do not make any secondary vertex constraints, as the Λ and $\bar{\Lambda}$ constraints in the same event limit the available phase space to such an extent as to essentially eliminate all background events. Figure 66 shows three distinct features:

1. There is clear evidence for a peak centered near 3.1 GeV/c^2 from the decay $\psi \rightarrow \Lambda\bar{\Lambda}$ (135).

2. There is a broader peak centered near 2.9 GeV/c^2, which will be discussed below.

3. There is a very broad line shape below 2.8 GeV/c^2. In the MKI[62] analysis, this was attributed to the decays $\psi \to \Xi^-\bar{\Xi}^+$ (183), and the isodoublet partner decay

$$\psi \to \Xi^0\bar{\Xi}^0. \tag{201}$$

In fact, other decays which have final states of the topology $\Lambda\bar{\Lambda}\pi\pi$ will populate the region below 2.8 GeV/c^2. As this experiment has shown other decay modes of the ψ such as (192) and (197) which have this final state, we may not use figure 66 to establish a result for reaction (201).

The isoscalar nature of the ψ may be used at this point to good advantage. One can easily show that essentially all events for the decay

$$\psi \to \Sigma^0\bar{\Sigma}^0, \tag{202}$$

have $m_{\Lambda\bar{\Lambda}} > 2.8$ GeV/c^2. Now $m_{\Lambda\bar{\Lambda}}$ for $\Lambda\bar{\Lambda}\pi\pi$ events is < 2.8 GeV/c^2. The only way this helps us is that the decays

$$\psi \to \Lambda\bar{\Lambda}\pi^0, \tag{203}$$

and

$$\psi \to \Lambda\bar{\Sigma}^0 + \text{c.c.}, \tag{204}$$

are I-spin forbidden as the final state must be I=1. Also, we expect the decay (if present at all)

$$\psi \to \Lambda\bar{\Lambda}\gamma, \tag{205}$$

to be suppressed relative to (135) by roughly an order of magnitude. Consequently, we feel safe[67] in attributing all the events with

$$2.84 < m_{\Lambda\bar{\Lambda}} < 2.96 \text{ GeV/c}^2 \qquad (206)$$

to the decay (202).

6.10.2 Angular distribution and branching fraction

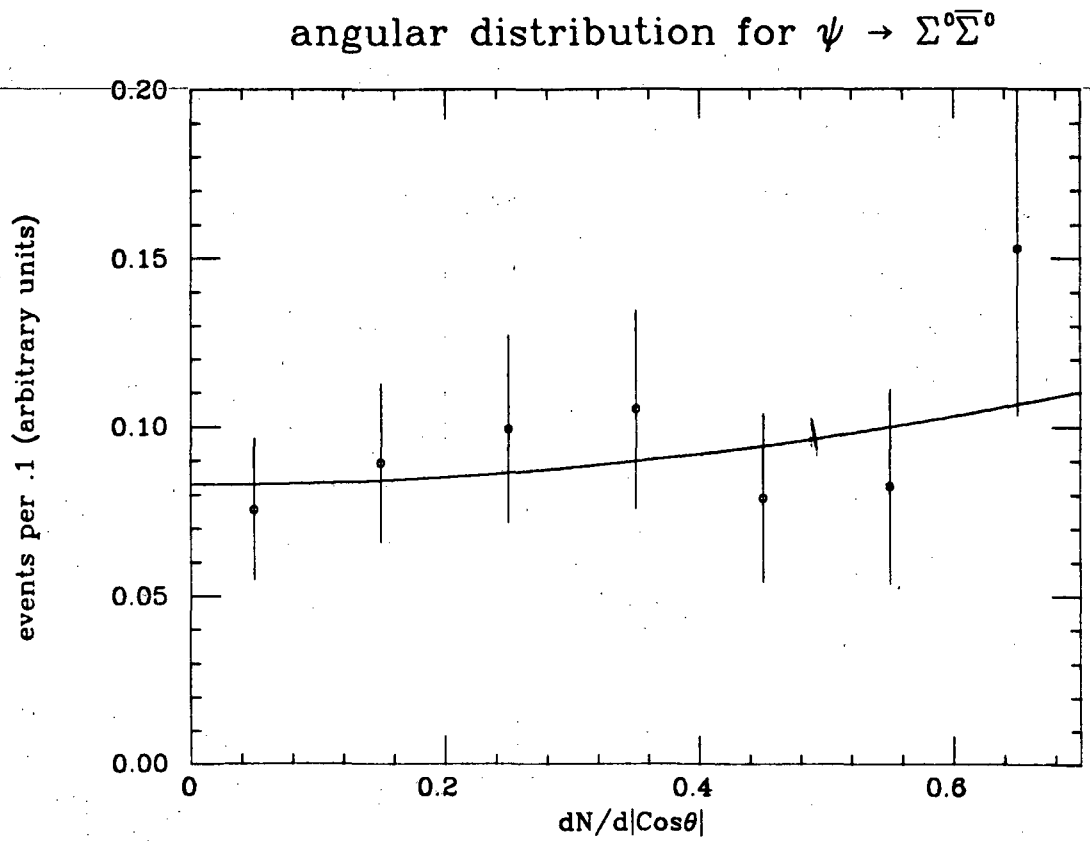

Figure 67: $\Sigma^0\bar{\Sigma}^0$ angular distribution.

Since we never actually reconstruct the Σ^0, we have to be a little careful when measuring the angular distribution. Again, however, the kinematics have been good to us. Since the γ ia a zero mass particle and the decay momentum in the Σ^0 rest system is only

74 MeV/c, the angle between the Λ and the Σ^0 in the lab system is (see Appendix B) always less than 4°. Thus, to a very good approximation, the Λ direction mimics the Σ^0 direction.

Figure 67 shows the $\Sigma^0\bar{\Sigma}^0$ angular distribution, corrected for acceptance by the phase space Monte Carlo. Both the Λ and the Σ^0 are allowed to decay according to their known branching fractions. A fit of the form (187) is done to the angular distribution, from which we get (χ^2 = 2.23/5 DF)

$$\alpha = .68 + 1.2 - .97. \tag{207}$$

In view of the large error, there is not much information in (207).

The branching fraction is now a simple calculation; we must only correct for the measured angular distribution in our Monte Carlo efficiency, whence

$$\epsilon = .043. \tag{208}$$

From figure 66, we attribute

$$90 \pm 9 \text{ events}, \tag{209}$$

to reaction (202). Combining (209) and (208), our result is

$$BR(\psi \to \Sigma^0\bar{\Sigma}^0) = (1.58 \pm .16 \pm .25)\times 10^{-3}, \tag{210}$$

where we have included a 15% systematic error due to the measured angular distribution in quadrature.

6.11 SUMMARY

6.11.1 Discussion of strange baryon decays

The MKI[62] has measured

$$BR(\psi \to \Lambda\bar{\Lambda}) = (1.1 \pm .2)\times 10^{-3}, \qquad (211)$$

(± 15% systematic errors). The two results (211) and (146) differ by 2σ. From experience with the Monte Carlo, the efficiency calculation is quite tricky. The pion momentum in the Λ rest system is only 100 MeV/c, consequently the resulting pion momentum spectrum from Λ's is very soft. As our reconstruction algorithms (and presumably those of reference 62) have difficulty below 100 MeV/c transverse momentum, and dp/dx corrections become significant at low momenta, the apparent discrepancy is not difficult to envision. In our Monte Carlo HOWL, a detailed simulation of nuclear interactions, dp/dx losses and the actual drift chamber performance are used. In addition, (146) uses the measured angular distribution (138) to correct for the ψ production mechanism, which is the largest component of the systematic error due to our poor acceptance at large $|\cos\theta|$. Reference 62 does not explicitly measure this quantity and presumably assumes a $1+\cos^2\theta$ distribution for the production mechanism. This explanation has the "correct" sign for the difference of the two results. Even so, the two experiments are in good agreement when all errors are considered.

We have presented measurements of the I-spin conjugate reactions $\psi \to \Sigma^{*-}(1385)\bar{\Sigma}^{*+}(1385)$, (192) and $\psi \to \Sigma^{*+}(1385)\bar{\Sigma}^{*-}(1385)$, (197). Since both (192) and (197) have identical I-spin structure, the

rates must be identical. Our results (195) and (200) are in excellent agreement.

We have measured the I-spin conjugate reactions $\psi \to \Sigma^{*-}(1385)\bar{\Sigma}^{+}$ + c.c., (167) and (168); and $\psi \to \Sigma^{*+}(1385)\bar{\Sigma}^{-}$ + c.c., (177) and (178). Since all four have the same I-spin structure, their branching fractions (171) and (181) must be identical. They are in excellent agreement with this prediction.

6.11.2 Summary of strange decays

In table 5, we summarize the results of this chapter for both this experiment and the MKI experiment. When more than one measurement has been made from this experiment, we list the "best" result, where "best" is defined as the measurement with the smallest combined error.

The only real surprise in table 5 is that the rate for $\psi \to \bar{p}K^{+}\Sigma^{*0}(1385)$ + c.c. is larger than for $\psi \to \bar{p}K^{+}\Sigma^{0}$. This could be an artifact of the statistics, or some subtle problem in the background shape, but both modes have roughly the same number of events and the $pK\Sigma$ channel has a much higher efficiency as phase space is rapidly running out.

Perhaps the most interesting results of this thesis is the large variety of two body hyperon decay modes of the ψ. We denote $B_8(\bar{B}_8)$ to be any member of the $1/2^{+}$ baryon(antibaryon) octet, and $B_{10}(\bar{B}_{10})$ to be any member of the $3/2^{+}$ baryon(antibaryon) decuplet. Table 6

TABLE 5

Strange decays of $\psi(3.095)$ (units of 10^{-3})

Decay mode	This experiment	MKI[62] (± 15% sys. errors)
$BR(\psi \to \Lambda\bar{\Lambda})$	1.58 ± .08 ± .19	1.1 ± .2
$BR(\psi \to \Sigma^0\bar{\Sigma}^0)$	1.58 ± .16 ± .25	1.3 ± .4
$BR(\psi \to \Xi^-\bar{\Xi}^+)$	1.14 ± .08 ± .20	1.4 ± .5
$BR(\psi \to \Sigma^{*-}(1385)\bar{\Sigma}^+ + c.c.)$	.36 ± .18 ± .09	
$BR(\psi \to \Sigma^{*+}(1385)\bar{\Sigma}^- + c.c.)$	.30 ± .11 ± .08	
$BR(\psi \to \Sigma^{*-}(1385)\bar{\Sigma}^{*+}(1385))$	.80 ± .17 ± .20	
$BR(\psi \to \Sigma^{*+}(1385)\bar{\Sigma}^{*-}(1385))$	1.17 ± .22 ± .29	
$BR(\psi \to \bar{p}K^+\Lambda + c.c.)$	.89 ± .07 ± .14	
$BR(\psi \to \bar{p}K^+\Sigma^0 + c.c.)$	.29 ± .06 ± .08	
$BR(\psi \to \bar{p}K^+\Sigma^{*0}(1385) + c.c.)$	.66 ± .26 ± .11	
$BR(\psi \to \Lambda\pi^-\bar{\Sigma}^+ + c.c.)$ (incl. $\Sigma^{*-}(1385)\bar{\Sigma}^+ + c.c.$)	1.53 ± .17 ± .38	
$BR(\psi \to \Lambda\pi^+\bar{\Sigma}^- + c.c.)$ (incl. $\Sigma^{*+}(1385)\bar{\Sigma}^- + c.c.$)	1.38 ± .21 ± .35	

shows the reduced branching fraction $|M|^2$ for all decays of the type

$$\psi \to B_8\bar{B}_8 \tag{212}$$

where we have divided out the phase space factor of

$$R_2 = \frac{\pi p}{\sqrt{s}}, \tag{213}$$

corresponding to two body phase space. We have also combined statistical and systematic errors. This allows a direct comparison of the matrix elements M for $B_8\bar{B}_8$.

TABLE 6

Reduced branching fractions for $\psi \to B_8\bar{B}_8$ (units of 10^{-3})

Decay mode	Value
$\lvert M(\psi \to \bar{p}p)\rvert^2$	1.73 ± .13
$\lvert M(\psi \to \Lambda\bar{\Lambda})\rvert^2$	1.45 ± .18
$\lvert M(\psi \to \Sigma^0\bar{\Sigma}^0)\rvert^2$	1.58 ± .30
$\lvert M(\psi \to \Xi^-\bar{\Xi}^+)\rvert^2$	1.39 ± .26

The reason this is interesting is that the ψ is presumed to be an SU(3) singlet. In that case, all the matrix elements for $B_8\bar{B}_8$ should be the same. All four of the measurements in table 6 are totally consistent with the ψ being a pure SU(3) singlet.

We may make the same comparison for the decays

$$\psi \to B_{10}\bar{B}_{10}, \tag{214}$$

shown in table 7. The three measurements in table 7 are in good agreement with each other.

For completeness, we present results for

$$\psi \to B_8\bar{B}_{10} + \text{c.c.}, \tag{215}$$

shown in table 8. Only two values are given, but the magnitude of the SU(3) violating matrix elements seems large when compared with tables 6 and 7.

The angular distribution of nucleon-antinucleon pairs from heavy quark decays, especially the ψ and the ψ' have recently become of

TABLE 7

Reduced branching fractions for $\psi \to B_{10}\bar{B}_{10}$ (units of 10^{-3})

Decay mode	Value
$\lvert M(\psi \to \Delta^{++}\bar{\Delta}^{--})\rvert^2$	1.07 ± .29
$\lvert M(\psi \to \Sigma^{*-}(1385)\bar{\Sigma}^{*+}(1385))\rvert^2$	1.13 ± .37
$\lvert M(\psi \to \Sigma^{*+}(1385)\bar{\Sigma}^{*-}(1385))\rvert^2$	1.68 ± .48

TABLE 8

Reduced branching fractions for $\psi \to B_8\bar{B}_{10}$ + c.c. (units of 10^{-3})

Decay mode	Value
$\lvert M(\psi \to \Sigma^{*-}(1385)\bar{\Sigma}+ + \text{c.c.})\rvert^2$	.46 ± .28
$\lvert M(\psi \to \Sigma^{*+}(1385)\bar{\Sigma}- + \text{c.c.})\rvert^2$	.37 ± .13

theoretical interest.[68,69] In particular, the authors of reference 68 predict from a hadronic helicity conservation argument of QCD that

$$\frac{d\sigma}{d(\text{Cos}\theta)} \propto 1 + \text{Cos}^2\theta, \qquad (216)$$

while reference 69 predicts from a calculation involving isospin violating effects that

$$\frac{d\sigma}{d(\cos\theta)} \propto 1 + \frac{m^2_\psi - 4m^2_B}{m^2_\psi + 4m^2_B}\cos^2\theta, \qquad (217)$$

for baryon-antibaryon pairs, where m_B is the mass of the baryon. Table 9 summarizes the results of this experiment for the angular distribution of baryon-antibaryon pairs, along with the predictions of references of Brodsky[68] et al. and Claudson[69] et al.. Reference 69 appears to be favored over reference 68, but the data does not allow us to make a clean separation.

TABLE 9

Angular distributions for $\psi \to B_8\bar{B}_8$

α for $1 + \alpha\cos^2\theta$ angular distribution

Decay mode	This experiment	Reference 68	Reference 69
$\psi \to \bar{p}p$	.61 + .23 - .22	1	.46
$\psi \to \Lambda\bar{\Lambda}$	.72 + .38 - .34	1	.32
$\psi \to \Sigma^0\bar{\Sigma}^0$	.68 + 1.2 - .97	1	.31
$\psi \to \Xi^-\bar{\Xi}^+$	-.13 + .59 - .51	1	.16

Appendix A

NONLEPTONIC HYPERON DECAYS

For purposes of the Monte Carlo, we[70] summarize the theoretical formalism for nonleptonic hyperon decays. The motivation for this outline is that weak effects (e.g. Λ polarization) may be observable at the ψ.

The transition matrix M for any hyperon decay may be written as

$$M = s+p(\vec{\sigma}\cdot\vec{q}), \tag{218}$$

where s and p are the parity-conserving and the parity-changing amplitudes respectively, $\vec{\sigma}$ is the Pauli spin operator, and $\vec{q}$ is the unit vector along the direction of the decay baryon in the hyperon rest frame.

Asymmetry parameters may be defined by the following relationships

$$\alpha = \frac{2Re(s^*p)}{|s|^2+|p|^2}, \tag{219}$$

$$\beta = \frac{2Im(s^*p)}{|s|^2+|p|^2}, \tag{220}$$

and

$$\gamma = \frac{|s|^2-|p|^2}{|s|^2+|p|^2}. \tag{221}$$

With the transition matrix (218), the angular distribution of the decay baryon in the hyperon rest system is

$$I = \alpha(\vec{P}_Y \cdot \vec{q}), \tag{222}$$

where $\vec{P}_Y = \langle Y|\vec{\sigma}|Y\rangle$ is the polarization of the decaying hyperon. The polarization of the decay baryon is

$$\vec{P}_B = \frac{(\alpha+\vec{P}_Y\cdot\vec{q})\vec{q}+\beta(\vec{P}_Y\times\vec{q})+\gamma\vec{q}\times(\vec{P}_Y\times\vec{q})}{1+\alpha\vec{P}_Y\cdot\vec{q}}, \tag{223}$$

where $\vec{P}_B$ is defined in the baryon rest system obtained by the Lorentz transform along $\vec{q}$ from the hyperon rest system in which $\vec{P}_Y$ and $\vec{q}$ are defined.

Conventionally, nonleptonic hyperon decays are described in terms of two independent parameters α, the decay asymmetry, and the angle ϕ, defined by

$$\beta = \sqrt{1-\alpha^2}\sin\phi, \tag{224}$$

and

$$\gamma = \sqrt{1-\alpha^2}\cos\phi. \tag{225}$$

The two parameters α and ϕ are conventionally quoted to determine the decay distributions of the hyperon.

Appendix B

TWO BODY DECAY OPENING ANGLES

This is a completely general formalism for any two body decay $a \rightarrow bc$. the problem is to find the maximum angle between b and the flight direction of a in the lab system, assuming a has a definite momentum in the lab.

Consider first the a rest system. Define an angle θ such that

$$Cos\theta = \frac{\vec{p}_a \cdot \vec{p}_b}{|\vec{p}_a||\vec{p}_b|}, \tag{226}$$

where $\vec{p}_a$ is the momentum vector of a in the lab system and $\vec{p}_b$ is the momentum vector of b in the a rest system. Clearly, $\vec{p}_b = -\vec{p}_a$ in the a rest system. The 4 momentum of b in the a rest system (dropping the b subscript) is just

$$p_\perp = pSin\theta, \tag{227}$$

$$p_{\parallel} = pCos\theta, \tag{228}$$

and

$$E = \sqrt{p^2 + m^2}. \tag{229}$$

We now Lorentz transform into the lab system (denoted as the coordinate system). The lab four momentum of b is

$$p_\perp' = p_\perp \tag{230}$$

$$p_{\parallel} = \gamma(p_{\parallel} + \beta E) \tag{231}$$

and

$$E' = \gamma(E + \beta p_{\parallel}), \tag{232}$$

where γ and β are for a in the lab system. The angle between a and b in the lab system is just

$$\mathrm{Cos}\theta' = \frac{p_{\parallel}'}{p'}$$

$$= \frac{\gamma(p\mathrm{Cos}\theta + \beta E)}{\sqrt{p^2 + (\gamma^2-1)p^2\mathrm{Cos}^2\theta + 2\gamma^2\beta pE\mathrm{Cos}\theta + \gamma^2\beta^2E^2}}. \qquad (233)$$

One can in principle use (233) to analytically find the maximum opening angle, but it is easier to solve (233) numerically for the allowed values of $\mathrm{Cos}\theta$. It is clear for p much less than E that $\mathrm{Cos}\theta'$ is always near 1. Intuitively, this is just that the heavier particle of b and c tends to follow the a direction in the lab system, regardless of how a decayed in its rest system.

REFERENCES

1. J.-E. Augustin, et al., Phys. Rev. Lett. 33 1406 (1974).

2. J. J. Aubert, et al., Phys. Rev. Lett. 33 1404 (1974).

3. A. M. Boyarski, et al., Phys. Rev. Lett. 34 1357 (1975).

4. G. Goldhaber, et al., Phys. Rev. Lett. 37 569 (1976).

5. I. Peruzzi, et al., Phys. Rev. Lett. 37 569 (1976).

6. See, for example, G. Goldhaber and J. Wiss (submitted to Ann. Rev. Nucl. Sci.)

7. This is not a good description of the lighter mesons, as they tend to be very relativistic.

8. E. Eichten, et al., Phys. Rev. D21, 203 (1980).

9. J. Richardson, Phys. Lett. 82B, 272 (1979).

10. W. Haxton and L. Heller, Phys. Rev. D22, 1198 (1980).

11. C. Quigg and J. Rosner, Phys. Lett. 71B, 153 (1977).

12. M. Machacek and Y. Tomozowa, Ann. Phys. (N.Y.) 110, 407 (1978).

13. A. Martin, Phys. Lett. 100B, 511 (1981).

14. C. Quigg and J. Rosner, Phys. Rev. D23, 2625 (1981).

15. E. Eichten and F. Feinberg, Phys. Rev. D23, 2724 (1981).

16. There is a candidate for the η_c' state at a mass of 3.592 GeV/c^2 which needs to be verified. See F. C. Porter, et al., SLAC PUB 2796 (1981) (unpublished).

17. S. Okubo, Phys. Lett. 5, 165 (1963).

18. G. Zweig, CERN Report TH-401, (1964) (unpublished).

19. G. Zweig, CERN Report TH-412, (1964) (unpublished).

20. J. Iizuka, Prog. Theor. Phys. Suppl. 37-38, 21 (1966).

21. J. Iizuka, K. Okada, and O. Shito, Prog. Theor. Phys. 33, 1061 (1966).

22. All gluons are color octets due to the color SU(3) symmetry of the strong interaction, while all mesons are color singlets.

23. T. Appelquist and H. D. Politzer, Phys. Rev. Lett. 34, 43 (1975).

24. T. Appelquist, A. De Rujula, H. D. Politzer, and S. L. Glashow, Phys. Rev. Lett. 34, 365 (1975).

25. M. S. Chanowitz, Phys. Rev. D12, 918 (1975).

26. D. Cohen, et al., Phys. Rev. Lett. 38 269 (1977).

27. R. Dashen and P. Sharp, Phys. Rev. 133, B1585 (1964).

28. J. Yellin, Phys. Rev. 147, 1080 (1966).

29. R. Barbieri, E. d'Emilio, G. Curci, and E. Remiddi, Nucl. Phys. B154, 535 (1979).

30. W. Davies-White, et al., Nucl. Instr. and Meth. 160, 227 (1979).

31. E. Cisneros et al., SLAC PUB 1844 (1976) (unpublished).

32. H. Brafman, et al., SLAC PUB 2033 (1977) unpublished).

33. T. Himel, Decays of the $\psi'(3684)$ to other charmonium states, SLAC PUB 223 (1979) (unpublished).

34. The number 2/3 is not tremendously impressive, but one must remember that real hadronic events comprise a significant fraction of the trigger rate at the ψ, unlike off-resonant data accumulation.

35. G. H. Trilling and A. D. Johnson, LBL Internal Memo IG-301, (1978) (unpublished).

36. Trower, UCRL 2426, Vol. IV (1966).

37. The large r_{xy} cut is made to allow VEEs with large decay lengths, while the large z cut handles VEEs with large dip. In fact, the z cut is relatively tight for VEEs with large dip given our resolution in z.

38. A good writeup of LADRV3 can be found in C. A. Blocker, Decays of the Heavy Lepton $\tau(1785)$, LBL 10801, Ph. D. Thesis (1980) (unpublished).

39. J. B. Dillon, LBL Internal Memo VFINDP, (1981) (unpublished).

40. Note that processes like $\psi \rightarrow K^+K^-$, where one of the K's is

misidentified as a proton, are forbidden in the limit of the ψ being a perfect SU(3) singlet and hence are rare as well as occurring at a much higher nominal momentum, thus not contributing to the background.

41. See, for example, F. James and M. Roos, MINUIT, CERN Computer 7600 Interim Program Library Long Write-up (unpublished).

42. L. B. Okun and M. B. Voloshin, Institute of Theoretical and Experimental Physics, Moscow, Report No. ITEP-95-1976, 1976 (unpublished)

43. S. J. Brodsky, T. A. DeGrand, R. R. Horgan, and D. G. Coyne, Phys. Lett. 73B, 203 (1978).

44. K. Koller and T. Walsh, Nucl. Phys. B140, 449 (1978).

45. W. Bartel et al., Phys. Lett. 64B, 483 (1976).

46. W. Bartel et al., Phys. Lett. 66B 489 (1977).

47. W. Braunschweig et al., Phys. Lett. 67B 243 (1977).

48. G. Alexander et al., Phys. Lett. 72B 493 (1978).

49. R. Brandelik et al., Phys. Lett. 74B 292 (1978).

50. D. L. Scharre, in Proceedings of the XIV Recontre de Moriond, Vol. II, edited by Tran Thanh Van (R.M.I.E.M., Orsay, 1979), p. 219.

51. R.Partridge et al., Phys. Rev. Lett. 44 712 (1980).

52. G. S. Abrams, et al., Phys. Rev. Lett. 44 114 (1980).

53. D. L. Scharre, et al., Phys. Rev. D23 43 (1981).

54. D. L. Scharre, G. Trilling, et al., Phys. Lett. 97B 329 (1980).

55. C. Edwards et al., SLAC PUB 2822 (1981) (unpublished).

56. G. Trilling, LBL Internal Memo TG-319 (1979) (unpublished).

57. P. Jenni et al., (to be published).

58. EGS code, R. L. Ford and W. R. Nelson, SLAC PUB 210 (1978) (unpublished).

59. Note that we certainly can't conclude that this is indeed the N*(1470) as there are two other states in the same mass vicinity, a D'_{13} state N*(1520) and a S'_{11} state N*(1535). The

actual mass peak may in fact be an admixture of these three states. We will proceed on the assumption the mass peak is all the N*(1470). The results as far as the width into N*N is in fact relatively insensitive to this assumption as all three of these states have similar branching fractions into nπ.

60. Actually, a missing π^0 will not produce exactly a Gaussian in the U projection, but will skew the Gaussian toward higher U values due to its finite mass. Due to the size of the π^0 mass and the statistics of the data, this small effect does not alter the analysis.

61. The decay $\rho^0 \to \pi^0\pi^0$ is I-spin forbidden.

62. I. Peruzzi, M. Piccolo, et al., Phys. Rev. D17, 2901 (1978).

63. This tacitly assumes the decay of the ψ into a virtual photon, then to hadrons, which accounts for the G-parity even decays of the ψ, does not contribute significantly to Δ production in this channel. If in fact it does, this would give an I = 1 component to the ψ decay and tend to enhance the Δ^{++} production over the Δ^0 substantially. There is clearly not a big effect, but this experiment is not sensitive enough to establish the presence of an I = 1 component in the decay $\psi \to \bar{p}p\pi^+\pi^-$.

64. Only the states $|1,1\rangle$ and $|1,-1\rangle$ are allowed as the ψ is produced by an intermediate virtual photon.

65. See, for example, M. Perl, High Energy Hadron Physics, Wiley, p.215 f.f..

66. The probability of finding the other Λ once one is found is not much larger than either (142) or (143) due to the large inefficiency for finding the soft pion relative to the solid angle inefficiency.

67. One might possibly worry about the decays $\psi \to \Lambda\pi^0\Sigma^0$ + c.c. feeding through into the $\Sigma^0\bar{\Sigma}^0$ signal region, as we have established results for the I-spin conjugate modes (162), (163), (172), and (173). In fact, the kinematically allowed region for this decay only barely overlaps the $\Sigma^0\bar{\Sigma}^0$ signal region and we estimate its contamination for this measurement to be small.

68. S. J. Brodsky and G. P. Lepage, SLAC PUB 2746, submitted to Phys. Rev. D, (1981).

69. M. Claudson, S. L. Glashow and M. B. Wise; submitted to Phys. Rev. D, (1981).

70. This is largely adapted from R. L. Kelley, et al., Rev. Mod.

Phys. 52 No. 2 Part II (1980).

TECHNICAL INFORMATION DEPARTMENT
LAWRENCE BERKELEY LABORATORY
UNIVERSITY OF CALIFORNIA
BERKELEY, CALIFORNIA 94720